Scattering and Absorption
of X-rays by Interstellar Dust

DISSERTATION

der Fakultät für Physik der Ludwig-Maximilians-Universität München
Doktor der Naturwissenschaften
Dr. rer. nat.

vorgelegt von

ELISA COSTANTINI
aus Rimini, Italien

München, den 27. Februar 2004

Summary

X-ray scattering and absorption by Interstellar Dust

Elisa Costantini

The interstellar dust (ID) in the Milky Way has been studied at all wavelengths: dust grains in the Interstellar Medium (ISM) absorb and scatter the optical, ultraviolet and X-ray radiation. While the absorbed radiation is re-emitted at longer wavelengths, from radio to far and near infrared, the scattering process keeps unchanged the wavelength of the scattered photons. Unlike in the visual band, the scattering in X rays is strongly biased into forward direction and forms "haloes" of diffuse emission surrounding the sources, rather than contributing to a real extinction. Therefore, also the scattered photons can be studied through the spectrum of the halo, its angular extension, and intensity.

After the pilot studies carried out with data from the X-ray observatories *Einstein* (e.g. Mathis & Lee, 1994) and ROSAT (Predehl & Schmitt, 1995; Smith & Dwek, 1998), the new generation X-ray satellites, thanks to improved spectral and spatial resolution, are now able to provide a deeper understanding of the physical and chemical nature of the ID.

The aim of this thesis is to use the complementary characteristics of the instruments aboard the NASA mission *Chandra* and the ESA mission XMM-Newton in order to extensively study the scattering and absorption of X-rays by ID.

In particular, the high energy resolution gratings (XMM-RGS and *Chandra*-HETG), were ideal to study the details of the absorption by the ISM:

- *Chandra*-HETG, the spectrograph with the highest energy resolution in the energy range 0.5-2 keV to date, was able to resolve spectral absorption features which would be the key signatures of absorption by solid grains. These features are called X-ray Absorption Fine Structure (XAFS) and they appear as absorption "teeth" inside an absorption edge. They were clearly detected inside the Mg and Si edges in the spectra of the brightest sources, lying behind a dust layer with equivalent hydrogen column density $N_H \sim$2-5$\times10^{22}$cm^{-2}. Magnesium and silicon are amongst the major constituents of the ID, mostly linked with iron and oxygen to form olivines and pyroxenes. However, only a qualitative comparison with laboratory measurement could help in the tentative identification of the compounds responsible for the absorption. Mathematical handling of such data would require a high statistics which is still yet to be achieved in astrophysics. From this comparative analysis, absorption by a single element could be ruled out, and the presence of a "heavy" and complex compound is

suggested, in agreement with predictions on the chemistry of ID.

- For sources which are not highly obscured by dust, low energy features could be studied in detail with the high throughput of the XMM-RGS. For the bright X-ray binary Cyg X-2 , the XMM-RGS was able to reveal the complexity of the oxygen edge ($E_{edge} = 0.543$ keV). Neutral and mildly ionized oxygen was indeed detected. This absorption is likely not intrinsic to the source, but a manifestation of the local ISM. The ionized phase accounts for few percent of the total oxygen abundance, as also stated by other studies (Juett et al., 2003).

At the same time, the large field-of-view of the CCD detectors (XMM-EPIC-pn and *Chandra* ACIS-S and ACIS-I), together with a moderate energy resolution were suitable for the study of the extended scattered emission around the X-ray sources. The *Chandra* detectors are characterized also by a superb spatial resolution, which allowed me to study the halo emission down to a few arcseconds from the source.

The spectral analysis of the *pure* scattered radiation, i.e. after each external contribution (instrument, source spectrum) is eliminated, was best studied in the case of Cyg X-2 , observed with EPIC-pn. The moderate ISM absorption towards this source allowed for a precise study of the halo spectrum down to 0.4 keV. This analysis led to the unprecedented detection of the *scattering features* from oxygen, magnesium and silicon. The best-fit halo spectrum showed a major contribution from $Fe_{2-x}Mg_xSiO_4$ (olivines) and $Fe_{1-x}Mg_xSiO_3$ (pyroxenes).

The spatial analysis of the extended emission, carried out on a sample of bright-halo sources, led also to interesting results:

- Thanks to *Chandra*-ACIS high spatial resolution, I could determine that the dust along the line-of-sight was not uniformly distributed in the direction of two sources (Cen X-3 and The Great Annihilator). This is not unexpected, since our line-of-sight passes at least through portions of the spiral arms of our Galaxy, but this structure was not previously clearly observed, apart for one ROSAT object (V1974 Cygni, Draine & Tan, 2003). From this analysis it was found that aside from a diffuse component, which accounts for 50-70% of the scattering, there is a second component situated closer to these sources, which accounts for the rest of the scattering.

- The correlation between the scattering, parameterized by the scattering optical depth, and the absorption, parameterized by the hydrogen equivalent column density, already established by the ROSAT analysis (Predehl & Schmitt, 1995) is confirmed here. However, for the sources in the present analysis, the scatter around the best-fit relation is larger than was seen for ROSAT sources, mostly because more sources with a large intrinsic absorption were selected.

I also tested the hypothesis of whether the ID grains are porous, as claimed previously (Mathis & Lee, 1991; Predehl & Schmitt, 1995) using the more precise Mie theory and updated values of gas and dust abundance in the ISM. As a result, the "fluffy" grains are no longer a strongly required parameter in order to explain the data.

- The combined spectral and spatial analysis allowed me to critically examine the validity of the dust grain models and the approximations in the scattering theory that were established, using low resolution instruments. As suggested by Smith & Dwek (1998), I found that the so-called "Rayleigh-Gans approximation" for calculating the differential scattering cross section is completely misleading for energies below 1 keV. Instead, the complete Mie theory (Mie 1908) needs to be used. This is mostly evident in the halo energy distribution, rather than for the halo angular distribution, where the difference between the two approaches results only in a normalization factor.

  As far as dust grain-size distribution models are concerned, I tested the classical model of Mathis Rumpl & Nordsiek (1977) and the Weingartner & Draine model (2001), including these in both the spectral and spatial analysis of the diffuse halo. Due to the quality and statistics of the available data, it was not possible deem one model more suitable than the other.

The present thesis is organized as follows: in Chapter 1 I will present a brief historical review of X-ray studies on the interstellar dust. The physical and chemical nature of the interstellar dust, and the theoretical background used in the analysis, are described in detail in Chapter 2. Chapter 3 is devoted to the description and performances of the X-ray observatories *Chandra* and XMM-Newton.

In Chapter 4, I describe the calibration of the instrumental point spread function that I performed on EPIC-pn and ACIS cameras and how the analysis and modeling of the data was performed. Chapter 5 and 6 contain the *Chandra* and XMM results, respectively, while the conclusions of this study are given in Chapter 7.

Contents

Abbreviations

ISM	Interstellar Medium
ID	Interstellar Dust
PSF	Point Spread Function
SBP	Surface Brightness Profile
R-G	Rayleigh-Gans
MRN model	Mathis, Rumpl & Nordsiek (1977) model
WD01 model	Weingartner & Draine (2001) model.

List of Figures

VI

List of Tables

X

Chapter 1

Introduction

The field of the Interstellar Dust (ID), studied in X-rays, is relatively new and unexplored. Most of the information about the chemistry and the physics of dust grains comes from high resolution telescopes operating from the radio band to the Ultraviolet (UV). Dust indeed absorbs UV light from background stars and remits it in the infrared (IR) regime.

The observed light from a source is obscured by the ISM through the combination of two processes: absorption and scattering. Absorption is due to both gas and dust, whereas scattering of photons is attributed to dust alone. The absorption component as a function of the wavelength may be evaluated by studying the absorbed spectrum of reddened stars along different lines-of-sight. On the other hand, the scattering component is studied through the observation of the albedo (ratio of the incident to reflected light) of reflection nebulae and diffuse galactic light (e.g. Lillie & Witt, 1976).

From IR to UV, the intensity of the scattered light can be described in terms of Rayleigh scattering (Figure 1.1), which can be applied if the ratio between the circumference of the grain, $2\pi a$, and the wavelength of the incident radiation, λ, is much smaller than unity. In this regime the scattered light is distributed almost uniformly into 4π angle, therefore it is difficult to measure unless a favorable geometry of the system emitter-nebula occurs.

Differently from the IR to UV wavelengths range, in the X-ray regime, the observation of absorption and scattering by ID are strongly coupled. If an X-ray emitter is located behind a layer of dust, its radiation would be absorbed and at the same time scattered into the direction of the observer. The scattering mechanism is no longer explained by the simple Rayleigh formula in the X rays (Chapter 2). In particular the scattering angle is in this case very small ($\theta_{scatt} \propto (\lambda/a) \ll 1°$), forward directed, dependent on the energy of the incident photon, and the size of the grain. The effect of the small scattering angle is to produce a halo of diffuse emission around the source (Figure 1.2a).
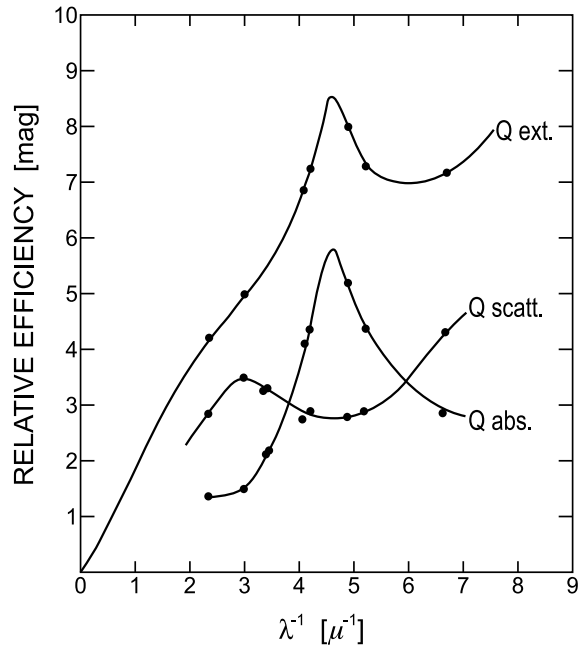
Figure 1.1: The wavelength dependence, from IR to UV, of the scattering and absorption efficiency of interstellar grains as derived from the observed albedo and the extinction curves shown in relation to the extinction curve (Lillie & Witt, 1976). Further information on the extinction curve are discussed in Chapter 2.

In the X-ray regime, the two extinction mechanisms can be simultaneously observed and studied. The energy range in which absorption and scattering can be studied, is a strong function of the equivalent hydrogen column density of the medium (N_H). Indeed the X-ray radiation is obscured by absorption depending on the value of N_H: $I = I_0 e^{-N_H \sigma}$, where I_0 is the source radiation and σ is the absorption cross section. For instance, the soft X-rays (up to ~ 0.2 keV) are completely absorbed by modest column densities ($N_H \sim 10^{21} \text{cm}^{-2}$) and photons of energies 1-2 keV are obscured by $N_H > 2 - 3 \times 10^{22} \text{cm}^{-2}$.

Information on the chemistry, column density and abundances of the the ID grains can be inferred through the analysis of the absorbed spectrum. Simultaneously, the spatial and spectral study of the scattered radiation allow us to learn about the grain size distribution, the number density of the dust and the dust distribution along the line-of-sight. The nature of the grains responsible for the scattering can also be investigated.
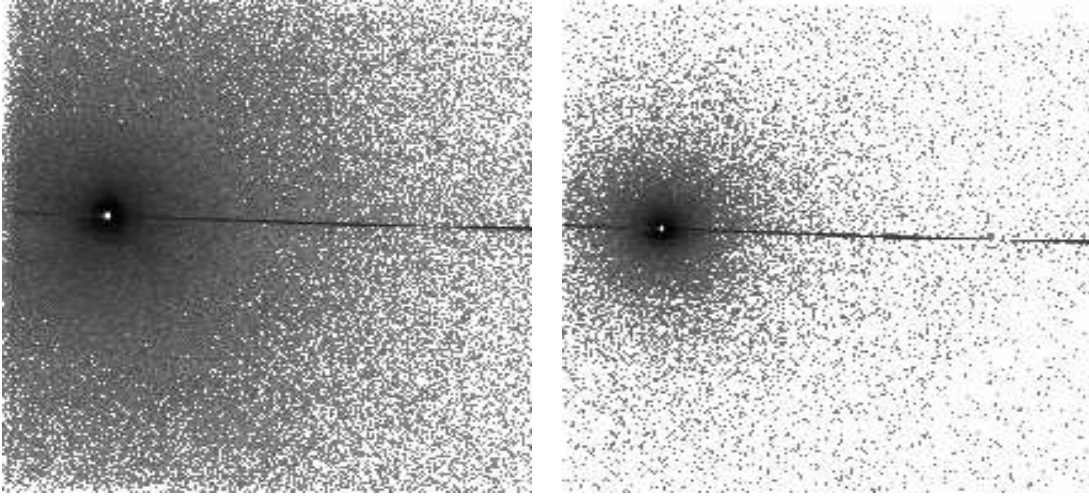
Figure 1.2: The effect of the dust scattering on the X-ray radiation from a background source. The efficiency of the mechanism goes roughly with E^{-2}. in the left panel (a) the energy range is 0.5-2 keV. In the right panel (b), in the interval 6-8 keV, only the scattering of the telescope mirror is visible. The sharp line across the detector is due to instrumental effects.

1.1 Absorption and scattering in X-rays: previous results

- The ISM constituents have many K and L shell electrons with energy levels in the range 0.1-2 keV, and they absorb X-rays. Measuring the optical depth of the absorption edge the abundance of that element can be studied. Spectroscopical studies on the ISM absorption edges have been hampered by technical limitations of the X-rays instruments, indeed an energy band extending well below 2 keV coupled with a high spectral resolution is needed. The detection of the ISM O K edge at 0.54 keV in the high resolution spectrum of the Crab Nebula, observed with the Focal Plain Crystal Spectrometer on board the *Einstein Observatory*, is one of the few examples where the ISM abundances could be studied in X rays (Schattenburg & Canizares, 1986; Schattenburg et al., 1980).

- X-rays scattering halos around celestial objects were first theorized by Overbeck (1965), but the first detection and analysis of X-rays scattered by interstellar grains came almost twenty years later (Rolf, 1983) taking advantage of the imaging capabilities of the *Einstein* X-ray Observatory (Giacconi, 1979): through the observation of the diffuse emission around bright compact objects and supernova remnants lying in the Galactic plane, the modeling and the technical approach of scattering halos were established (*e.g.*, Mauche & Gorenstein, 1986; Mathis & Lee, 1991). Starting from the basic relation:

$$I_{halo} = I_{tot}(1 - e^{-N_g \sigma_{scatt}}),$$

where N_g is the dust column density of the ISM, it was found that the scattering cross section integrated over the total solid angle could be described by the relation:

$$\sigma_{scatt} \propto E^{-2},$$

where E is the energy of the incoming X-rays. The dust size distribution model (*e.g.*, the Mathis Rumpl & Nordsieck model, see Chapter 2). based on IR and optical observational facts, could also be tested on the X-ray results. The number of grains with radius a simply obeys a power law distribution with an index ~ 3.5:

$$n(a) \propto a^{-\alpha},$$

if the grain size is between 0.005 and 0.25 μm.

Scattering halos: the ROSAT heritage

The first systematic analysis of scattering halos was carried out by the German Satellite ROSAT (Trümper, 1982), after the pioneering detections of the *Einstein* satellite. Indeed the Proportional Counter PSPC on board ROSAT provided an unprecedented spatial resolution ($\sim 15''$), coupled with a moderate energy resolution ($\Delta E/E \sim 0.42 \ E_{\text{KeV}}^{-1/2}$) in the energy band 0.1-2.4 keV. The ROSAT mirrors, made of Zerodur, were polished to reach a micro roughness of only ~ 2Å. As a result, the intensity of the radiation scattered from the mirrors (the so-called wings of the point spread function), was sensibly lower than for *Einstein* mirrors. While the extended emission for *Einstein* sources relied on a critical subtraction of such instrumental halo, and only the brightest halos could be detected, with ROSAT, the relatively faint halo emission could be more easily studied for a large number of sources.

The results of the ROSAT campaign on the halo-sources, besides strengthening the earlier *Einstein* findings, pointed out further links between the X-ray and the optical ISM properties. This was quantified by the correlation between the intensity of the halo, parameterized by the scattering optical depth, and the associated absorption, quantified by the equivalent hydrogen column density N_H, along a specific line-of-sight. That relation allows also to distinguish between absorption taking place in the diffuse medium (which correlates linearly with the scattering) and absorption intrinsic

4
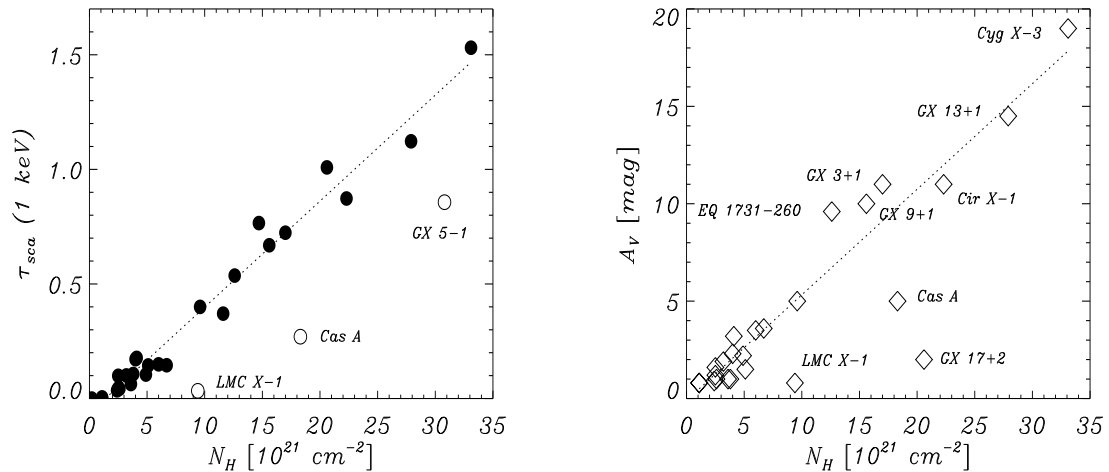
Figure 1.3: Correlations between the equivalent hydrogen column density and the strength of the halo (the scattering optical depth τ, left) and the optical extinction A_V (right), obtained using a sample of 29 ROSAT-PSPC sources (Predehl & Schmitt, 1995)

to the source. As a consequence, also a correlation between scattering strength and the optical extinction could be stated, (Figure 1.3, Predehl & Klose, 1996; Predehl & Schmitt, 1995, hereinafter PS95).

However, the successful performance of ROSAT was not sufficient to shed a light on certain issues, which remained controversial:

- The so called "carbon crisis" in the ISM (Cardelli et al., 1996): the amount of carbon available in dust grains is less than the amount required to produce the observed extinction. Whether this missing carbon exists may also to be a matter of uncertainties in the abundances values (Draine, 2003b).

- The hint of a more complex behavior in the scattering cross section-energy relation. suggests that elements locked up in the grains (i.e. carbon, oxygen, iron, magnesium, silicon) could play a role at softer energies in determining the observed scattered radiation (Smith & Dwek, 1998). The proportionality with E^{-2} seems to be inadequate at energies < 1keV.

- Whether the dust grains are completely filled with matter or are "fluffy" (Mathis & Lee, 1991; Predehl & Schmitt, 1995; Mathis, 1996)

5

1.2   A deeper understanding on the interstellar dust

The XMM-Newton and *Chandra* X-ray Observatories were launched in 1999 and provided higher sensitivity, spectral and spatial resolution than previous observatories. With respect to the ID study, several results have already been achieved.

In particular, thanks to the high resolution grating spectroscopy, XMM-RGS and *Chandra* -HETG, the analysis of absorption features in galactic sources has made a substantial step forward with the clear measurement of edges and resonant absorption lines of elements important in the ISM, providing an additional tool for abundances measurements (e.g. Paerels et al., 2001; Schulz et al., 2002; Takei et al., 2002; Juett et al., 2003). Moreover, substructures in the ISM absorption edges of Mg and Si have been detected for the first time. Such modulations of the edge would be the clear signature of absorption by solid dust grains (Lee et al. 2002).

The large effective area of XMM-Newton mirrors, together with a sufficient energy resolution are ideal to study faint halos which correspond to low ISM absorption. If the absorption is low, the softer photons are only slightly extincted and that part of the spectrum is therefore accessible to the analysis of some of the most abundant elements in the dust which appear between 0.5 and 2 keV.

The excellent spatial resolution of *Chandra* instruments ($\sim 0.5''$) allows to study the scattering halo down to a few arcsec radius from the source, inspecting substructures in the halo shape which would be the signature of a "clumped" medium.

Besides, this characteristic of the *Chandra* telescope made possible to measure distances with high accuracy through the measurement of flux variation of the source, delayed in the halo (see §2.6). Such a delay can be clearly quantified only at few arcsecs from the source, before being smeared out in the halo. The method, proposed by Trümper & Schönfelder (1973) was tested with a *Chandra* ACIS observation of Cyg X-3 giving a distance estimate of: $8.4^{+0.6}_{-0.4}$ kpc (Predehl et al., 2001).

Chapter 2

Physics and Chemistry of Dust in the ISM

2.1 Introduction

In the following, the theoretical background for dust absorption, scattering and emission, is described. Those are the physical processes that allow astronomers to indirectly examine the nature of the interstellar dust grains. In the reminder of this chapter a picture of the physical and chemical nature of the dust grains is discussed.

The electromagnetic radiation produced by an astronomical object is attenuated by the interaction with solid particles in the Interstellar Medium. The extinction is the sum of different kinds of interactions (Daillant & Jibaud 1999):

- **Absorption**: all the energy of the photon is transferred to the atom. A lower energy photon can be re-emitted via fluorescence.

- **Elastic Scattering**: if there is no frequency change between the incoming and the outcoming photon.

- **Inelastic Scattering**: if part of the photon energy is transferred to the atom leading to the ejection of an electron (**Compton Scattering**). If instead the electron passes to an upper atomic level then the interaction is called **Raman Effect**. Since the inelastic scattering does not take place in the environments considered in this thesis, we will not describe it further.

2.2 X-ray absorption

In the modern picture of the atomic structure, the electrons in a multi-electrons atom, occupy a series of atomic orbitals whose wave functions and eigenvalues are solutions of the Schrödinger equation, according to the Aufbau principle: electrons occupy the lowest available atomic orbital first. Each of these orbitals are characterized by four
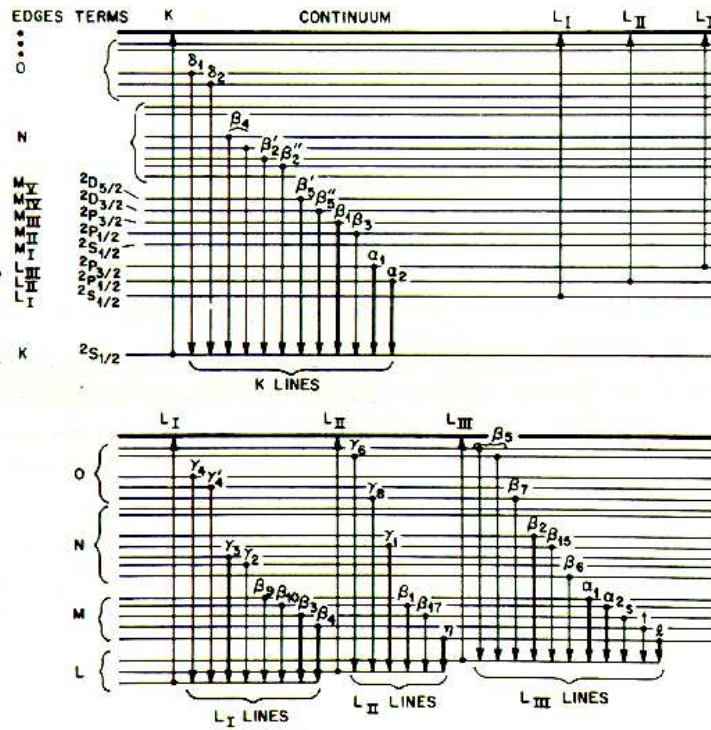
Figure 2.1: The main permitted atomic transitions in emission and absorption (Teo 1986).

quantum numbers: n, l, m, s.

Name	quantum number	Other Name	degeneracy
Principal	$n = 1, \ldots \infty$	orbitals K,L,M,N, etc.	n^2
Orbital (azimuthal)	$l = n - 1, \ldots \infty$	sub shell s,p,d,etc.	$2(2l + 1)$
Magnetic	$m = -l, \ldots, l$		
Spin	$s = \pm 1/2$		

Pauli's exclusion principle forbids any two electrons of having the same set of quantum numbers. Transitions of electrons from one energy level to another leads to the absorption or emission of radiation with energy $h\nu = E_f - E_i$, where E_f and E_i are the energies of the final (n',l',m',s') and initial (n,l,m,s) state, respectively. The selection rules state that only transitions with $\Delta l = \pm 1, 0$, $\Delta m = \pm 1, 0$, and Δn unrestricted, can take place (here we ignore s).

In Figure 2.1, some of the permitted transition, in absorption and emission, are shown. For example, the series of lines which result from higher electrons dropping into a K hole is called the K series and the various lines of the series are called K_α, K_β etc.

(Siegbahn's notation). If, on the other hand, an electron in an occupied level is excited to a virtual bound state by absorbing a photon, an *absorption line* is obtained. If the electron passes to an unbound state, an *absorption edge* would occur. The minimum energy required for this bound-free transition is called the *threshold energy* whose value is the absolute value of the binding energy of the electron. In order of decreasing energy, absorption edges are labeled (Sommerfeld notation) by K, L_I, L_{II}, L_{III}, corresponding to the excitation of an electron from the $1s(^2S_{1/2})$, $2s(^2S_{1/2})$, $2p(^2P_{1/2})$, $2p(^2P_{3/2})$ orbitals (states) respectively.

We can also describe the bound-free transition also in terms of *absorption coefficient*, μ. If a beam of radiation passes trough a layer of material of thickness x, the element loss in intensity is given by:

$$dI = \mu I dx,$$

which integrated gives

$$I/I_0 = e^{-\mu x},$$

where I_0 is the original intensity. As the X-ray energy increases, μ decreases until the binding energy of an element is reached. A sudden increase of μ then occurs. This corresponds to the ejection of the electron from the atom. The absorption coefficient then continues to decrease until the next edge as $e^{(-\tau(E/E_0)^{-3})}$, where τ is the optical depth and E_0 is the threshold energy. There are one, three, five, absorption edges for the K, L, M shells, respectively. It can be seen that within each edge, the absorption cross section decrease with increasing orbital levels. The difference in energy between the successive absorption edges K, L, M, decreases dramatically with increasing quantum number n. The *edge jump* generally decreases in going from low to high energies edges. Finally, with increasing atomic number, the absorption edges shift to higher energies and the edge jump decreases.

2.3   X-ray Absorption Fine Structure

The X-ray absorption fine structure (XAFS) refers to the oscillatory variation of the X-ray absorption as a function of photon energy beyond the absorption edge and identifies the absorption process as caused by solid particles (e.g. Teo, 1986; Königsberger, 1988). We have seen that the absorption, normally expressed in terms of the absorption coefficient (μ), can be determined from the measurement of the attenuation of X-rays upon their passage through a material. If the X-ray photon energy (E), is tuned to be the binding energy of some core level of an atom in the material, an abrupt increase in the absorption coefficient, known as absorption edge, occurs. For isolated atoms, the

absorption coefficient decreases monotonically as a function of energy beyond the edge. For atoms either in molecules or embedded in a condensed phase, the variation of the absorption coefficient at energies above the absorption edge displays a fine structure.

In detail, the XAFS is a final state interference effect involving scattering of the outgoing photoelectron from the neighboring atom. The probability that an X-ray photon will be absorbed by an innermost level, "core", electron depends on both the initial and final states of the electron. The initial state is the localized core level corresponding to the absorption edge. The final state is that of the ejected photoelectron which can be represented as an outgoing spherical wave originating from the X-ray absorbing atom. Nevertheless, if the absorbing atom has a neighboring atom, the outgoing photoelectron wave will be backscattered by the neighboring atom, producing in this way an incoming electron wave. The final state is then the sum of the outgoing and all of the incoming waves, one from each neighboring atom. It is exactly the interference between the outgoing and the incoming waves that give rise to the observed sinusoidal variation of μ as a function of E (the XAFS). For a monatomic gas, where there are no neighboring atoms, a photoelectron ejected by absorption of an X-ray photon will travel as a spherical wave with a wave number k:

$$k = \sqrt{\frac{2m}{\hbar^2}(E - E_0)}, \tag{2.1}$$

where E_0 is the edge energy.

The curves in Figure 2.2 are examples of XAFS behavior. In the presence of neighboring atoms, for example in MgO, the outgoing photoelectron can be backscattered from the neighboring atoms producing an incoming wave which can interfere either constructively or destructively with the outgoing wave near the origin, resulting in the oscillatory behavior of the absorbing rate. The amplitude and frequency of this sinusoidal modulation of μ vs E depends on the type and bonding of the neighboring atoms and their distance from the absorber, respectively.

We can describe two types of modulations, the EXAFS (Extended X-ray Absorption Fine Structure) and the XANES (X-ray Absorption Near Edge Structure). The former displays structures which may extend up to 1000 eV above the absorption edge and may have an amplitude of up to a few tenth of the edge jump (1-20 %). Conversely, the XANES are features inside the edge shape itself. We have one or the other behavior depending on the value of the wave number, k (Equation 2.1). It may be proven that if $k > 4$ Å^{-1} then single scattering of the photoelectrons from immediate neighboring atoms is the dominant process and EXAFS are produced. If $k < 4$ Å^{-1}, the multiple scattering is important and XANES are produced.
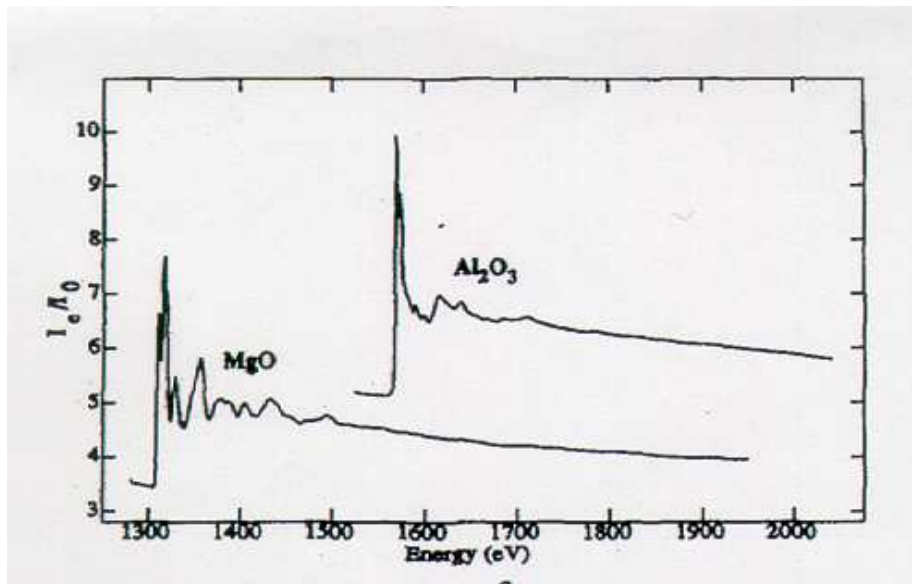
Figure 2.2: Laboratory measurement of the spectral behavior of MgO and Al_2O_3 around the Mg and Al edge respectively. In the vertical axis the absorption coefficient is plotted (Wong et al., 1995).

2.4   Scattering

The quantity which typically describes scattering of any kind is the scattering cross section $\sigma_{sca} = 4\pi|b|^2$. The complex number b, called the **scattering length** is a function of the scattering angle, as we will see later, and relates the amplitude of the incident and scattered radiation:

$$A_{sca} = -A_{in}b\frac{e^{-ikr}}{r}, \tag{2.2}$$

where r is the distance at which the scattered radiation is measured. It is assumed much larger than the wavelength of the incoming radiation (far-field approximation). Any particle scatters and absorbs part or all of the energy; therefore the total cross section for extinction is defined as:

$$\sigma_{tot} = \sigma_{sca} + \sigma_{abs}. \tag{2.3}$$

The *optical theorem* links the total scattering cross section to the scattering length measured at scattering angle zero.

$$\sigma_{tot} = 2 \ \lambda\Im m(b(0)). \tag{2.4}$$

From this relation alone we cannot infer the total value of b (de Bergevin, 1999).

11

2.4.1 Thomson and Rayleigh Scattering

As long as the frequency of the incident photon is large compared to the specific atomic frequency, the Thomson Scattering occurs. In this case, each electron in the atom scatters independently, and the outcoming radiation is a function of the atomic number and the electronic distance from the nucleus. The scattered amplitudes add coherently.

The equation of motion for the electron under the influence of the magnetic field takes into account the binding of the electron to the nucleus by adding a restoring force of stiffness κ and a damping coefficient γ which indicates the loss of energy radiated from the electron. From here we could derive the expression for the scattering length (here polarization is neglected):

$$b = r_e \frac{\omega^2}{\omega^2 - \omega_0^2 - i\gamma\omega/m}, \tag{2.5}$$

where $\omega_0^2 = \kappa/m$. It happens that $\omega, \omega_0 >> \gamma/m$, thus from the comparison between ω and ω_0, it holds:

- $\omega > \omega_0 \rightarrow$ Thomson scattering for a free electron:
  $b = r_e$,
  where r_e is the Lorentz classical electron radius $r_e = e^2/mc^2 \sim 2.818 \times 10^{-15} m$.

- $\omega << \omega_0 \rightarrow$ Rayleigh scattering:
  $b = -r_e \frac{\omega^2}{\omega_0^2}$.

After integration over the scattering length in eq 2.5 over all atomic electrons gives:

$$b_{atom} = r_e(f + f' + if''). \tag{2.6}$$

The term in f is the classical Thomson scattering (f is the atomic form factor), while f' and f'' give the correction, called **anomalous scattering** due to resonance. This expression may be completely described by a quantum mechanical approach to the scattering-absorption phenomenon (de Bergevin, 1999).

2.5 X-ray scattering in the ISM

In Figure 2.3, the scattering geometry is illustrated (e.g. Smith & Dwek, 1998; Predehl & Schmitt, 1995). The intensity of the scattered radiation (eq. 2.7) depends on the amount of dust that the light has to go through, the dust distribution along the line of sight ($f(z)$, where $z \equiv R/D$) the size of the scattering grain a, the grain density as a function of a, $n(a)da$ and finally the flux and spectral energy distribution of the source. In units of photons per cm^2 per second per steradian we have:

$$I_{sca}(\theta) = \int_{E_{min}}^{E_{max}} dE \ F_x \ S(E) \int_{a_{min}}^{a_{max}} da \ N_H \ n(a) \int_0^1 \frac{f(z)}{(1-z)^2} \left(\frac{d\sigma(E, a, \phi)}{d\Omega} \right) dz. \quad (2.7)$$
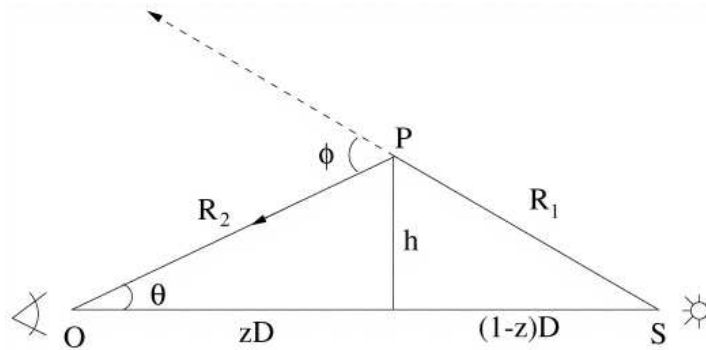
Figure 2.3: *Scattering geometry of an X ray coming from a source S, scattered by a dust grain by an angle ϕ, at distance $(1 - z)D$ from the source (Smith & Dwek, 1998).*

2.5.1   The Mie theory

The Mie theory calculates the exact solution for scattering and absorption of light from spherical particles (Mie 1908, Van der Hulst 1967) starting from Maxwell's equations with appropriate boundary conditions.

Scattering and absorption are expressed in terms of efficiency factors, the ratio between the physical cross section and the geometrical cross section:

$$Q_{ext} = \frac{C_{ext}}{\pi a^2}, \quad (2.8)$$

$$Q_{ext} = Q_{sca} + Q_{abs}. \quad (2.9)$$

Extinction strongly depends on the grain size, a and energy involved (here expressed in wavelength) through the parameter:

$$X = \frac{2\pi a}{\lambda} \quad (2.10)$$

Finally, the refractive index m of the material involved has to be carefully measured (Henke 1993):

$$m = \beta - i\delta \quad (2.11)$$

In the X-ray regime δ is small ($\delta <$0.1) compared to β, which approaches unity for both dielectric materials (silicates , ice) and metals (Fe). It also holds: $\Re e(m) = n \approx c_1 + c_2\lambda^{-2}$, where $c_1 >> c_2$ are constant. The proportionality between extinction and

13
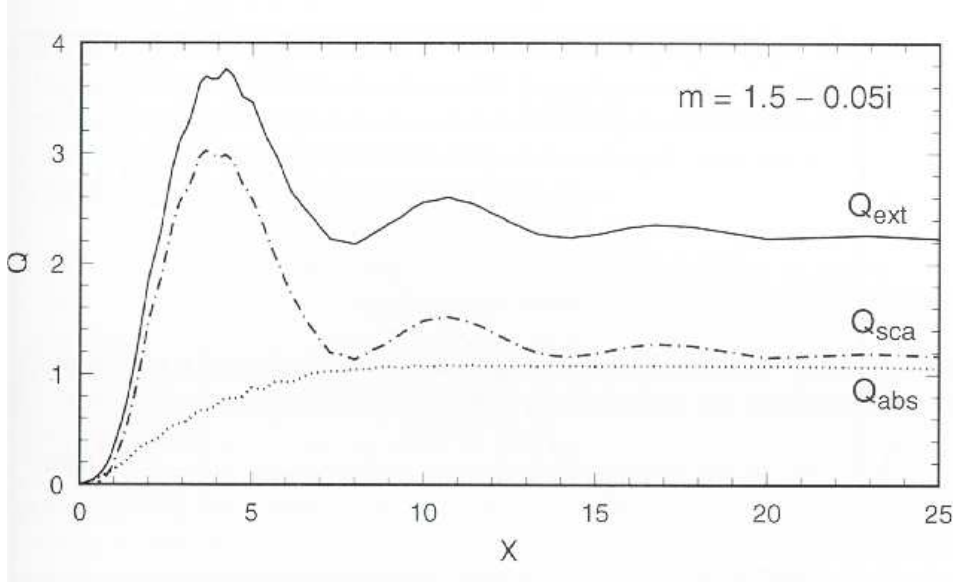
Figure 2.4: *The Efficiency for extinction, scattering and absorption as a function of X for a constant refraction index m=1.5-0.05i (this condition is true in first approximation, given eq 2.11). The peak is in correspondence of the resonance value of λ and a (Whittet 2003).*

both scattering and absorption efficiency is given by the *albedo* $0 < \alpha < 1$:

$$Q_{sca} = \alpha \ Q_{ext} \tag{2.12}$$

$$Q_{abs} = (1 - \alpha)Q_{ext}. \tag{2.13}$$

In Figure 2.4 the dependence of the efficiency as function of the parameter X is shown. In the limit of very large grains (X>15), the extinction becomes independent from energy. For smaller values of X, extinction is instead sensible to the grain size and/or the energy, for a chosen material. The peak is the result of the resonance between λ and the grain size.

The scattered amplitude is expressed by the modulus squared of the scattered amplitude $i(\theta_{sca})$ in two orthogonal direction of polarized light. We neglect polarization in this context so that (we drop in the following the subscript for θ):

$$S(\theta) = |i(\theta)|^2. \tag{2.14}$$

The complex number $i(\theta)$ is numerically evaluated for each considered θ, a and energy (Wiscombe 1980), requiring some computational effort. The total scattering cross section is then expressed as:

14
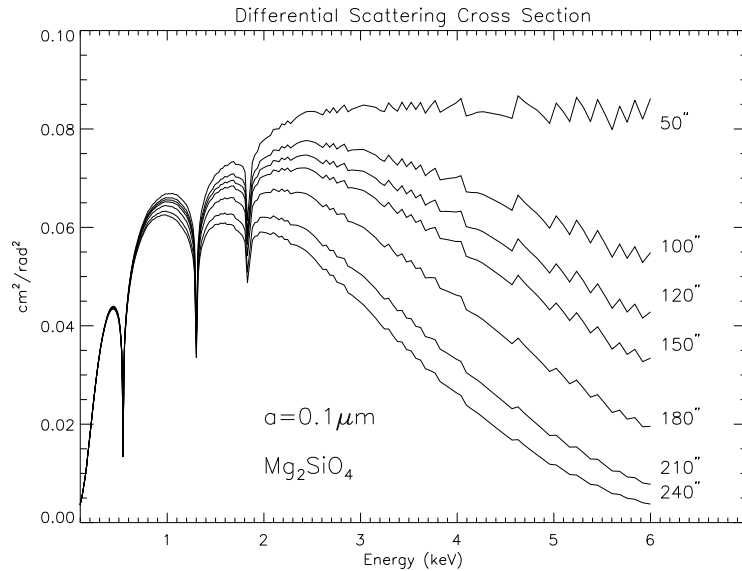
Figure 2.5: *The scattering cross section at specific solid angles vs energy for Mg_2SiO_4. A single grain size (0.1 μm) is considered. The features of the constituents of Mg_2SiO_4 are evident: oxygen, magnesium and silicon at 0.54, 1.3, 1.84 keV, respectively.*

$$C_{sca} = Q_{sca}\pi a^2 = \frac{2\pi}{E^2}\int_0^\pi S(\theta)sin(\theta)d\theta. \qquad (2.15)$$

For each angle θ we can evaluate the energy dependence of the scattering cross section. In Figure 2.5 such dependence is illustrated at angles from $50''$ up to $240''$, for forsterite (Mg_2SiO_4) and for a typical grain size $a=0.1$ μm.

Finally, we can define the asymmetry parameter $(0 < g(\theta) < 1)$:

$$g(\theta) \equiv < cos(\theta) >= \frac{\int_0^\pi S(\theta)sin(\theta)cos(\theta)d\theta}{\int S(\theta)sin(\theta)d\theta} = \frac{2\pi}{C_{sca}}\int_0^\pi S(\theta)sin(\theta)cos(\theta)d\theta. \qquad (2.16)$$

If the scattered rays spread over 4π, $g(\theta) \sim 0$, while for forward directed scattering, $g(\theta) \to 1$. Such parameter is a sensitive function of the grain size: as the ratio a/λ goes from 0.3 to 1, in the UV/optical regime, $g(\theta)$ increases from 0.15 to 0.75 (Witt, 1989)

2.5.2 Rayleigh-Gans Theory

The Rayleigh-Gans approximation for the differential cross section $(d\sigma/d\Omega)$ requires the following two assumptions. First that the reflection from the surface of the dust

particle is negligible, which means $|m - 1| \ll 1$, where m is the complex index of refraction of the dust. This ensures that the X-ray enters the dust particle instead of being reflected. The second, more stringent requirement is:

$$2\pi a/\lambda \, |m - 1| \ll 1. \qquad (2.17)$$

This means that the incident wave is not shifted inside the grain. In this limit, and for sufficiently small scattering angles, it may be shown that the intensity of the scattered waves add coherently inside the grain (Smith & Dwek, 1998). Such intensity is thus proportional to the square of the number of atoms in the grain: $I \propto N^2 \propto \rho^2 a^6$, where, ρ and a are the density and the radius of the grain respectively. This can be expressed also as:

$$\frac{a_{\mu m}}{E_{\text{keV}}} \left(\frac{\rho}{3g\text{cm}^{-3}} \right) \ll 0.316. \qquad (2.18)$$

It is evident that the coherency requirement fails if the value for the energy of the incident wave is not significantly larger than the grain size value.
In the R-G limit, the scattering process can be analytically described (Mauche & Gorenstein, 1986):

$$\left(\frac{d\sigma}{d\Omega} \right) (E, a, \phi) \; = \; 2a^2 \left(\frac{2\pi a}{\lambda} \right)^4 |m - 1|^2 \left(\frac{j_1(y)}{y} \right) (1 + cos^2\phi). \qquad (2.19)$$

The spherical Bessel function j_1 can be well approximated by a Gaussian function:

$$\propto 2a^2 \left(\frac{2\pi a}{\lambda} \right)^4 |m - 1|^2 \frac{1}{9} exp \left(-\frac{y^2}{2\sigma^2} \right) (1 + cos^2\phi), \qquad (2.20)$$

where $y = (4\pi a/\lambda)sin(\phi/2)$ and σ is a function of the energy and size of the dust particle.

Limitation of the R-G approximation are found if E is approximately less then 1keV or for large grains (e.g. $a=1\mu m$), when the proportionality to N^2 is lost (Figure 2.6). The functional form for the differential scattering cross section would then be (Mathis & Lee, 1991):

$$\left(\frac{d\sigma}{d\Omega} \right) (E, a, \phi) \; \approx \; exp(-0.4575 \; E(\text{keV})^2 a(\mu m)^2 \left(\frac{\theta}{1-z} \right)^2). \qquad (2.21)$$
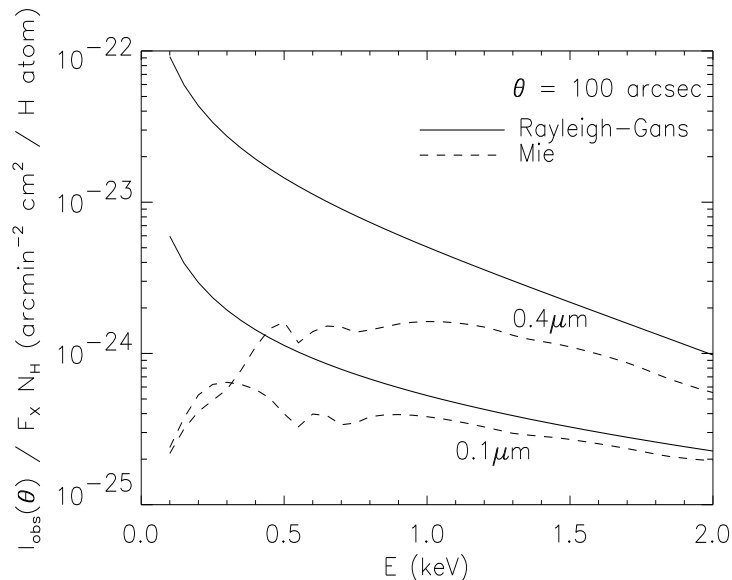
Figure 2.6: Scattered intensity at 100″ for silicate grains of radius 0.1 and 0.25μm, calculated both by the RG approximation and the Mie solution as a function of X-ray energy. For E=1 keV, the two methods show the same energy dependence; below it, absorption modifies the E dependence, an effect that becomes more pronounced at 0.25 μm (Smith & Dwek, 1998).

2.6   Distance determination

Given the scattering geometry of Figure 2.3, it is evident that the scattered X-rays cover a slightly longer path compared to the unscattered ones before coming to the observer. Thus, if the X-ray emitter undergoes a flux variability, such variation will be delayed and damped in the halo. This simple model was developed by Trümper & Schönfelder (1973). In the case of very small scattering angles, the time delay is (Figure 2.3):

$$t = \frac{d}{c}\left[1 - z\left(1 + \frac{\Theta^2}{2}\right) - \sqrt{(1-z)^2 + z^2\Theta^2}\right], \qquad (2.22)$$

where c is the velocity of light, Θ is the scattering angle, x is the fractional distance and d is the distance of the source. Since the relation between the scattering angle and the observed angle is:

$$\Phi = \frac{\Theta}{1-z}. \qquad (2.23)$$

Assuming that $\Theta \ll 1 - x$, we have:

$$t = \frac{d}{2c}\frac{z\Theta^2}{1-z}, \qquad (2.24)$$

17

and the distance may be estimated.

2.7   Dust in the Galactic environment

The interstellar medium (ISM) constitutes approximately for one fifth of the total mass of our Galaxy (Whittet, 1981). It interacts and exchanges continuously with the stellar component. New stars condense from interstellar clouds and as they evolve, they irradiate the surrounding ISM. At the final stages of the star life, a fraction of material returns back to enrich the ISM with heavy elements, result of the nuclear reaction inside the star or created as a consequence of a supernova explosion.

A fraction of the material in the ISM is locked in solid particles. Such interstellar dust (ID) account for 1% of the total mass of the ISM. The most obvious effect of the ID is the extinction of the star light. The ultra-violet (UV) and visible light absorbed by the grains is re emitted in the infrared (IR) accounting for $\sim 20\%$ of the bolometric luminosity of the Milky Way. The observed magnitude of an object must be then unfolded from the contribution of the extinction A_V by the ID. Using the Johnson (1963) notation:

$$m_V - M_V - A_V = 5 log d - 5 \qquad (2.25)$$

Where M_V and m_V are the absolute and apparent magnitudes respectively in the V band and d is the true distance of the object.

Stars behind a layer of dust appear redder, that is at lower temperature, than what calculated from the spectroscopy. The reddening of a star is expressed by the *color excess*: $E_{B-V} = (B-V) - (B-V)_{obs}$, where $(B-V)$ and $(B-V)_{obs}$ are the intrinsic and observed color indexes. E_{B-V} is positive (extinction is always larger in B band, 4400Å than in V band, 5500Å) or zero if there is no extinction.

The ratio of total to selective extinction $R_V = A_V/E_{B-V}$ depends theoretically on the composition and the size distribution of the grains, but in practice it is empirically evaluated (Johnson 1968) and it is found to be $R_V = 3.1$ for most lines of sight. For denser regions $R_V = 5.5$, requiring a shift of the dust size distribution toward larger sizes (Kim et al., 1994). On the other hand $R_V \sim 1.2$ if the Rayleigh Scattering is important ($A_\lambda \propto \lambda^{-4}$). As far as extinction in other galaxies is concerned, the Magellanic Clouds (LMC and SMC) are the best studied examples. Variations in R_V are found for these objects, with an extinction law which is similar to the Galaxy diffuse medium law (Fitzpatrick, 1986; Misselt et al., 1999). The reddening is also consistent with the Galactic one, scaled for the lower metallicity of the LMC and SMC (*e.g.*, Kurt & Dufour, 1998).

18

2.8   The Chemistry of the ID

Until the 1960s very little was known about the chemical composition of the ISM. Now we know the complexity of the environment and the importance of the interaction gas-dust, even if the exact chemistry of the medium is still not known. Spectroscopic studies of the absorption lines of interstellar gas pointed out that there was a striking difference between the abundances calculated from the line strength of interstellar gas (from optical and UV spectra) and the solar abundances. The heavier elements (atomic number $Z > 12$) were less abundant in the interstellar environment. The discrepancy could be solved allowing the missing atoms to be in solid phase. The degree of depletion is near 100% for most refractory elements (e.g. Si, Ca, Fe, Ni and Ti). It is generally believed that the ID is mainly constituted by silicates and carbonaceous materials.

- The silicates are found mostly in amorphous state (Li & Draine, 2002). At most the 5-10% of the silicates is allowed to be in crystalline state (Bouwman et al., 2001). Silicates may be found either in the form of pyroxene ($Mg_xFe_{1-x}SiO_3$) or olivine ($Mg_{2x}Fe_{2-2x}SiO_4$). In the circumstellar environments Fe appears to be almost absent in olivine in favor of compounds such as $MgSiO_3$ (Molster et al., 2002). Fe should be then combined with oxygen alone (FeO, Fe_2O_3, Fe_3O_4) or in metallic form, at least in these environment. The actual abundance ratio of Si, Fe and Mg varies depending on the assumed ISM abundances values and there is not a general agreement about that. A value of 3:1 (Howk et al., 1999) for the (Fe+Mg) Si ratio would allow Fe to be also disjointed from olivine. Recent results (Sofia & Meyer, 2001) show that such ratio would be instead consistent with the one expected from olivine, 2:1.

- Carbonaceous material is detected in various forms depending on how the C is bonded: diamond ($sp3$), graphite ($sp2$) amorphous (mixture of $sp3$ and $sp2$) or hydrogenate amorphous (if H is present), polycyclic aromatic carbon (PAH) ($sp2$ with H at the edges), aliphatic hydrocarbons (CH).

- Ices are supposed to coat dust grains in the denser molecular clouds ($A_V > 3.3$, Whittet et al., 1998). The ice mantle is variable from one line of sight to another and it is basically formed by a mixture of H_2O, NH_3, CH_3OH, CH_4.

2.8.1   Observational Evidences of interstellar dust

The chemical composition of ID is inferred by the characteristic of the several emission and absorption features that may be imprinted in the extinction curve. The μm region

λ (μm)	Carrier
0.2175	Graphite (PAH?) $\pi \to \pi^*$ transition
9.7	Si-O silicates stretching mode
18	O-Si-O silicates bending mode
3.4	C-H stretching mode
3.1	H_2O (ice)
4.67	CO (ice)
7.7	CH_4
9.0,2.2,2.9,3.4	NH_3 (ice)
15.2,3.5,6.8	CO_2 (ice)
3.3	C-H stretching mode (PAH)
6.2,7.7	C-C stretching mode (PAH)
8.6	C-H in-plane bending mode (PAH)
11.3	C-H out-of-plane bending mode for mono H[1]
12.0	for duo H[1]
12.7	for trio H[1]
13.55	for quartet H[1]

[1] see caption of Figure 2.7

Table 2.1: *Main ID spectroscopic features in the Galactic environment (from Draine, 2003b).*

is described by:

- The most prominent feature in the extinction curve is the 2175 Å bump. Its central wavelength is constant regardless of the line of sight, while the width varies by $\sim 12\%$ at 2σ confidence level (Fitzpatrick & Massa, 1986). The most accredited responsible for such feature is graphite in the form of randomly oriented small spheres. Although this explanation would be consistent with ISM abundances (Draine, 1989), it would not explain the variability in the width. If instead one allows the graphite to be in PAH (grain size $\sim 1nm$), then such variability would be the result of different mixtures of PAH in different environments (Weingartner & Draine (2001), hereafter WD01).

- silicates absorption features are detected at $9.7\mu m$ and $18\mu m$, identified as the Si-O stretching mode and O-Si-O bending mode respectively. The $9.7\mu m$ feature structure seems to indicate that the silicates are amorphous, given that it shows no features, while the crystalline silicates observed in laboratory are more structured. The strength and profile of the $9.7\mu m$ is consistent with absorption by olivine and indicates that nearly 100% of Si, Fe and Mg must be in solid form in the ISM (*e.g*, Draine, 2003a).

- The "trait d'union" between gas and dust particles are considered the PAH particles (polycyclic aromatic carbon). They are planar molecules composed
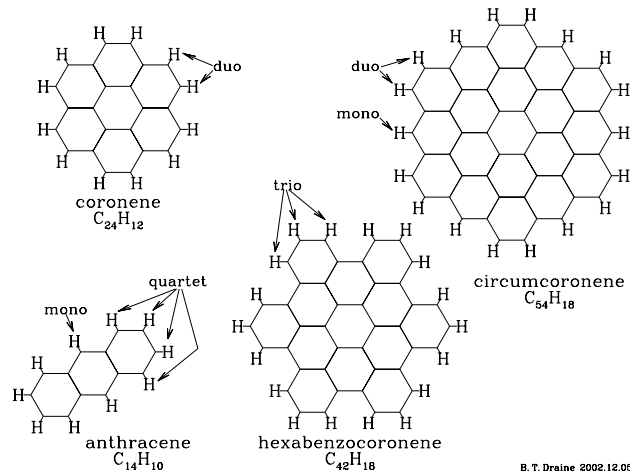
Figure 2.7: Structure of PAH molecules. The Hydrogen is called mono, duo, trio, quartet depending on how many neighboring H atoms there are (Draine, 2003b).

of benzene rings of the diameter of $\sim 1nm$. The PAH were detected through characteristic vibrational modes of the hydrogens atoms attached at the edge of the system as illustrated in detail in Figure 2.7. The emission features fall in the IR band (Omont 1996), at 3.3, 6.2, 7.7, 8.6 and 11.3 μm (Table 2.1) and they should account for $\sim 5\%$ of the carbon in the ISM.

- Other relevant features in the extinction curve are due to C-H stretching in chain-like hydrocarbons (3.4 μm), ice features like the 3.1 μm O-H stretching mode in icy H_2O (Table 2.1). Many weak absorption features, called *Diffuse Interstellar Bands* which still have to be identified are detected in the 0.38-0.868 μm band. A possible carrier would be extra small particles, like PAH.
The nature of the *Extended Red Emission* is also very uncertain. It may be hydrogenate amorphous carbon (Witt & Schild, 1988), or silicon nanoparticles (Smith & Witt, 2002). It appears as a broad emission band in the range 5400-9000 Å and it is supposed to be produced by photoluminescence at lower energies of a UV photon.

2.9   The Mathis, Rumpl & Nordsieck Model (MRN)

Mathis et al. (1977), constructed their classic interstellar dust model on the basis of the observed extinction of starlight for lines of sight passing trough diffuse clouds. The observational evidences were *(i)* the strong absorption observed at 9.7 and 18 μm, corresponding to stretching and bending modes in silicates and *(ii)* the strong extinction feature at 2175 Å , which can be reproduced approximately by small graphite particles (Stecher & Donn, 1965; Wickramasinghe & Guillaume, 1965) The simplest model

incorporating both silicates and graphite material consists of two separate grain populations, one of of silicate composition and one of graphite composition. MNR found that the extinction curve is well represented if the grain-size distribution (with identical form for each component), is given by:

$$dn_{grain} = Cn_H a^{-3.5}, a_{min} < a < a_{max}$$

with $a_{min} = 50$ Å and $a_{max} = 0.25 \mu m$; $n_{grain}(a)$ is the number density of grains with size $\leq a$ and n_H is the number density of H nuclei (in both atoms and molecules). MRN adopted spherical grains, for which the Mie theory can be used to compute extinction cross sections.

2.10   The Weingartner & Draine Model (WD)

Since the development of the MRN model, more observational evidence has become available; some of these require revisions of the model. The WD grain size distribution adds both the size distribution which takes into account very small carbonaceous grains and are consistent with the observed extinction, for different values of R_V.

(a) a different distribution depending on the density of the interstellar environment, parameterized by R_V (§2.7). The distribution for $R_V = 5.3$ has significantly fewer "small" grains ($a < 0.1 \mu m$) than the one for $R_V = 3.1$. This was expected since generally there is relatively less extinction at short wavelengths (provided by small grains) for larger values of R_V.

(b) The class of carbonaceous grains with a size less than 50 Å,the Polycyclic Aromatic Hydrocarbons (PAH), responsible for the thermal emission in the $3 - 60 \mu m$ range and for emission features at 3.3,6.2,7.7 and 11.3 μm. On the other hand, the non detection of the 10 μm silicates feature in emission from diffuse clouds appears to rule out silicate grains as a major component of the $a \leq 15$ Å .
In the WD, uncertainties on the abundance of C still remains and distributing C either in graphite or PAH appears simplistic (the model does not justify the emission feature at 3.4 μm, for example). Moreover the depletion of Fe in the ISM is not observationally well determined. Iron is locked not only in olivine, but it may be in form of metal or oxides like FeO or magnetite Fe_3O_4 (Draine & Lazarian, 1999; Howk et al., 1999). The mathematical expression used in the present thesis for the very small carbon grain distribution is (Li & Draine, 2002):

$$\frac{1}{N_H} \left(\frac{dn_{gr}}{da} \right)_{vsg} \equiv D(a) = \sum_{i=1}^{2} \frac{B_i}{a} \exp\left(-\frac{1}{2} \left[\frac{\ln(a/a_{0,i})}{\sigma} \right]^2 \right) \quad , \qquad a > 3.5 \text{ Å} \quad (2.26)$$

$$B_i = \frac{3}{(2\pi)^{3/2}} \frac{\exp(-4.5\sigma^2)}{\rho a_{0,i}^3 \sigma} \frac{b_{C,i} m_C}{1 + \text{erf}[3\sigma/\sqrt{2} + \ln(a_{0,i}/3.5 \text{ Å})/\sigma\sqrt{2}]} \quad , \qquad (2.27)$$

where m_c is the atomic mass of C, $\rho = 2.24 \mathrm{gcm}^{-3}$ is the density of graphite, $b_{c,1} = 0.75 b_c$, $b_{c,2} = 0.25 b_c$ with b_c total C abundance per H nucleus, $a_{0,1} = 3.5\mathrm{\AA}$, $a_{0,2} = 30\mathrm{\AA}$, and $\sigma = 0.4$. The functional form used is:

$$\frac{1}{N_H}\frac{dn_{\mathrm{gr}}}{da} = D(a) + \frac{C_{\mathrm{g}}}{a}\left(\frac{a}{a_{\mathrm{t,g}}}\right)^{\alpha_{\mathrm{g}}} F(a;\beta_{\mathrm{g}},a_{\mathrm{t,g}}) \times \begin{cases} 1 & , & 3.5\,\mathrm{\AA} < a < a_{\mathrm{t,g}} \\ \exp\left\{-[(a-a_{\mathrm{t,g}})/a_{\mathrm{c,g}}]^3\right\} & , & a > a_{\mathrm{t,g}} \end{cases}$$
$$(2.28)$$

$$\frac{1}{N_H}\frac{dn_{\mathrm{gr}}}{da} = \frac{C_{\mathrm{s}}}{a}\left(\frac{a}{a_{\mathrm{t,s}}}\right)^{\alpha_{\mathrm{s}}} F(a;\beta_{\mathrm{s}},a_{\mathrm{t,s}}) \times \begin{cases} 1 & , & 3.5\,\mathrm{\AA} < a < a_{\mathrm{t,s}} \\ \exp\left\{-[(a-a_{\mathrm{t,s}})/a_{\mathrm{c,s}}]^3\right\} & & a > a_{\mathrm{t,s}} \end{cases}.$$
$$(2.29)$$

The term

$$F(a;\beta,a_{\mathrm{t}}) \equiv \begin{cases} 1 + \beta a/a_{\mathrm{t}} & , & \beta \geq 0 \\ (1-\beta a/a_{\mathrm{t}})^{-1} & , & \beta < 0 \end{cases}$$
$$(2.30)$$

provides the curvature of the distribution for larger dust sizes (Figure 2.8).

Equations 2.28 and 2.29 are for carbonaceous and silicates grains respectively. The expression allows a smooth cutoff for $a > a_t$ (Greenberg 1985) and a change in slope $d\ln n_{gr}/d\ln a$ for $a < a_t$. In Figure 2.8 the grain size distributions according to the WD and the MRN models are displayed. The WD model extends down to the grain size of the PAH. Moreover, it predicts a lower carbon density at all values of a compared to the MRN model.

23
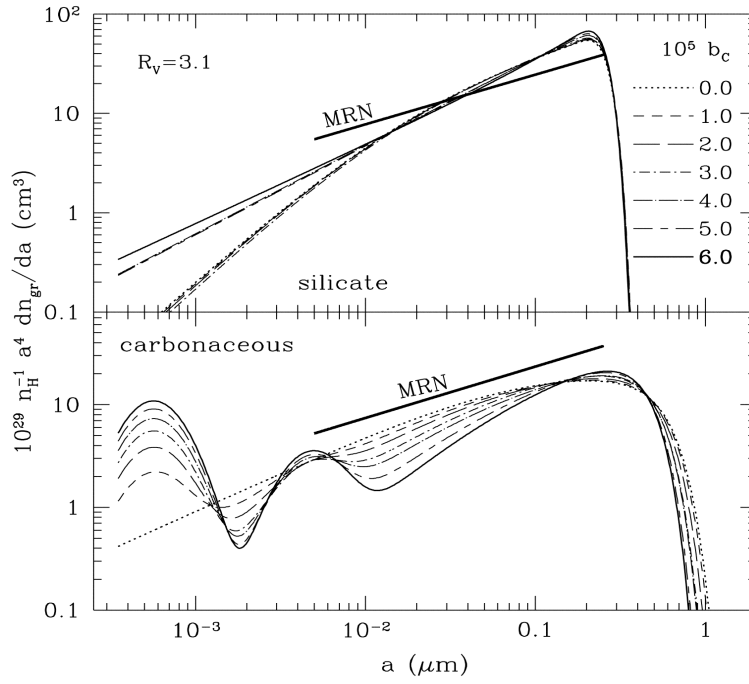
Figure 2.8: Grain size distribution for R=3.1. The value of the abundance of very small carbon grains are also reported. The preferred value is 6×10^{05}. For comparison, also the MRN model is plotted, both for carbon (top) and silicates (bottom) from Weingartner & Draine (2001).

Chapter 3

The Instruments

The study of ID in X rays requires high sensitivity and spectral resolution as well as spatial resolution. The two X-ray observatories *Chandra* and XMM-Newton are very useful in this respect. The large effective area, coupled with the broad band spectroscopy of XMM-Newton are suitable for studying the fainter scattering halos, while the narrower Point Spread Function (PSF) of *Chandra* enables the detection of the halo down to very small radii from the central source. Finally, the high spectral resolution of the *Chandra* gratings allows absorption features by the dust grains to be detected.

A number of technical limitations exists. First of all the problem of pile-up, affecting CCD observation of bright sources, as they are in the present sample; secondly, uncertainties in the exact observational characteristics of scattering by the telescope mirror itself remain uncharacterized.

In this chapter I will give an overview on the instruments used in the present analysis.

3.1 The Chandra X-ray Observatory

Chandra [1] is the X-ray component of NASAs four Great Observatories, together with the Hubble Space Telescope, the Compton Gamma-Ray Observatory and the Infrared mission Spitzer Space Telescope. The satellite couples an efficient high resolution ($\leq$ 0.5 arcsec) X-ray telescope (the High Resolution Mirror Assembly, HRMA) with a set of imaging and spectroscopic instruments, namely:

- The Advanced CCD Imaging Spectrometer (ACIS, see e.g., Garmire et al., 2003) is a two CCD array, divided in ACIS-I (four Front-Illuminated (FI) CCDs) and ACIS-S: four front-illuminated plus two Back-Illuminated (BI) CCDs in one of

---

[1]A detailed explanation on the instruments and data reduction may be found: http://asc.harvard.edu/proposer/POG/html/.
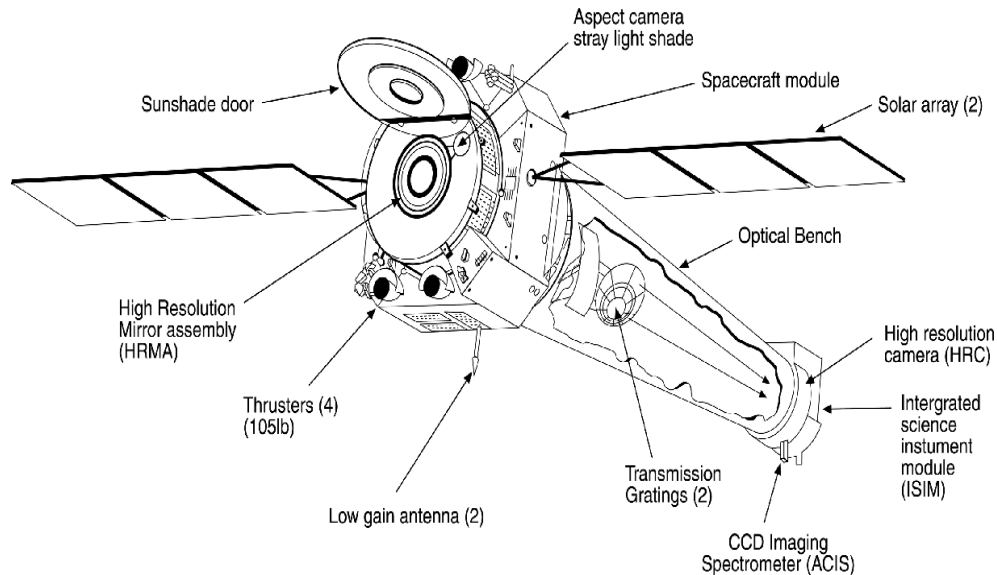
Figure 3.1: The Chandra payload with labeled subunits.

which the best focus position is located. ACIS-I is mainly used for imaging since it has a larger field of view.

- The High Resolution Camera (HRC, Murray et al., 1998) is comprised of two micro-channel plate imaging detectors: the HRC-I designed for wide field imaging and HRC-S, thought as a read out support camera for the LETG. The HRC detectors have the highest spatial resolution on *Chandra*, best approaching the HRMA point spread function.

- The High Energy Transmission Grating (HETG) coupled with the ACIS-S forms the HETG spectrometer (§3.1.2, Marshall et al., 2003).

- The Low Energy Transmission Grating (LETG) coupled with the HRC-S forms the LETG Spectrometer. It provides a resolving power $E/\Delta E > 1000$ at low energies (0.08-0.2 keV, Brinkman et al., 2000).

3.1.1 ACIS, the Advanced CCD Spectrometer

The CCD device

A CCD is a solid-state electronic device composed primarily of silicon. A gate structure defines the pixel boundaries. The FI chips have the gate structure facing the X-ray incident beam. On the contrary, the BI chips have the back side facing the HRMA, exposing the photo sensitive depletion region of the CCD directly to the incoming

26

Table 3.1: ACIS main parameters

CCD format	1024x1024 px
Pixel size	24μm (=0.492 arcsec)
On-Axis Effective Area	600 cm^2 @ 1.5 keV (FI)
Min row read out time	2.8 ms
Frame time	3.2 sec(full frame)
read out time	41 μ s(per row)
Sensitivity	4×10^{15} erg/cm^2/s in 1 ksec

rays and enhancing the sensitivity. Indeed, the silicon in the active, depletion region, situated below the gates where most of the absorption takes place, has an electric field applied, to quickly move the charge to the gate surface. The gates make the confined charge to be passed to another set of pixels in parallel to a serial readout at one edge of the CCD by varying the voltage in the gates. In a typical observation mode of ACIS, the active region is exposed for a certain frame time (3.2 sec) at the end of which the charge is transferred in 40 ms into the frame region. While the next exposure begins, the data in the frame store is moved to the local processor which identifies the position and the amplitude of each event, after removing the bias (the charge in a pixel not exposed to X-ray radiation). This data, together with the events of a small region surrounding the pixel are labeled as "graded" and passed to the telemetry stream.

ACIS performances

The spatial resolution is physically limited by the size of the pixel (0.492 arcsec). Approximately 90% of the encircled energy lies in the first 4 pixels (2 arcsec) at 1.49 keV and 5 pixels at 6.4 keV for both BI and FI chips. The back-illuminated response extends to lower energies (0.5-8 keV) than the front-illuminated CCDs and the resolution depends mostly on the position. On the other hand, the FI response extends to higher energies (0.8-10 keV, Figure 3.2). The energy resolution of the FI chips, which in principle approaches the theoretical limit at all energies, underwent a substantial worsening after the launch, becoming a function of the row number. The degradation was caused by low energy protons encountered during the passages through the radiation belt.

3.1.2   HETG, the High Energy Transmission Grating

In the spectrometer system, the HETG provides spectral separation through diffraction. The X rays from the mirror are diffracted by the gratings in one dimension by an angle β defined by the grating equation : $sin\beta = m\lambda/p$, where p is the period of the grating lines, m is the order of the dispersion, λ is the wavelength (in Å) of the
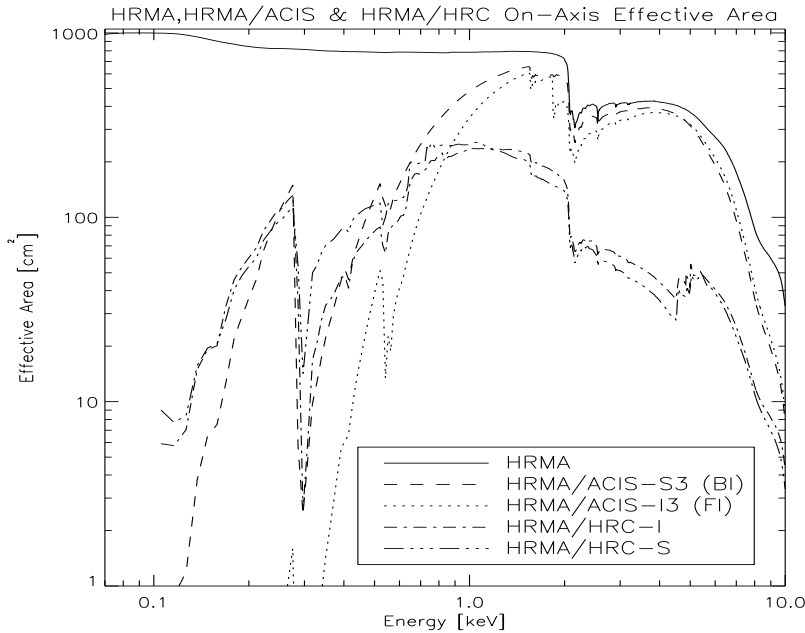
Figure 3.2: Effective Area for Chandra detectors.

incident photon. In order to avoid third-order aberrations, gratings are mounted on a "Rowland Circle", whose schematic view is shown in Figure 3.3. The view from the top of the system is shown in the top panel. The X rays are diffracted through an angle β from one side of the circle to the other. The vertical line is the plane where the diffraction image is visualized. The dotted lines indicate the focus of the 0th undispersed order (m=0, in the grating equation). The bottom panel looks along the dispersion direction. The photons hit the Rowland focus before converging in the imaging focus. This causes an extension of the photons along the cross dispersion direction by an amount less than 100 μm. The "Rowland Torus" is formed by rotating the circle about the optical axis. Individual grating facets are mounted such that their centers lie on the torus. Such structure allows the focal properties of the telescope to be stable in the dispersion direction for a large range of diffraction angle β, therefore minimizing any grating-added optical aberration.

HETG performances

HETG coupled with ACIS-S and the HRMA becomes the HETG Spectrometer which can reach a resolving power $E/\Delta E \sim 1000$ in the 0.4-10 energy band. The HETG comprises of two grating assemblies, the Medium Energy Grating, MEG and the High Energy Grating, HEG. The MEG (0.4-5 keV) intercepts rays from the two outer mirror shells while the HEG (0.8-10 keV) intercepts ray from the two inner ones. The HEG and MEG dispersions are offset by 10 degrees. The effective area depends on the

28
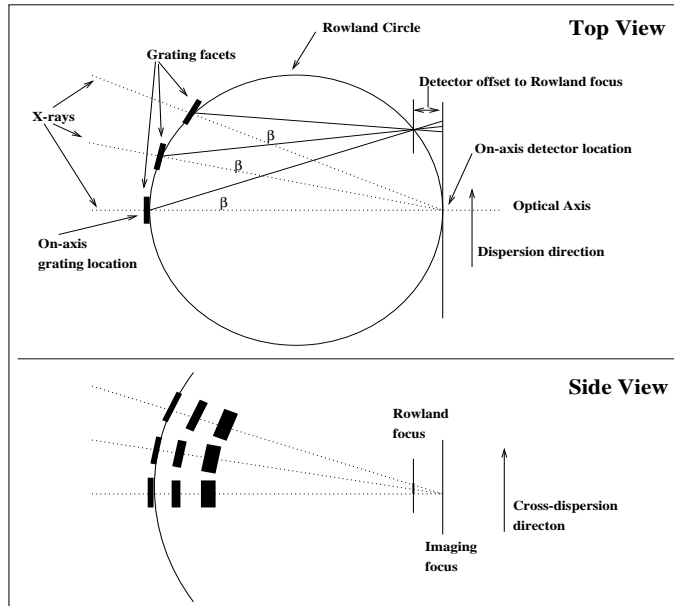
Figure 3.3: The Rowland geometry (see text).

dispersion order considered. At the first order it reaches its maximum at 1.5 keV (200 cm^2).

3.2 The XMM payload

The X-ray astronomy satellite XMM-Newton[2] is a cornerstone mission of the European Space Agency's Horizon 2000 program. It was launched on 10 December 1999 and put in a 48h orbit by the Ariane-V rocket. It includes two large payload modules connected by a long carbon fiber tube which forms the telescope bench. On the focal plane assembly the two Reflection Grating Spectrometers (RGS, den Herder, 2001) readout cameras, an EPIC-pn (Strüder, 2001), and two EPIC-MOS imaging detectors (Turner, 2001) are located. The space-craft Service Module contains most of the spacecraft subsystems, as well as the Optical Monitor Instrument (Mason, 2001) star trackers and three X-ray Mirror Modules. The configuration of the scientific payload is showed in Figure 3.4. Each of the three X-ray telescopes on board consists of 58 Wolter I Gold mirrors which are nested in a coaxial and co-focal configuration (Aschenbach et al., 1987) with diameters ranging from 153 to 350 mm. The axial mirror length is 600 mm, with thickness from 0.47 to 1.07 mm. The focal length measures 7500 mm. The two RGS gratings partially cover the beam behind two of the three mirrors. This

---

[2]Details on XMM instruments and performances may be found: http://xmm.vilspa.esa.es/external/xmm_user_support/documentation/uhb/index.html.
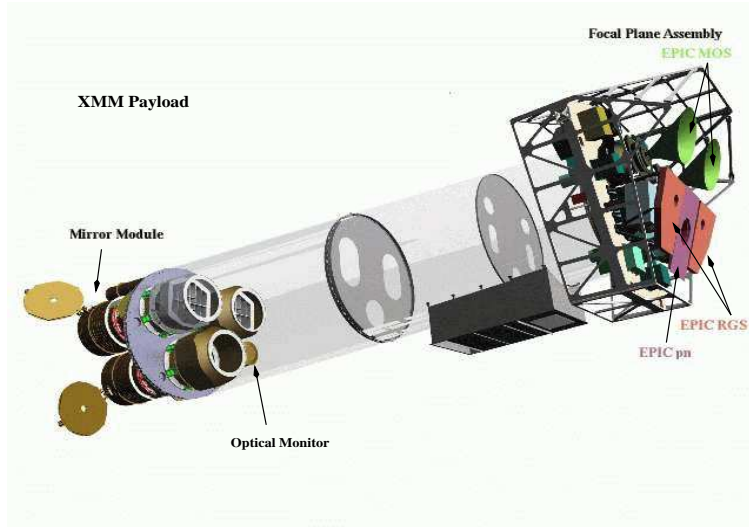
Figure 3.4: The XMM Payload. On the right hand side the X-ray instruments are indicated: the PN and the two MOS CCD cameras, plus the RGS spectrometers read-out cameras, coupled with the PN camera. (Courtesy of Dornier Satellitensysteme GmbH).

configuration offers the largest collective area over a wide energy band that has been so far achieved for an X-ray telescope.

3.2.1 The EPIC-pn camera

The EPIC-pn camera consists of a single wafer with 12 integrated back-illuminated CCD chips. The four individual quadrants each have three pn-CCD subunits with 200 x 64 pixels, operating in parallel. The pn array was designed for the XMM-Newton FOV (30$'$) and PSF having a total imaging area of 6 x 6 cm (97% of the field of view). The instrument performances are summarized in Table 3.2. As the EPIC detectors are not only sensitive to X-ray photons but also to IR, visible and UV light, the cameras include aluminised optical blocking filters to reduce the contamination of the X-ray signal by those softer photons. Depending on the instrument used, the effective area changes as described in Figure 3.5.

3.2.2 RGS the Reflection Grating Spectrometer

The RGS spectrometer consists of two identical units (RGS1 and RGS2). The diffraction geometry of a reflection grating is shown in Figure 3.6. The incoming rays hit the grating at an angle α and are reflected by an angle β which is given by: $cos\beta = cos\alpha + m\lambda/d$. Neither the undispersed spectrum nor positive orders are visible in the detector array, (*i.e.*, RGS works with ($\beta \geq \alpha$). The RGS Focal Camera is a

Table 3.2: In orbit performances of the CCD camera EPIC-pn on board XMM-Newton.

Bandpass	0.15-15 keV[1]
Sensitivity	$\sim 10^{-14}$ (erg/cm^2/sec)
Field of View	30'
PSF	6'' (FWHM)
Pixel size	4.1''
Timing resolution	0.03 ms
Spectral Resolution	$\sim$ 80eV at 1 keV

[1] Nominal bandpass

Table 3.3: RGS in-orbit performance parameters.

		RGS1	RGS2
Effective Area (cm^2) @15 Å	1st order	61	68
	2nd order	15	19
Resolution (km/s) @15 Å	1st order	1200	1400
	2nd order	700	800
Wavelength accuracy		$\pm$ 8mÅ	
Wavelength range	1st order	5-38 Å (0.35-2.5 keV)	
	second order	5-20Å 0.62-2.5 keV)	

linear array of 9 MOS CCD chips which are located along the dispersion direction of the RGS assembly. The FOV is 5' in the cross dispersion direction and covers the entire FOV of the mirrors in the dispersion direction. The total effective area was reduced by a factor of two in the wavelength range 20.1-23.9 Å and 10.5-14.0 Å as a consequence of the failure of an electronic component in the clock driver of CCD4 and CCD7 in RGS2 and RGS1, respectively. Important information on RGS performances are summarized in Table 3.3.

31
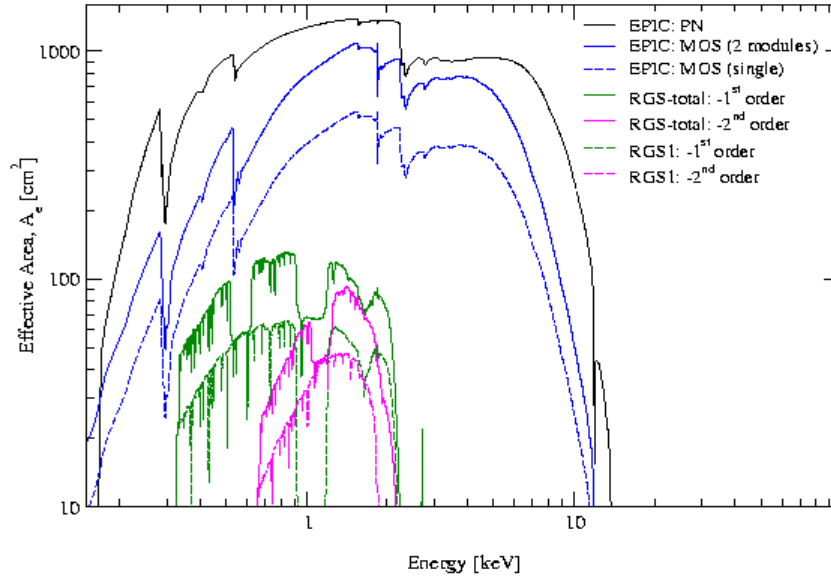
Figure 3.5: *The Effective area, in logarithmic scale, of the five instruments on board XMM. From top to bottom: pn, MOS 1+2, MOS(single), RGS 1+2 and RGS single (1st order), RGS 1+2 and RGS single, (2nd order).*
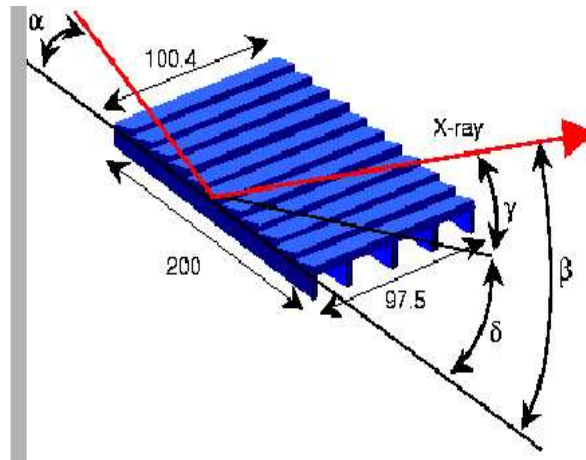
Figure 3.6: *Schematics of the RGS reflection gratings including some of the key dispersion angles.*

Chapter 4

Data Analysis

In this chapter, I review the calibration and data treatment needed to study scattering halos: faint extended emission in the foreground of a bright X-ray emitter. To appreciate the contribution of the halo, a precise knowledge of the Point Spread Function (PSF) behavior at all distances from the source and at all energies is essential. Moreover, the accurate subtraction of the source contribution to the halo emission requires careful evaluation of its absolute flux and spectral shape.

4.1 pile-up in CCD observations

When two or more photons hit a detector in a single frame time exposure, the event is recorded as a single event with energy equal to the sum of the photons. This causes the spectral shape of the source to be distorted in a highly non-linear manner. The resultant effect on the spectrum is depletion of the soft energies and an enhancement of the higher energies. Pile-up may also affect grating observations, causing the photons belonging to bright emission lines in the spectrum to be transferred to higher diffraction orders. In addition, pile-up also distorts the Surface Brightness Profile (SBP) of a source. If the pile-up is extreme, the information around the location of the peak of the SBP is completely lost. In Figure 4.3, an example is given. As all the incident events at the center are recorded as single events, the net effect is the characteristic "hole".

Recovering the flux value

Even though some correction methods have been developed, recovering the original shape is not trivial and depends on many boundary conditions that must be satisfied. For instance, the exact best fit model for the source should be known a priori (Davis, 2001). The absolute value of the flux and the spectral shape may be evaluated in indirect ways: *(i)* the grating data which, in the case of XMM, are always recorded

simultaneously or *(ii)* the collection of photons from the so called Out of Time Events (OOT) in the CCD camera itself. The latter are recorded during the read-out time, their exposure is 6% of the total exposure for XMM EPIC-pn and 1.3 % for *Chandra* ACIS. Given the relatively long read-out time for *Chandra* ACIS, it may be that for extremely bright sources, the OOT events are also piled up.

The grade migration

Finally, pile-up produces also the so-called "grade migration". In the *Chandra* analysis terminology the *grade* (*pattern*, in the XMM terminology) is a code that identifies which pixels, within a three-by-three pixel island centered on the local charge maximum, are above a certain amplitude threshold (for example, a single pixel event has grade 0). As the flux of the source increases, the fraction of the total number of events occupying a particular event grade changes as photon-induced charge clouds merge. The resulting detected event migrates to other *grades* which may not be included in the standard (G02346, for *Chandra*) grades and therefore missed in the analysis. The flux is thus underestimated.

A diagnostic tool for XMM CCDs takes advantage of the grade distribution, which can be precisely modeled in function of energy in the absence of pile-up. From a comparison of such a modeled distribution with a *real* grade distribution, the percentage of pile-up of a spectrum extracted from a given extraction region can be derived.

The above mentioned grade distribution, turned to be useful for the diagnose of pile-up also in the spatial analysis (*e.g.*, Gaetz, 2002), examining the radial profile of the source extracted for different grade events. When the count rate is low, far from the central source and thus pile-up free, the ratio of such profiles tends to a constant which depends on the spectrum. In Figure 4.9 an example is given for GX 5-1, where it is evident that up to $\sim 100''$, pile-up is a noticeable problem.

4.1.1   MIPs and Pseudo-MIPs in XMM-Newton CCDs

The event analyzer in the EPIC-pn camera aboard XMM-Newton is able to discriminate MIPs (Minimum Ionizing Particles) from X-ray events in order to reduce telemetry and background rates (Freyberg, 2003). These events are caused by high-energy particles (e.g., α particles and protons) and penetrate the detector creating electron-hole pairs. The energy loss per unit length is minimal for high-energy particles (about 80 electron-hole pairs per μm). The corresponding charge in a pixel is very high and the amplitude can be used to identify and screen such events: in the case of EPIC-pn, pixels in a read-out frame with amplitudes > 3000 adu (~ 15 keV) are flagged as MIPs. Subsequently all events in this CCD column of this particular frame are rejected as

well as all events in both neighboring columns (immediately right and left) of this column. The number of rejected columns in each quadrant accumulated over 20 frames is recorded ("discarded line counter") and used as time-resolved (in full-frame mode about 1.5s) exposure correction. At the end of each exposure the total number of rejections of each column is written into a "discarded line file" (DLI, Figure 4.1) where each element is stored in 16 bit. In principle, this DLI file could be used to correct for spatial inhomogeneity in the MIP distribution; however, under normal conditions the CCD columns 2 to 63 (all CCD columns but the edge column) are found to be evenly affected.

A very bright source can produce so much charge in a pixel due to pile-up that this triggers the MIP-rejection scheme described above ("pseudo-MIPs"). Then, preferentially in the core of the PSF, more CCD columns are rejected than outside. This spatial exposure inhomogeneity is not automatically accounted for (the EXPOSURE extensions contain only temporal but no spatial information). Moreover, these rejected columns also affect the determination of the flux from the out-of-time events as these also occur in the columns correspondent to the PSF core. Finally, the 16-bit-entries of the DLI file, that could in principle monitor the spatial exposure inhomogeneity, are subject to overflows in the case of long exposures, exposures with very high background, and especially in the case of pseudo-MIPs. In the latter case they can overflow many times and the exact number of column rejections remains uncertain by multiples of 65536 (the maximum number of column rejections is of course the total number of read-out frames in this exposure, i.e. $t_{\mathrm{exp}}/t_{\mathrm{frm}}$). To investigate the pseudo-MIPs a simulation program, described in Appendix A, was used where the position, brightness, and spectrum of an X-ray source can be input, and the resulting DLI file can be checked for the spatial profile and possible overflows.

4.2 The PSF mirror scattering wings

The study of scattering halos relies on an accurate PSF subtraction. The spatial response of the instrument may be divided into two components. A Gaussian, whose full width half maximum (FWHM) is the nominal spatial resolution of the instrument, plus the scattering of the telescope mirror which is described by a King's profile :

$$PSF = A \left\{ \frac{1}{\left[1 + \left(\frac{r}{r_c} \right)^2 \right]^{\alpha}} + BKG \right\}, \qquad (4.1)$$

where α is the King's slope and r_c is the core radius of the main King component. For our purposes we are most interested in the outer shape of the PSF, where the halo is detected.
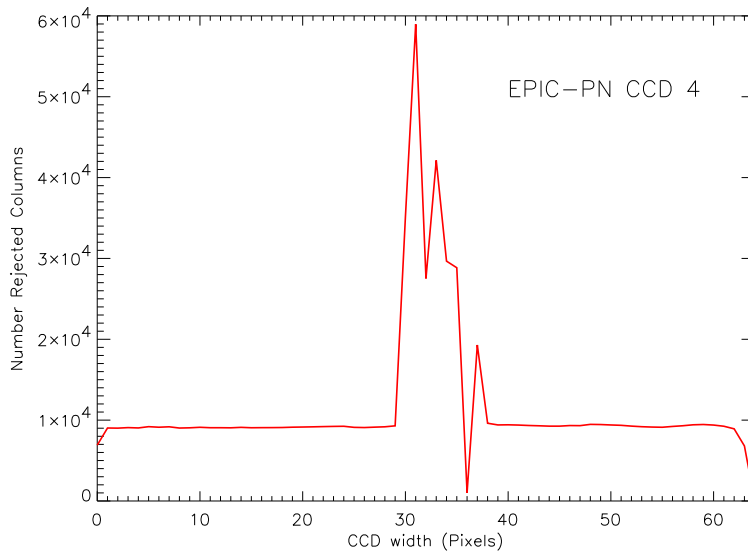
Figure 4.1: *Discarded line plot for EPIC-pn CCD number 4 (where the source is typically located), for Cyg X-2.*

4.2.1 XMM EPIC-pn PSF

Using a set of bright, but "non-piled-up" sources, Ghizzardi (2002), found that for the pn camera the parameters for the King's profiles are:

	1.5 keV	8 keV	9 keV
r_c	$6.18''$	$4.18''$	$3.88''$
α	1.50	1.40	1.39

The King's profile parameters were found to vary as a function of energy for on-axis sources according to the relations:

$$r_c(E) = 6.636(0.020) - 0.305(0.032) \times E$$
$$\alpha(E) = 5.525(0.001) - 0.015(0.001) \times E.$$

The on-ground calibrated PSF wings, which may be simulated by the SciSim XMM simulator[1], agrees to a good approximation with the in-flight calibration model (Figure 4.2). The error bar is the poissonian error on the number of counts.

As a main reference, I chose an in-flight calibration source, the bright, low N_H object Mkn 421. The quasar PKS 0558-504 was chosen for comparison (Table 4.1). Mkn 421 was observed in special masking mode, i.e. a squared patch $50''$ wide was located on the core of the source in order to avoid possible pile-up in the OOT events

---

[1]http://xmm.vilspa.esa.es/scisim/
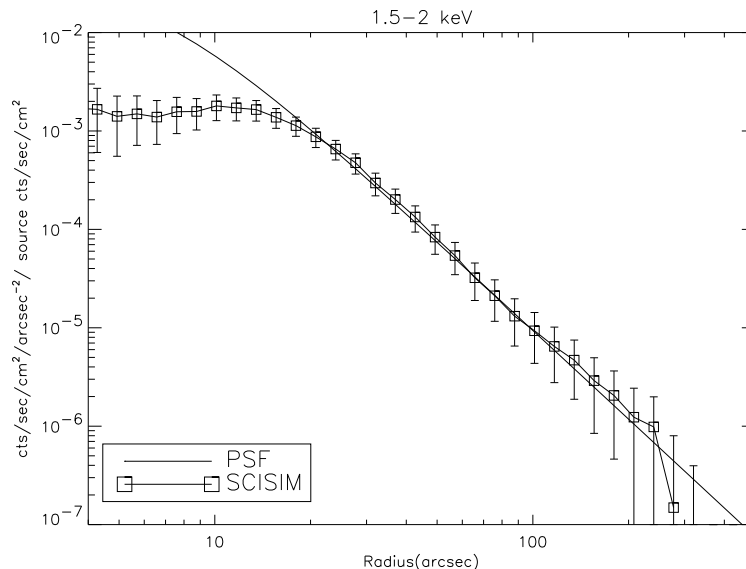
Figure 4.2: The simulated point source using `scisim` *in the energy range 1.5-2 keV is in good agreement with the model by Ghizzardi (2002). At lower radii the pile-up of the simulated source is visible.*

and pseudo-MIPs. Nevertheless, pile-up affects the bright region around the core up to a radius of $c.40''$. The statistics of Mkn 421 was actually high enough to create profiles in energy bins ~ 100 eV wide, providing the best estimate of the profile used for comparison with the XMM halo sources presented in this thesis. In Figure 4.3 we show a comparison between the King model, Mkn 421 and PKS 0558-504 within two energy ranges of interest for the study of the halos. It can been seen that a high count rate source over a broad energy band is needed for a reliable determination of the PSF shape.

We found that the PSF does not change dramatically in the energy range 0.3-2 keV (Figure 4.4), where scattering by dust usually plays a role, at all distances from the source. At outer radii, a deviation of the spectral shape is noted at higher energies. Indeed the integral below the PSF profile at outer radii increases and the slope flattens. The lower limit of the energy range is set by the reliability of the response of the instrument at the present time.

4.2.2 *Chandra* ACIS PSF

The determination of the PSF "wings" for ACIS-S was more complex. The Chandra HRMA consists of four nested Wolter type I grazing incidence optics (Chapter 3), each consisting of a paraboloidal mirror and a hyperboloidal mirror. These are referred to as "mirror pairs" or "shells" interchangeably. The overall image aberrations

37
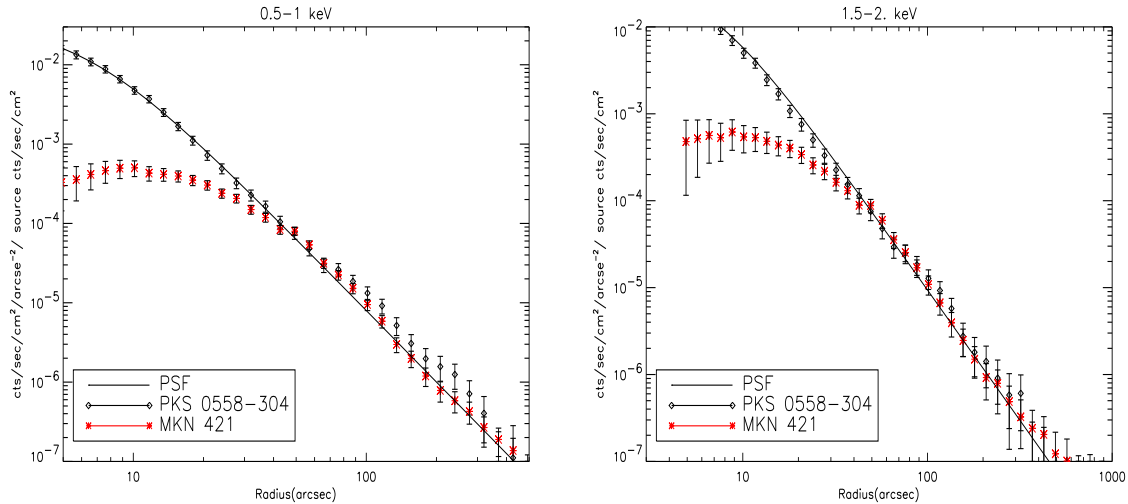
Figure 4.3: Comparison between the model (solid line), Mkn 421 (asterisks) and PKS 0558-504 (rhombus) between 0.5 and 1 keV (left) and 1.5-2 keV (right). We see the deviation of the PKS 0558-504 from the model at larger radii due to unsufficient statistics.

Table 4.1: Parameters of interest for our XMM calibration sources

source	Exp	Rate$_{[0.5-2\mathrm{keV}]}$	N_H	b
	ksec	cts/sec	10^{20} cm^{-2}	deg
Mkn 421	14	220.6	1.38	+38.2088
PKS 0558-504	10	16.4	4.39	-50.4475

induced by misalignments within the optics is quite well reproduced by the on-ground calibration, while modeling the scattering has been proven to be more problematic. The scattering function is based on detailed metrology of the roughness of the optics. The center of the optic (typically about 80%) is smoothest, with increasing roughness toward the edges. Mirror pair 1, the largest mirrors, also have the roughest surfaces. The scattering model is still under refinement for it tends to considerably underestimate the observed scattering wings (as shown in Figure 4.7).

For the in-flight calibration, I chose at first a set of four observations of bright quasars lying away from the galactic plane and having a mean column density of $N_H \sim 2 \times 10^{20}$cm^{-2}. A log of the observation is shown in Table 4.2. The core of all of the sources were piled-up, but the statistics in the OOT events enabled the evaluation of the flux in bins larger than 0.5 keV. The determination of the PSF was unsatisfactory for low energies since the sample lacked of a real "soft" source. The uncertainty is shown in Figure 4.5 indicating the SBP of the QSOs sources (lower panel) as well as the ratio of the minimum and maximum dispersion (upper panel).

In July 2002, Her X-1 was observed, an ideal target for this calibration purpose (Gaetz
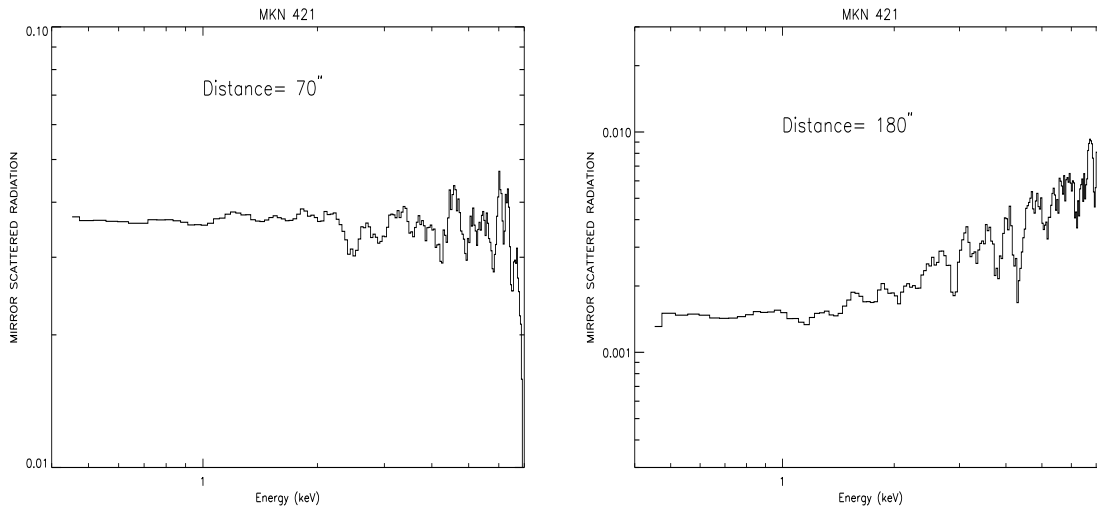
Figure 4.4: XMM EPIC-pn pure scattering mirror spectrum at 70″ (left) and 180″ (right) extracted from the halo-free source Mkn 421. We note a smooth increase of the scattering above 2 keV for larger radii. Neither spectra is divided by the extraction area.

2002). Indeed, the wings of this very bright source were actually detected in the image against the background emission.

The surface brightness profile was extracted using the procedure described in §4.3.2 and also in this case, due to pile-up, the source flux had to be evaluated by the OOT events. From the in flight calibration the slope of the wings can be described by a power law: θ^γ, where θ is the angular distance from the source. The index γ is steep for low energies and maintains approximately a value of 2 until $\sim$ 5 keV. The increasing steepness above 5 keV is likely due to the loss of effective area due to the roughness of the outer and largest mirror (the Mirror pair 1). Above 8 keV the statistics is insufficient to determine the slope with any accuracy (Figure 4.6).

The mirror scattering as function of energy at a given radius can be also evaluated. In Figure 4.8 the pure mirror scattering spectrum for Her X-1 is shown at a distance of 100″ from the source. The extraction procedure will be fully described in §4.3.4. The spectrum stays fairly constant until $\sim$1 keV and then it steepens with a power law slope of $\sim$1.33 up to 5 keV. Above this energy we note the same anomaly as for the PSF shape (Figure 4.6). The spectral distribution of the PSF mirror wings is important to properly subtract the instrumental contribution from the halo at each energy. Such subtraction allows us to determine the continuum of the scattered radiation as well as to detect possible spectral features from dust.

Table 4.2: Main parameters for the Chandra sources chosen for the PSF's wings calibration.

source	Exp	N_H^1	A_V	b
	ksec	10^{20} cm^{-2}	mag	deg
NGC 3783	57	8.5	0.4^2	–37.73
3C 273a	39	1.7	0.08^2	+2.05
3C 273b	26	1.7	$0.08^{\ 2}$	+2.05
PKS 2155-304	27	1.7	0.08^2	–30.22
Her X-1	50	1.8	0.05^3	+37.52

[1] Dickey & Lockman (1990)
[2] From the Bohlin et al. (1978) relation $N_H \approx 1.9 \times 10^{21} A_V$ cm^{2}mag^{-1}
[3] Liu et al. (2001)
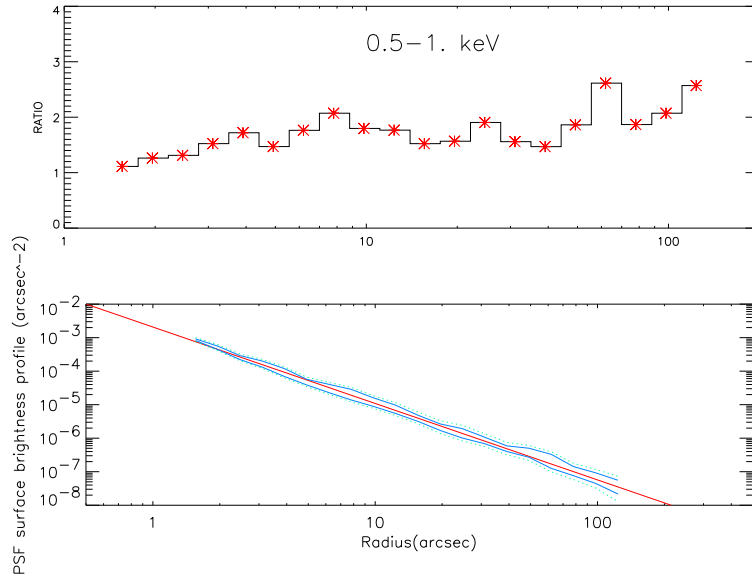
Figure 4.5: SBP of the QSOs listed in Table 4.2 in the energy range 0.5-1 keV (lower panel) and the ratio between the minimum and maximum value for each radial distance (upper panel).
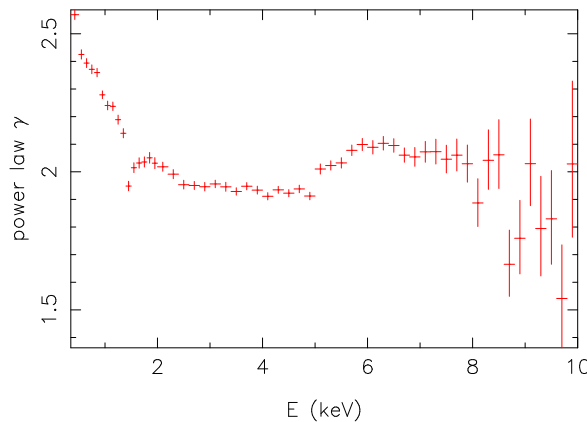
Figure 4.6: The powerlaw index which describes the scattering wings of the Chandra mirrors as function of energy (courtesy of T. Gaetz).

4.3   Data treatment

• The description of the data manipulation applies to all the XMM sources studied in the present work. I processed the data using the XMM-Newton Science Analysis Software (XMMSAS ver 5.4.1) and *ad hoc* programs that I developed for specific issues. From pn camera data I extracted the spatial information and the broadband (albeit at low resolution) spectrum of both the source and the halo. The RGS provided the high resolution energy distribution of the central object, from 0.35 to ∼1.7-1.8 keV. Both EPIC-pn and RGS data were available (Chapter 3), nevertheless, due to the extreme brightness, the central camera of EPIC-MOS was completely saturated and thus not usable.

• The data treatment for extended sources observed by the CCDs on board *Chandra* is very similar to the one of XMM-EPIC. The data were processed using the CIAO software ver. 3.0. For all the halo sources of the *Chandra* sample I studied the ACIS-S and ACIS-I data in the band ∼0.5-8 keV. On the other hand the High Energy Transmission Grating (HETG) has been used for a different sample of sources.

4.3.1   The physical parameters of the central source

All of the sources here considered are affected by pile-up. Therefore for both the absolute flux determination and the spectral shape of the central source the data treatment needed to be performed individually, tailored for each source.

   The EPIC-pn images are affected by a noticeable pile-up (§4.1) at the center of the source. The calibration source Mkn 421 was observed in the special masked mode[2],

---

[2]The central 10x10 pixels of the source are obscured during the observation. This prevents the

Profiles: 1.4-1.5 keV
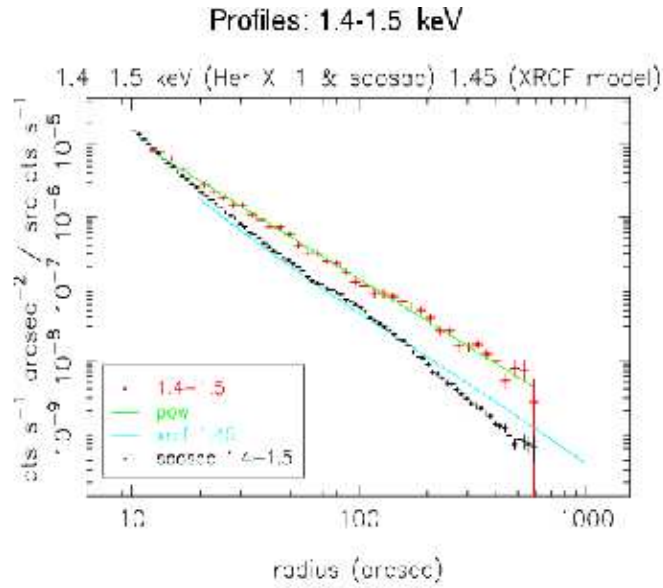
Figure 4.7: The difference between the in-flight determined PSF wings profile and the simulation based on a theoretical scattering model (courtesy of T. Gaetz).
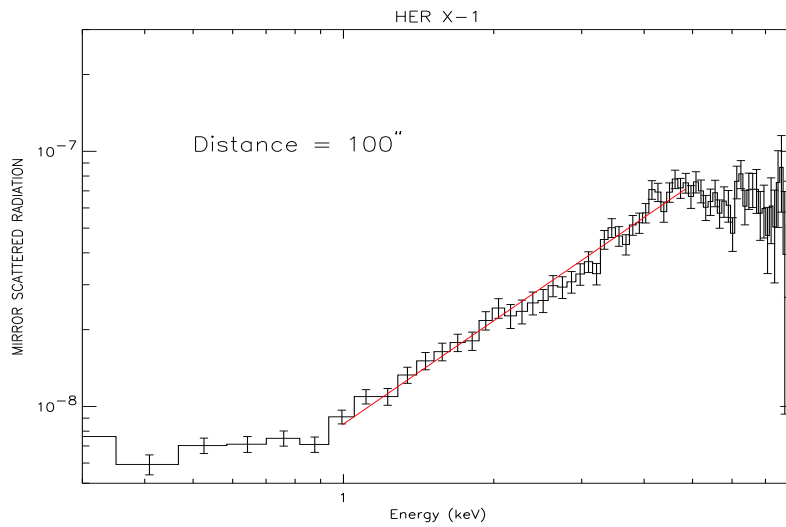
Figure 4.8: The pure mirror scattering spectrum per unit area at a distance of $100''$ from the source extracted from Her X-1.

42

enabling the true flux to be completely recovered as well as the spectral shape from the OOT events. Conversely, the OOT events in the observation of Cyg X-2 and GX 339-4[3] were affected both by pile-up and column rejection due to pseudo-MIPs. Since the pile-up of the OOT was marginal, once the central columns were eliminated, at least the spectral shape could be recovered. The absolute flux was evaluated both from the RGS spectrum and by the pseudo-MIPs simulation program described in detail in Appendix A (for Cyg X-2 only). The EPIC-pn count rate was simulated unfolding the best fit model of RGS by the pn response. However, the application of this procedure resulted in a flux increase of 21%. Recent EPIC-RGS cross correlation analysis show an increase of a similar magnitude (Pollock, 2003). However, the ultimate test on the flux of EPIC-pn halo sources was the comparison of the halo profile level with Mkn 421 profile, whose absolute normalization was accurately determined.

In *Chandra* observations, the gratings are not employed simultaneously, therefore no additional information of the source flux comes from the gratings data (as for XMM). The source flux has to be evaluated from only the OOT events in the CCD observation. The OOT events are recorded in 4.1×10^{-4}sec/pixel. Given the longer frame time (3.2 sec), the pile-up in ACIS observations is an even a more frequent event than for EPIC, however, the pseudo-MIPs phenomenon does not occur in *Chandra* observations.

4.3.2 Halo spatial analysis

The analysis of a source's extended emission, at a basic level, means studying the surface brightness profile of the source and compare it with the instrumental PSF. The reminder between the profiles and the PSF is the halo diffuse emission.

Pile-up handling

First of all, in order to evaluate the dependence of pile-up as a function of the distance from the source (§4.1), I extracted the radial profile of the source at different energies for single events, double events and the total events, selecting different *pattern* from the data. I selected an area extraction[4], in order to guarantee that the energy response stays constant across the detector (for XMM EPIC-pn). Where the count

---

occuring of pseudo-MIPs in the central columns as well as pile-up in the OOT events.

[3]The special masking mode for GX 339-4 failed. The observation was concluded without an automatic procedure leading to a considerable loss of data including the DLI file §4.1.1.

[4]the RAW CCD coordinates selection was:Y=180-199. This RAW Y range always contains the source, if it is observed on-axis, and allows us to avoid the uncertainties related to the RAW Y dependence of the energy response.

rate is low, (i.e. no pile-up) the ratio of the radial profiles, extracted with different *patterns*, should tend to a constant which depends on the spectrum.

For *Chandra* data the same "grade migration test" was applied to the radial profile using as a reference, the ratio of grade 0 and grade 6 to all the ASCA standard grades: 02346 (Chapter 3) over all the chip area containing the source. In Figure 4.9, I show such ratios, as a function of the angular distance from the source, for GX 5-1, along with the constant value one should find in absence of pile-up. The selected energy was 2 keV. In this (extreme) example, the pile-up is non-negligible up to $\sim 90''$ from the center. Therefore I excluded all the photons within the pile-up radius from the analysis of all sources.
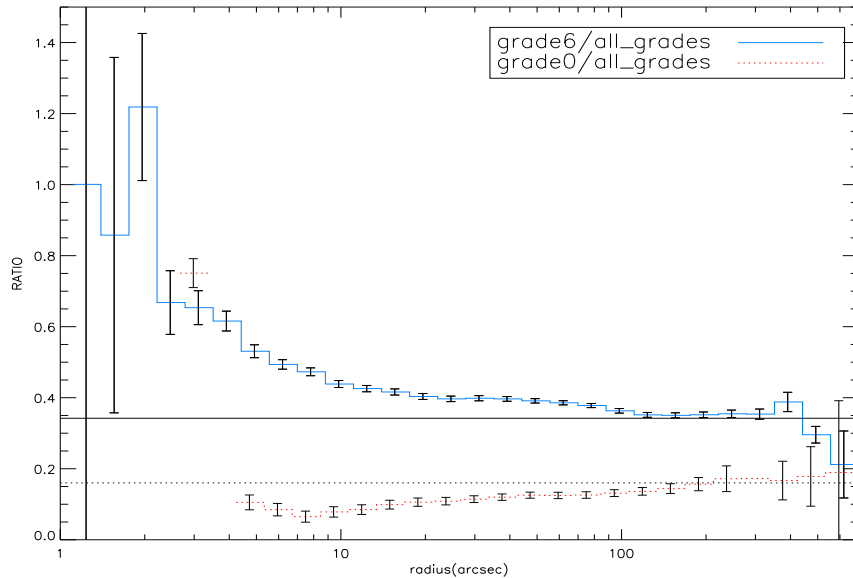
Figure 4.9: The ratio grade 0/totalgrade (solid line), grade 6/totalgrade (dashed line) in function of the radial distance from the source (in arcsec) for the Chandra ACIS-S observation of GX 5-1. The horizontal lines show the expected value for G0 (G6) events far away from the source. Within $\sim 90''$ pile-up is a noticeable problem.

The surface brightness profile (SBP) extraction

The XMM-Newton PSF behavior was described in §4.2.1. In XMM EPIC-pn, the source photons were extracted by dividing the region around the central source in concentric, logarithmically spaced rings. Each photon, at a given energy and coordinates, was vignetting and exposure corrected[5]. The exposure map also corrects for

---

[5]The tool for vignetting correction weights each photon for the inverse of the ratio between the effective area in that position and energy and the effective area at the aim point of the detector.

the chips gaps and hot pixels on the detector. The background, also vignetting and exposure corrected, was extracted from an outer ring.

For the *Chandra* observations, approximately the same procedure applies: the SBP was divided by the mean exposure map, at each selected energy and distance from the source. The exposure map calculation includes the exposure time, the Quantum Efficiency convolved with the filter transmission (BI or FI chip) as well as the effective area across the CCD. For consistency, the counts extracted from OOT events were divided by the value of the exposure map at the position of the source. Both the SBP and the PSF (the point-like source Her X-1), were background subtracted. In the case of ACIS-S + HETG observations, the exposure map was also corrected for the grating contribution, which decreases the effective area of the zeroth order photons by a mean factor of about 6. The lines formed by the dispersed photons and the read out streak where removed from the image before extracting the profile.

For each source, either observed with *Chandra* or XMM, I eliminated the serendipitous detections in the field. The list of serendipity objects was found using the SIMBAD database[6]. Other spurious features in the CCD, such as the out of time events, were also taken out. The surface brightness profile was calculated by dividing the number of photons in a ring by its area (in arcsec), corrected for the area of the serendipitously detected sources.
The number of energy dependent SBFs depends of course on the statistics. For bright sources (namely Cyg X-2 , GX 339-4 , GX 5-1), the halo could be studied at all energies from 0.5 to 2-3 keV, keeping the energy bin as small as the energy resolution of the instrument. Once divided for the absolute count rates, as determined above, the extended emission, measured in $arcsec^{-1}$, can be compared with the PSF at the relative energy.

4.3.3 Convolution

In principle the halo emission would be the deconvolution of the data with the PSF according to:

$$g * h \equiv \int_{-\infty}^{+\infty} g(\tau)h(t - \tau)d\tau, \tag{4.2}$$

where g is the observed function and h the PSF, for example. The *Convolution Theorem* makes the computation of Equation 4.2 straightforward:

$$g * h \Leftrightarrow G(f)H(f), \tag{4.3}$$

---

[6]http://cds-strasbg/simbad

where $G(f)$ and $H(f)$ are the *Fourier Transforms* of $g(t)$ and $h(t)$. These are easily computed via discrete Fast Fourier Transform (Press et al., 1992). I compared the resulting halo with a halo profile obtained subtracting the PSF from the observed data. The difference between the two methods is of the order of 1-2%. This is well below the uncertainties introduced by various assumptions on the dust distribution and chemistry, on the scattering mechanism and the quality of the X-ray data. Throughout this work, for a sake of simplicity, I did not deconvolve the data from the PSF, but I extracted the halo simply subtracting PSF wings from the data.

4.3.4   Halo spectral analysis

For the brightest sources, the high statistical sampling allowed me to study in detail the *halo* spectral shape as a function of energy. For this purpose, I considered the radial distance from the source going from the pile-up radius (§4.3.2) to the full extension of the halo ($\sim$4-6$'$ depending on the source) divided in rings of roughly 1$'$. I estimated the background in an outer annulus of $\sim 2'$ width, avoiding the read-out streak region (i.e. the OOT events region).

For XMM-EPIC camera, in the extraction I took into account the different exposures for each quadrant of the detector, selecting just the time intervals when all the CCDs were switched on at the same time, to have an homogeneous exposure throughout the detector. I selected then only RAWY> 180, to avoid uncertainties related to the RAW Y dependency of the response matrix (§4.3.2). In order to have a model independent estimate of how the halo spectra may change as a function of the distance from the source, I normalized the ring's spectra for the source spectrum, estimated from the OOT events (§4.3.1). In this way all the features belonging to the X-ray emitter itself cancel out. In absence of any additional extended emission, the result must be a constant. The same procedure was applied to the PSF data: the point-like source Mkn 421. The PSF data were from real, though high statistics, data, and thus affected by noise. Thus, in order not to lose information on the halo emission, the PSF spectrum was smoothed (as in Figure 4.4) before subtracting it from the data.

For Chandra the halo spectral analysis was hampered by a lack of calibration in the Charge Transfer Inefficiency (CTI) correction for CCD number 7, the chip where the source is located when observed with ACIS-S. The effect of the CTI is to broaden and shift in energy any spectral feature emphasizing this effect going towards the read out node. Moreover, the CTI correction of the true source position cannot be applied to the events taken from the read out streak, orthogonal to the read out node. This makes impossible to compare spectra taken from different regions of the detector with the spectrum of the central source, unless we are interested in the continuum shape

only.

4.3.5 The halo modeling

In this thesis, the modeling of both the halo profile and the halo spectrum was carried out using a procedure non implemented in the *Chandra* and XMM standard analysis.

The halo emission obeys eq 2.7. I calculated the differential scattering cross section ($d\sigma/d\Omega$) using both the Rayleigh-Gans approximation and the complete Mie theory for scattering by spherical particles (§§2.5.2,2.5.1). The code[7] (Wiscombe 1980) used to generate the scattering cross sections is reliable until $X = 2\pi a/\lambda < 2 \times 10^4$. For large values of a (say $a > 1.2\mu m$ for $E = 2$keV), anomalous diffraction theory should be used (van de Hulst 1967). However we ignore such very large grains in our calculation since, as shown in Tan & Draine (2002), radii $> 0.4\mu m$ contribute less than 1% at large scattering angles and less than 20% for $\theta_{sca} < 100''$. We also restricted the halo modeling to E< 2 keV. For the geometry of the system, always holds: $\theta_{sca} > \theta_{obs}$, but in practice we consider $cos(\theta_{sca} - \theta_{obs}) \to 1$ (Smith & Dwek 1998).

I calculated the differential scattering cross section considering refraction indices for 10 different elements and compounds that are likely to be found in the ID[8]. The dust sizes ranged from 0.005μm to 0.4μm in 20 steps, logarithmically spaced. The energy range was 0.1-2 keV in 221 steps.

The dust size distribution models used were the MRN model (§2.9) and the WD01 model (§2.10). In the former, the slope was constrained to range between -3.2 and -4, while the minimum and maximum for z and a were left as free parameters. The WD01 model was applied using a range of best fit parameters stated in Weingartner & Draine (2001). The distribution of very small carbon grains was neglected here, given that the C region is outside the range of the observed data. Once again z was left free to vary.

In the case of the radial profile analysis, the energy is fixed, while the dust size distribution $n(a)$ and the differential scattering cross section ($d\sigma/d\Omega$) are integrated over the grain size a. The differential scattering cross section is also dependent on z, the fractional distance at which the scattering occurs. The parameter z allows one, in principle, to distinguish between smooth and evenly distributed dust and a "clumpy" structure along the line of sight. The normalization was left as a free parameter. The agreement between the calculated intensity *vs* scattering angle is then compared to the data through the χ^2 test (eq. 4.4).

Conversely, in the spectral analysis, the scattering angle is fixed, since the spectrum is extracted from a thin annulus around the source. After the integration of $d\sigma/d\Omega$ and $n(a)$ over the grain size, for each element and compound, the best fit with the data

---

[7]ftp://climate.gsfc.nasa.gov/pub/wiscombe/Single_Scatt/Homogen_Sphere/Exact_Mie/

[8]Namely: C, Mg, Si, Fe, Mg_2SiO_4 , $FeMgSiO_4$, Fe_2SiO_4, $FeSiO_3$, $MgSiO_3$ (Whittet 2003).

was found through a linear combination of the single halo intensities. The goodness of fit was also evaluated minimizing the χ^2.

4.3.6 The grating data

The XMM-RGS data were filtered from possible background flares. The extraction region of the background spectrum was carefully chosen not to include any halo emission. I extracted the first and second order from RGS1 and RGS2 for a total of four data sets. The data below 7Å are affected by low, non-calibrated, sensitivity and had to be rejected.

Where *Chandra* gratings are concerned, dealing with high count rates, the HETG Data Analysis was hampered by pile-up. For some of the sources the exposure time was distributed in two alternate frame time modes, a very short frame time (0.4 sec)for a short total exposure (few percent of the total time), in order to have a low statistics, but not piled-up spectrum and a longer frame time coupled with a longer total exposure. The lower exposure spectrum provides a reliable estimate of the total flux and of the shape of the continuum and constitutes a direct way to check pile-up in the longer exposure observation. For other sources,in order to reduce the amount of incoming photons, it turned out to be more convenient to put a filter on the position of the 0th order.

For both XMM and *Chandra* gratings, the resulting spectrum has an associated response matrix and effective area, specific to the instrument and the grating order. The spectrum is then corrected for the background emission and rebinned (a minimum of 20 counts per bin is necessary to apply the χ^2 test). The spectral analysis was carried out using the XSPEC (ver.11.1) package. The best fit model was decided on the basis of the minimization of the χ^2:

$$\chi^2 = \sum_i \frac{(m_i - x_i)^2}{\sigma_i^2} \tag{4.4}$$

Where x are the data and m the model points. σ^2 is the standard deviation (Bevington & Robinson, 2003).

Chapter 5

The XMM view of interstellar dust

5.1   Motivations

As described in §3.2, XMM-Newton stands apart from other X-ray observatories due to the large collecting area (Table 3.2) of its mirrors. This, coupled with an improved spatial resolution with respect to the ROSAT PSPC ($\mathrm{FWHM_{EPIC-pn}} < 12''$) makes it suitable to study fainter halos. The detection and the analysis of a halo is dependent upon two competing effects: on one hand, the higher the column density the brighter the halo (more dust produces more scattering); on the other side, more dust in the line of sight implies more absorption, according to $I = I_0 e^{(} - \sigma\ N_H)$ (see Chapter 2). For line-of-sight column density N_H above $\sim 6 - 7 \times 10^{22} \mathrm{cm}^{-2}$, all the photons in the energy region of interest for the scattering (up to $\sim$2.5 keV) will be absorbed, rather than scattered.

Sources with faint halos lie behind a hydrogen column density which is low enough to not completely absorb the soft energy emission. Indeed in the energy range 0.3-2 keV, many absorption features of ID components may appear, primarily oxygen (0.53 keV), magnesium (1.3 keV), silicon (1.87 keV). An energy resolution of $\sim$80 eV over a broad energy band (nominally 0.1-10 keV) makes it possible to spectroscopically investigate the features of a faint halo emission (*e.g*, 4-5% of the total emission of the source measured aat soft energies) with high signal to noise ratio down to 0.3 keV (depending on the degree of the absorption and possible instrumental uncertainties). In this section, I present the imaging and spectral results pertaining to two bright ($L \sim 10^{39} \mathrm{erg\ s}^{-1}$) X-ray binaries, Cyg X-2 and GX 339-4 , observed by XMM-Newton as guaranteed time (GT) targets.

Table 5.1: Observation parameters for Cyg X-2 and GX 339-4

source	exp (ksec) PN[1]	exp (ksec) RGS[1]	count rate RGS[3]
Cyg X-2	7.298	10.683	44.55±0.06
GX 339-4	0.869	2.588	35.8±0.2

[1] exposure times are filtered by background temporal inhomogeneities (Chapter 4).
[3] first order mean count rate from RGS1.

5.2 Data analysis

Table 5.1 lists the observation parameters for Cyg X-2 and GX 339-4 . The data treatment has been fully described in Chapter 4. The excluded pile-up region was within $\sim 50''$, $\sim 10''$ for Cyg X-2 and GX 339-4 , respectively, while the halo extension is up to $4'$ and $6'$, respectively.

5.3 Cyg X-2

5.3.1 Broad-band spectrum

An accurate modeling of the broad-band spectrum, especially at soft energies, permits the inference of the value of the total hydrogen column density along the line of sight, an important parameter for the study of ID.

In Table 5.2 the best-fit parameters for the spectrum of Cyg X-2 are shown. The soft spectrum is well fitted by a multi-temperature black body for the accretion disk emission (DISKBB in XSPEC, Mitsuda et al., 1984) plus a comptonized black body spectrum for the emission of the neutron star (COMPTT in XSPEC, Titarchuk, 1994). The soft (seed) photons have a temperature T_0 and are led to a temperature T through Compton scattering within an electron cloud of thickness τ (Piraino et al., 2002; Di Salvo et al., 2002). At $\sim$6.7 keV, the fit requires a Gaussian component, identified as the fluorescence He-like Fe emission line from an accretion disk, possibly from ionized material. The soft spectrum experiences both photoelectric absorption (TBABS in XSPEC, Wilms et al., 2000) and scattering by ID *i.e.*, light is diverted from our line of sight, "subtracting" photons from the central source spectrum (PS95), The scattering correction is based upon the empirical relations: $\tau_{sca} = 0.05 N_H - 0.083$ and $A_V = 0.56\ N_H + 0.23$, where τ is the scattering optical depth and N_H is in units of 10^{21} cm^{-2}. The optical extinction A_V value is only 1.3 for Cyg X-2 , therefore the influence of the scattering on the spectrum is almost negligible (-0.0210^{21} cm^{-2}) in the fit for such low intervening column densities at least for energies >0.4 keV (PS95).
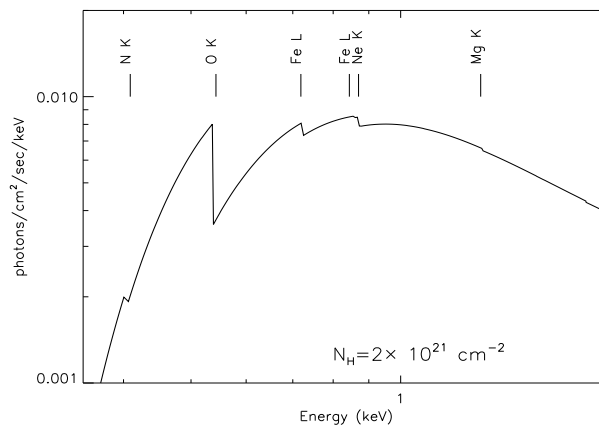
Figure 5.1: ISM absorption edges predicted for $N_{\rm H} \sim 2.2 \times 10^{21} {\rm cm}^{-2}$. Mg and Si are only marginally evident in the model.

5.3.2 RGS spectrum

As the RGS only covers the 0.35-2 keV band, the hard component cannot be constrained, therefore I fixed the thermal comptonization parameters to the EPIC-pn best-fit values. The measured total equivalent hydrogen column density $N_{\rm H}$ of 2.20 ± 0.02 $10^{21} {\rm cm}^{-2}$ predicts absorption edges from K shells of nitrogen, oxygen, and neon and also from L shell of iron, as shown in Fig 5.1. In the present data, the statistics enable the physical parameters of the absorption by those elements to be measured. For each element j, I calculated the column density $N_j = \tau_j / \sigma_j$ using the photoelectric cross section calculated from tabulated values (Henke et al. 1993). The optical depth τ_j was extracted adding an absorption edge model to a continuum were the abundance j was fixed to zero. Using the the ISM abundances listed by Wilms et al. (2000), I derived the equivalent hydrogen column density. The column densities are not tightly constrained for all elements. In general, within the errors, I find an agreement with the $N_{\rm H}$ found in our best-fit model (Table 5.3). On the other hand we note that iron, which is measured with the best accuracy, shows an overabundance of $\sim 20\%$ compared to the ISM value.

Takei et al. (2003) found a complex structure for the oxygen edge region in a *Chandra*-LETG observation of Cyg X-2 . In their analysis they noted the atomic and compound contribution in the absorbed spectrum (model 2 in Table 5.4). Although RGS's energy resolution is approximately 44% less than LETG, I find a similar complexity in the oxygen region. In particular a single oxygen edge model unsatisfactorily fits the data, while an additional edge improves the fit by $\Delta\chi^2/\Delta\nu = 39/1$ (corresponding to a significance higher than 99.5%). The two edge energies are fixed: 0.536

Table 5.2: *Best-fit parameters for the spectrum of Cyg X-2 in the energy band 0.3-10 keV, with a disk black body at temperature kT_{db} and a comptonized spectrum, affected by extinction of gas and dust. Errors are given at 90% confidence level for one interesting parameter. kT_e is the electron temperature and τ is the optical depth of the electron cloud that comptonizes the soft photons at temperature kT_0 (keV).*

N_H ($\times 10^{22}$ cm^{-2})	0.21 ± 0.05
kT_{db} (keV)	0.36 ± 0.05
kT_0 (keV)	0.81 ± 0.03
kT (keV)	6.2 ± 0.1
τ	1.62 ± 0.07
E_{Fe} (keV)	6.67 ± 0.16
σ_{Fe} (keV)	$0.2^{+0.3}_{-0.1}$
EQW_{Fe} (eV)	73 ± 53
χ^2/dof	$1115/1111$

Table 5.3: *Relevant absorption edges in RGS spectrum of Cyg X-2 . The energy, the corresponding wavelength, and the optical depth (τ) were measured from the data. The equivalent total hydrogen column density N_H was derived from the ISM abundances of Wilms, Allen & McCray (2000). These are to be compared with the best-fit $N_H = 2.20 \pm 0.02 \ 10^{21}$ cm^{-2}.*

Element	Energy (keV)	Wavelength (Å)	τ	$N_H(10^{21})$
N K-shell	0.409 (fixed)	30.31	0.15 ± 0.06	2.7 ± 1.1
O K-shell	0.543 (fixed)	22.83	0.45 ± 0.1	1.6 ± 0.4
Fe L-shell	0.706 ± 0.01	17.56 ± 0.02	0.13 ± 0.01	2.8 ± 0.2
Ne K-shell	$0.869^{+0.02}_{-0.06}$	$14.26^{+0.10}_{-0.03}$	0.06 ± 0.03	1.8 ± 0.9

(22.11) and 0.543 (22.83) keV (Å), corresponding to compound and atomic oxygen, respectively. On the other hand, a third edge, strongly required by LETG data at 0.549 keV (atomic oxygen), here improves the fit of $\Delta\chi^2/\Delta\nu = 5/1$ (significance 97.5%). At an energy of 0.524 ± 0.003 keV, consistent with the atomic oxygen $1s - 2p$ transition, an absorption line of equivalent width (EW) $1.45^{+0.22}_{-0.14}$ is clearly detected. Finally, at 0.530 ± 0.003 keV some absorption line-like residuals, in addition to the known instrumental absorption line (de Vries et al. 2003), still remains. Including a second absorption line in the fit yields an energy that is consistent with the $1s - 2p$ transition of compound oxygen (Figure 5.2, right panel). The measured EW is $1.40^{+0.26}_{-0.28}$, consistent with the findings of Takei et al. (2003).

However, large uncertainties still remain on the laboratory measurements of oxy-

gen bounded with other elements and the identification of such features is not conclusive. Other laboratory measurements (*e.g.*, McLaughlin & Kirby, 1998; Gorczyca & McLaughlin, 2000) of atomic oxygen around its K edge region would interpret the complex features around the edge as absorption lines from neutral and ionized oxygen; we will call this model 1 (Figure 5.2, left panel). The only two features in common with the Takei et al. interpretation are: the absorption edge at 0.543 keV (22.83Å) and the $1s - 2p$ transition line at 0.524 keV (23.5Å). The region in between is fit by an absorption line at 22.89Å, consistent with the 1s-3p transition of neutral atomic oxygen, with an absorption line which would be consistent with a blend of unresolved lines of OIII (at 23.05 Å). Finally, the evident absorption line at 23.35Å, found also by Takei et al. is on the contrary interpreted not as oxygen in compound, but as ionized atomic oxygen (OII), as predicted by Gorczyca & McLaughlin (2000) measurements. This interpretation (model 1) is supported by *Chandra* -HETG results on a sample of bright galactic sources (Schulz et al., 2003; Juett et al., 2003). In Table 5.4 the results of the two models are shown. There is not a significative difference in terms of goodness of fit. However, given the more solid theoretical calculations and the previous analysis by *Chandra* -HETG, whose energy resolution, around the O edge, is almost a factor of 2 better than *Chandra* -LETG, the "ionized oxygen" interpretation will be preferred also in the following. Such ionized component would be interpreted as ionization of the ISM, localized in the vicinity of the source.
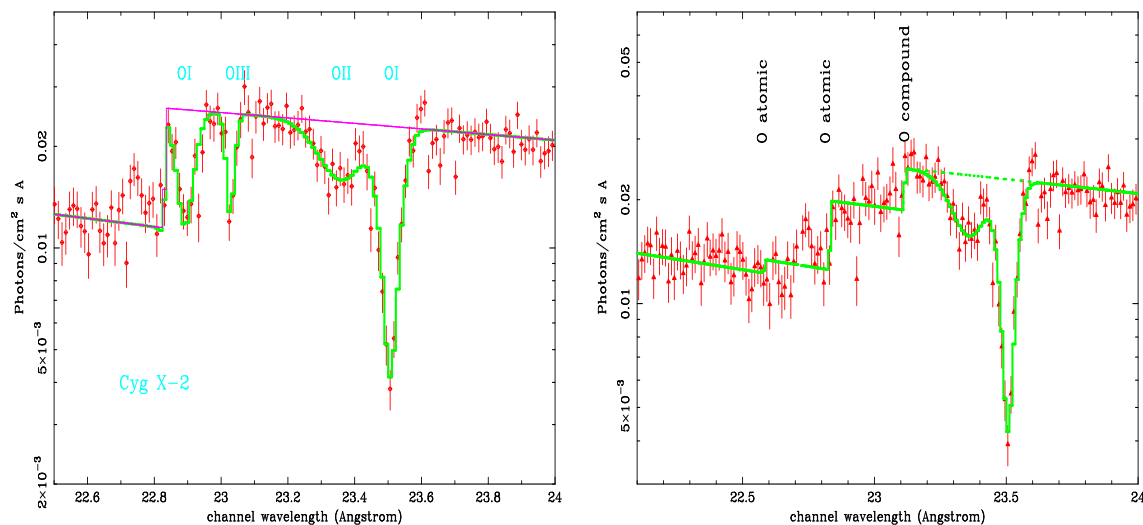

Figure 5.2: Comparison between model 1 (left) and model 2 (right). Model 1 includes one absorption edge and four absorption lines. Model 2 includes three absorption edges and two absorption lines. The plots show the data and the model divided by the effective area. According to de Vries et al. (2003), the emission residuals that still remains around ~22.7Å, maybe instrumental.

Table 5.4: *Fitting results for the oxygen region in Cyg X-2. The parameters for the continuum emission are taken from the broad-band spectrum. The energies are measured in keV and the Equivalent Width (EW) in eV. Model 1 interprets the spectrum in terms of absorption by atomic O, either neutral or mildly ionized. Model 2 fits the O vicinity with 3 edges (two of which from atomic O) and 2 absorption lines (one from atomic neutral O and the other from molecular O). See text for the physical interpretation.*

	model 1	model 2
Lines		
$Energy_1$	0.527±0.001	0.527±0.001
EW_1	1.49±0.17	1.45±0.19
$Energy_2$	0.530±0.001	0.530±0.001
EW_2	1.44±0.28	1.41±0.26
$Energy_3$	0.538±0.001	$\cdots$
EW_3	$0.44^{+0.19}_{-0.24}$	$\cdots$
$Energy_4$	0.541±0.001	$\cdots$
EW_4	$1.01^{+0.15}_{-0.26}$	$\cdots$
Edges		
$Energy_1$	$\cdots$	0.536 fix.
τ_1	$\cdots$	0.27±0.06
$Energy_2$	0.543±0.001	0.543 fix.
τ_2	0.81±0.02	0.45±0.02
$Energy_3$	$\cdots$	0.549 fix.
τ_3	$\cdots$	$0.09^{+0.07}_{-0.08}$

5.3.3 The halo spectrum

The pure halo spectrum was extracted as described in §4.3.4. In Figure 5.3 the spectra, not yet PSF subtracted, are plotted for radii ranging from 2.1′ to 4′, in order to illustrate the behavior of the halo with increasing angular distance from the source, as the PSF contribution becomes less important. Below 2 keV, the decline of the curve is evident as well as the presence of three absorption features corresponding to the energy of O (0.53 keV), Mg (1.33 keV) and Si (1.87 keV). The vertical blue lines indicate the position of such features and for completeness, the Fe L edge position (0.709 keV). The red lines around 2 keV mark the mirror scattering features of gold. After the PSF subtraction, the halo spectra, within the statistical error, do not vary dramatically as a function of the observer's angle, implying that the medium, on average, is evenly distributed. This is also confirmed by the spatial analysis of the halo (Figure 5.5). However, above 2 keV the differential scattering cross section does change dramatically as a function of the solid angle (Figure 2.5), but, given that at around this energy the contribution of the PSF wings is dominant, this effect is unobservable in the present data.

54

5.3.4 Spectral modeling of the Halo

Using eq. 2.15 I calculated the expected scattered intensity for the most common constituents of interstellar grains at a given observed angle, i.e., graphite (carbon) and silicates. Silicates are found in the form of $Mg_{2x}Fe_{2(1-x)}SiO_4$, thus I included this material in the fit in the three different forms of MgFeSiO4 ($\rho = 3.8 \ g \ cm^{-3}$), Fe_2SiO_4 ($\rho = 4.39 \ g \ cm^{-3}$), and Mg_2SiO_4 ($\rho = 3.27 \ g \ cm^{-3}$). In the energy range 0.4-2 keV, where the halo is relevant, I considered a range of grain sizes from 50Å to $0.4\mu m$ distributed according to both the MRN and the WD01 model (Chapter 2). The relative contributions from the different grains materials are free parameters. The goodness of the fit was then evaluated minimizing the χ^2 (§4.3.5).

Since these data are cut in energy below 0.4 keV, they cannot constrain the carbon component, whose main feature is at 0.28 keV. Indeed, the data are modeled by a mixture of Mg_2SiO_4 and $FeMgSiO_4$ and pyroxenes ($MSiO_3$, where M is either Mg or Fe) (χ^2/dof=1.01,1.03 for MRN and WD01 respectively). C, O, Fe, Mg and Si account alone for 95% of the dust components (Whittet, 2003). All elements but O account for 15-30% of the total amount of dust, locked in various forms. According to the best-fit model (which includes only silicates and carbonaceous grains) 40% is due to O, 26% to C, 10 and 12% to Si and Mg and 4-5% to Fe. Better statistics would be needed to put tighter constraints.

In Fig 5.4, I show the scattered radiation data collected in a ring around 4'. Superimposed are the best-fit models using MRN and WD01 (solid line and dashed-dotted line). Since the continuum in the scattered spectrum has to be a superposition of many components, that the present spectral resolution cannot disentangle, I cannot rule out the presence of other compounds in the diffuse interstellar dust toward Cyg X-2 . Nevertheless, the data show a major contribution from silicates of the form of pyroxenes and olivines.

Magnesium and silicon are only marginally detected in absorption (Fig. 5.1). Indeed the ISM extinction cross section is due predominantly to gas phase below ~1 keV and to solid particles above (see Figure 6.10). While gas can only absorb, solid particles both absorb and scatter, therefore the scattered spectrum analyzed here reveals the pure dust components of the ISM. The prominence of the scattering features might suggest a substantial contribution to the scattering from refractory elements (like olivines and pyroxenes). Indeed, these compounds do not absorb the radiation as much as they are able to scatter it.

5.3.5 The halo profile

Information on the SBP of the source is fully described in §4.3.4. In Figure 5.5 the halo is compared with the PSF. The halo is smoothly distributed as a function of the angular distance from the source, thus I assume that the dust is uniformly distributed

along this line of sight. Both the MRN and WD01 grain size distributions fit the data well, in agreement with the halo spectral fitting. The fit was performed using the Rayleigh-Gans approximation, instead of the full Mie theory, for the differential scattering cross section. The two approaches tend to overlap above ~1 keV and once the energy is fixed the difference between the two is a matter of absolute normalization, which is let as free parameter here. Within the errors, the model shows a contribution of the extended emission of I_{frac}=3.2% at 1 keV, in rough agreement with the ROSAT results (PS95). This value corresponds to $\tau_{sca}(1 \text{ keV})$=0.02.
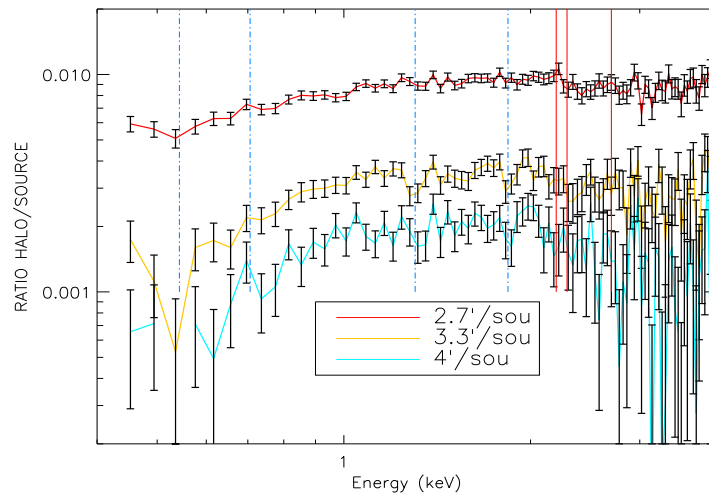
Figure 5.3: The spectra, still convolved with the PSF of the halo emission of Cyg X-2 for radii 2.7,3.3,4 arcmin respectively. At larger radii the PSF contribution becomes less important. Blue dashed vertical lines: energies of relevant ID elements (O, Fe, Mg, Si). Red solid vertical lines: gold features.
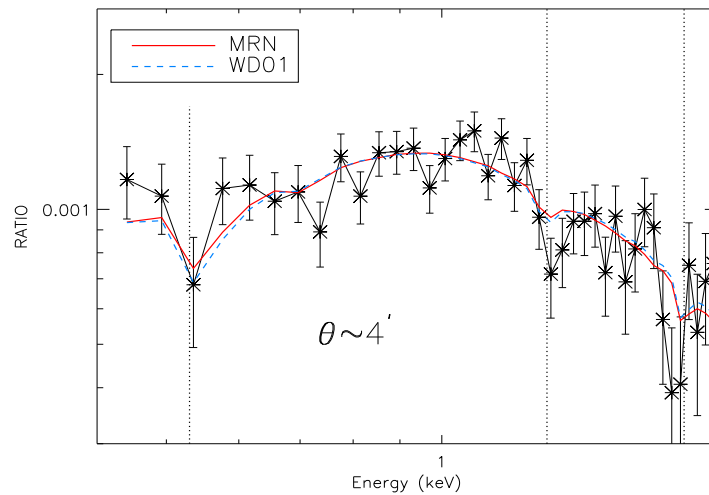
Figure 5.4: Epic-pn data of Cyg X-2 halo (asterisks) compared with the best-fit models: WD01 (blue dashed line) includes 27% of $FeMgSiO_4$ and 73% of Mg_2SiO_4 and MRN model (red solid line).
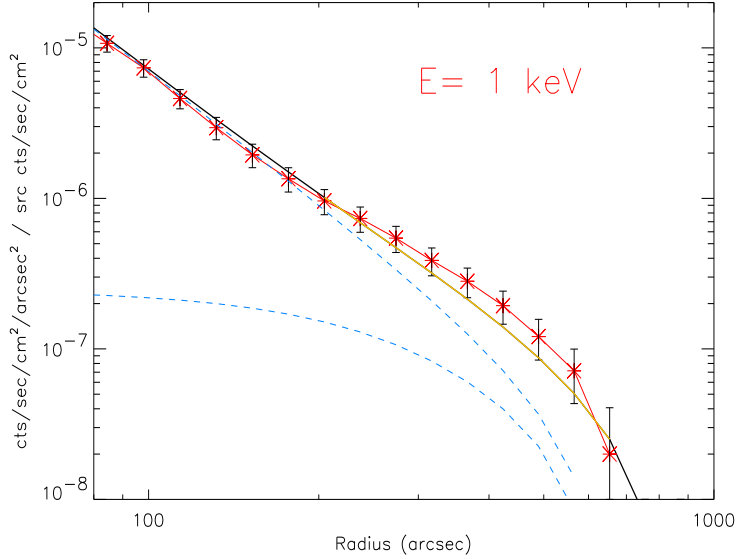
Figure 5.5: The halo profile (asteriscs) compared to the PSF around 1 keV. The dashed blue lines are the halo model component and the PSF, while the yellow line indicates the best-fit (PSF+model) to the total data.

5.4   GX 339-4

5.4.1   Broad-band spectrum

This black hole candidate was discovered in 1973 by the *OSO-7* satellite, and since then it has been extensively studied in the Radio, IR, Optical and X-ray bands. Its flux behavior is characterized by three main states. The source is found most of the time in the low state, when the spectrum is dominated by a power law of the form $F(E) \propto E^{\Gamma}$ with photon index =1.5-2 (Maejima et al., 1984). In the intermediate and high states the flux increases as does the soft component of the spectrum, (Mendez & van der Klis, 1997; Belloni et al., 1999) modeled with a black body-like component. Such thermal emission is supposed to arise from the accretion disk around the compact object. The hard energy tail is modeled in this case with a steeper power law. The non thermal component, visible at medium energies, is believed to arise from the reprocessing of the disk photon via Inverse Compton effect.

   In the observation discussed here, the source was found in a high state. The broadband spectrum, measured by EPIC-pn, is dominated by a soft component which is best modeled by a multicolor black body (see §5.3) with an associated N_H in the interval $5\text{-}5.8 \times 10^{21} cm^{-2}$. Previous spectral analysis of this source during the high state made

it possible to constrain the hard tail parameters thanks to the broader bandpass of *Ginga* (2-20 keV, Miyamoto et al., 1991). Their analysis preferred a comptonized black body (a thermal component), which provides a curvature in the spectrum over a straight power law (non thermal component). The present data seem to confirm this result since a power law worsens the χ^2, but given the low signal to noise, I cannot put tight model constraints on the spectral shape above ~7 keV. The evidence of an iron line, which would show the presence of accreting matter around the source, is weak in ASCA observations (Wilms et al., 1999), taken during a low flux state. However, in a very high state an iron line of equivalent width ~70-100 eV is required as well as an edge feature consistent with absorption by highly ionized iron at ~ 8.8 keV (Miyamoto et al., 1991). In the modeling of the present data, the addition of a Gaussian at 6.4 keV does not improve the χ^2, but above ~7 keV, EPIC-pn effective area and the poor statistics do not permit a detailed description of the data.

5.4.2 RGS spectrum

GX 339-4 is significantly more absorbed than Cyg X-2 and its flux is at least a factor of four fainter. This hampered the possibility o a detailed description of the spectrum at the lowest energies. On the other hand, absorption from heavier elements (Fe, Ne, Mg, Si) becomes more important ($N_j \propto N_H$, for an element j). The RGS bandpass is nominally 0.35-2.5 keV, but calibration problems still exists above ~1.8 keV (Pollock, 2003), therefore the present analysis is limited to 0.35-1.8 keV. The edge features of oxygen (K-shell), Fe (L_3-shell), Ne (K-shell) and Mg (K-shell) could be clearly detected. From their optical depths, I derived the element abundances, as described in §5.3.2. Table 5.5 lists the resulting N_H values. As far as the oxygen edge is concerned, an underabundance of ~30% is found, while Mg, measured for only GX 339-4, is significantly overabundant (up to a factor of 3), however the value is not precisely determined.

Detailed studies of K and L shell photoabsorption cross sections have recently become available for oxygen, iron and neon (McLaughlin & Kirby, 1998; Kortright & Kim, 2000; Gorczyca & McLaughlin, 2000). As discussed in §5.3.2, they are needed to understand the observed X-ray spectra presented here. In GX 339-4 I could identify complex structures around the O K edge and the Fe L edge that I interpreted as the resonant features of those elements in atomic form (Table 5.6).

The vicinity of the oxygen edge in this source spectrum is characterized by lower statistics with respect to Cyg X-2 which is less absorbed than GX 339-4 . In addition, there is an effective lack of data due to a chip gap occurring between 22.7 and 23 Å. Only the two prominent features of OI could be detected that may contain a contribution from other predicted features. The feature at ~0.707 keV near the L_3 iron

Table 5.5: *Estimated ISM abundances along the line of sight of GX 339-4. From the optical depth (τ) of the edge, the total N_H is calculated, assuming solar abundances (Wilms et al., 2000).*

Element	Energy (keV)	τ	$N_H(10^{21})$
O K-shell	0.5431 ± 0.0009	1.8 ± 0.11	$3.7^{+0.2}_{-0.4}$
Fe L-shell	0.7078 ± 0.0003	$0.34^{+0.04}_{-0.1}$	$6.3^{-1.8}_{+0.8}$
Ne K-shell	0.870 ± 0.001	0.20 ± 0.04	4.4 ± 0.8
Mg K-shell	1.303 ± 0.001	0.12 ± 0.03	12^{+5}_{-3}

Table 5.6: *ISM Absorption line parameters.*

Transition	Energy (keV)	Wavelength (Å)	EW (eV)	EW (Å)
OI 1s-2p	0.527 fix.	23.51	16^{+4}_{-6}	$0.69^{+0.15}_{-0.27}$
OII 1s-2p[1]	0.530	23.35	...	...
OIII 1s-2p[1]	0.538	23.05	...	...
OI 1s-3p	0.541 fix.	22.89	2.8 ± 1.8	0.120.08
Fe 2s-2p	0.707 fix.	17.53	2.0 ± 0.8	0.05 ± 0.02

[1] not resolved in GX 339-4.

edge is detected (Figure 5.6) with high significance (5σ) and could be clearly identified with the Fe 2s-2p (spin 3/2) transition (Kortright & Kim, 2000). The resolution is insufficient to recognize both the L_2 edge and the associated absorption line 2s-2p (spin 1/2) transition at $\sim$0.720 keV.

An ionized absorber?

In a *Chandra* -HETG observation performed at the end of a high flux state of GX 339-4 was 10 times dimmer than the present observation and showed a spectrum more typical of the "low flux" state (§5.4.1). In particular, a more prominent power law and an evident relativistic iron line was detected (Miller et al., 2003) and besides, the evidence of a local ionized absorption was claimed. In the wavelength range 9-19 Å several absorption features, especially from He-like oxygen and neon, were detected with calculated equivalent widths of the order of 10mÅ. This corresponds to a mild ionization of the absorbing medium, parameterized by the ionization parameter $\xi = L/nr^2 \sim 70$ where L is the luminosity of the source, n the number density of the medium and r the distance from the photoionizing source. In the present data, none of the absorption lines were detected. Despite the lower resolution of RGS (RGS 2 order has 47% less resolving power than *Chandra* HETG), with an intensity 10 times
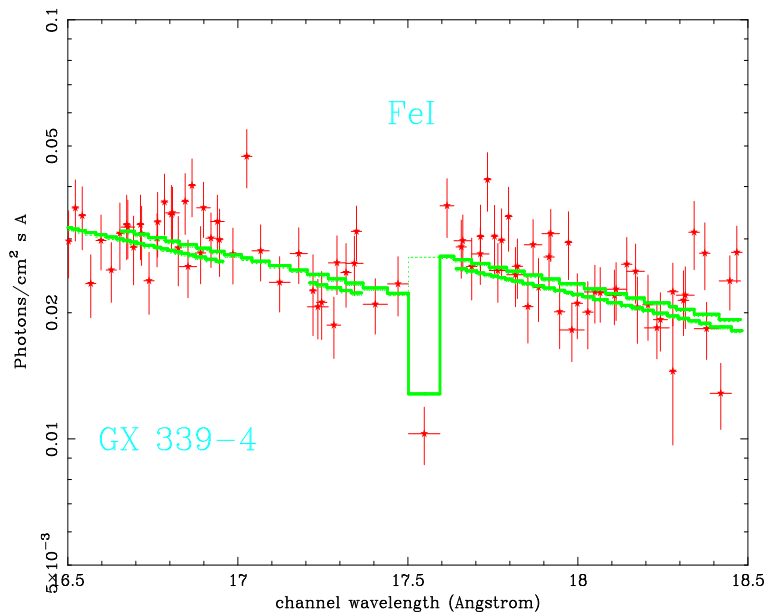
Figure 5.6: Detail of the Fe edge at 0.708 keV for GX 339-4 . The line detected at 0.707 keV has been identified as FeI 2s-2p bound-bound transition.

larger than in the *Chandra* observations, such features should have been detected. Their absence actually reveals a different local physical conditions. Indeed, considering the higher luminosity of GX 339-4 in the RGS observation, ξ would be >700 and simulations show that the elements of a possible absorbing medium, believed to be at a distance of $\sim 2 \times 10^{11}$cm from the source (Miller et al., 2003), would be totally stripped of their electrons and no longer visible in the soft energy range. This evidence supports also the hypothesis of a warm absorber intrinsic to the source, rather than absorption occuring in the ISM.

5.4.3   Halo imaging and spectroscopy

The EPIC-pn information on GX 339-4 was very fragmentary in the present data due to technical problems during the observation. The imaging information was lost up to $\sim 100''$ from the center, because of the misplacement of the "mask" which was supposed to cover the core of the source (masked mode). The DLI file (Appendix A), was also lost during the observation. For only ~ 0.1 ksec of the integration time were the four quadrants of the detector switched on at the same time.

In Figure 5.8 the spectrum collected at around 4.5′ is plotted. The PSF wings contribution to the observed spectrum is subtracted. This is achieved comparing the halo spectrum taken at a certain distance from the source with Mkn 421 spectrum taken at same distance (Figure 4.4). Since the absolute flux of GX 339-4 cannot be recovered precisely from these data, the scaling relies on Mkn421 absolute normalization, letting
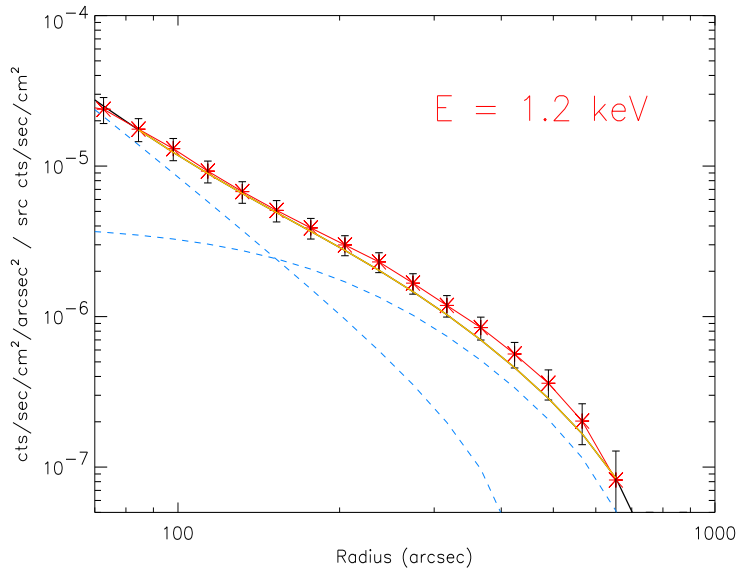
Figure 5.7: Halo profile for GX 339-4 around 1.2 keV. The star points are the data, the solid thick yellow line the model folded with the PSF. The dashed thin blue lines indicates the PSF and the halo component separately.

the spectra to overlap at higher energies, where both GX 339-4 and Mkn421 spectral shape is dominated by the mirror scattering (see *e.g.*, Figure 6.3). The overall level of the ratio in Figure 5.7 is affected by an uncertainty of 30%. However this does not affect the spectral shape, which could be modeled. Unfortunately, the statistics do not allow any quantitative measure on the chemistry of the dust. In order to fit the continuum, silicates of Mg are needed plus a contribution of free Fe. The amount of O is very loosely constrained, because of the relatively high N_H towards this source, thus the data cannot distinguish whether the O can be explained by Mg_2SiO_4 alone or at least a part of the iron has to be bound in silicates of the kind of olivines. In Figure 5.8 the best-fit result is shown. The imaging analysis shows an amount of dust which is consistent with previous results by ROSAT (PS95). At 1.2 keV the fractional contribution to the total emission is 10%. The MRN model properly fits the extended emission (Figure 5.7).

5.5   Discussion: absorption features and abundances

From the high-resolution RGS spectra I could clearly detect the ISM absorption edges and also study their spectral vicinity. The low absorption source Cyg X-2 showed a very complex oxygen region where different ionization states of atomic oxygen could be identified: OI (1s-2p, 1s-3p transitions) , OII (1s-2p) and OIII (1s-2p). For GX 339-4,
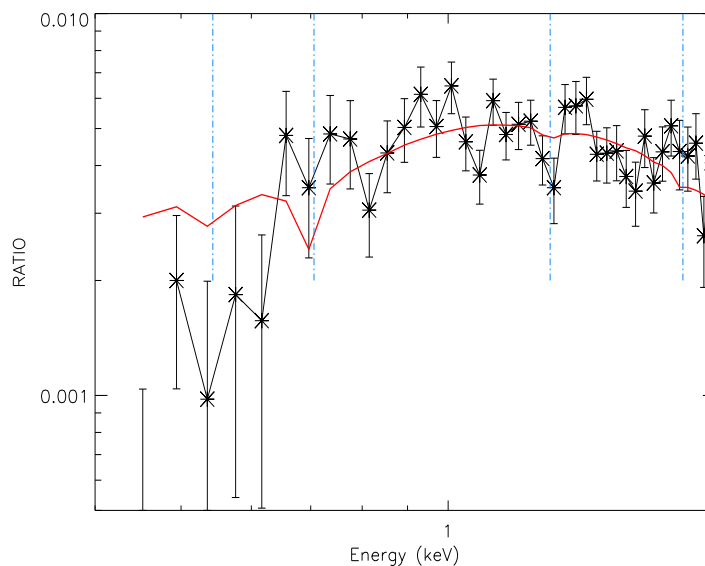
Figure 5.8: Halo spectrum at 4.5′. The model uses the MRN grain size distribution and the Mie theory. The fit suggests the presence of iron and magnesium, which is difficult to quantify due to the lack of statistics. The dashed vertical lines indicate the position of O, Fe, Mg and Si, from left to right.

in addition to the oxygen features, albeit detected with lower significance, the Fe L edge region showed evidence of the 2s-2p (spin 3/2) atomic iron absorption line.

Although the measurement for OII and OIII are supported by laboratory measurements, one cannot rule out completely that the absorption feature at 23.35Å is not due to molecular oxygen (Paerels et al., 2001). Moreover, additional molecular oxygen may be present, but it may well not be detected. In this case, the ratio of molecular to neutral oxygen would be ∼10% (Juett et al., 2003) assuming that the oscillator strength of molecular oxygen (which is unknown) is similar to that of OII. Alternatively, Juett et al. (2003), performing a study on the curve of growth of the high resolution absorption lines observed in Cyg X-2 by *Chandra*-HETG, determined that the ratio of ionized to neutral oxygen must also be 10%. The XMM data hint at an underabundance of O, derived from the N_O of the absorption edges. Oxygen in molecular form or in an ionized phase may account for the discrepancy.

Despite the maximal depletion fraction of ∼60%, the abundance of oxygen is so high in the ISM that a relatively large fraction dust must contain it. There is no general consensus on the exact amount of O, since this value strongly depends on the solar abundances assumed. The most recent results (Allende Prieto et al., 2001; Holweger, 2001) give an O/H ratio ranging from 490 to 545 ppm for the solar environment, which

tends to agree with other observational evidences for the O gas-to-dust-phase ratio in the ISM. As far as O in dust is concerned, it is known that the maximum amount of O that can be locked up in silicates is 180 ppm (Cardelli et al., 1996). The average value on a sample of 19 stars found by André et al. (2003) is 109 ppm. The corresponding amount of O in dust would be approximately 21%.

For the XMM data I could compare the effect of the scattering, which is due to dust grains only, with the absorption, parameterized by the equivalent hydrogen column density, which is due to both gas and dust. The Cyg X-2 scattered spectrum (§5.3.3) is better sampled than GX 339-4 at the O energy. The best-fit for Cyg X-2 data requires a mixture of pyroxenes and olivines such that the ratio Mg/Fe is 5/1.6, which has to be compared with the theoretical 5/2. Mg and Si belong to the same depletion group, and silicates with such an Mg/Fe ratio can account for all the depleted Mg and Si. Oxygen may be found in other forms (metal oxides for instance) and for only about one third is supposed to be in silicates. However, the results of this investigation are consistent with almost all the oxygen being in form of silicates (Figure 5.4). These conclusions must be confirmed by deeper observations of Cyg X-2 and other halo-sources with similar characteristics.

A clear correlation between the observed N_H and the halo contribution to the total emission at 1 keV (parameterized by the scattering optical depth τ_{sca}) was established by PS95. Nevertheless, close to energies where the dust elements absorb/scatter, this relation may not be true. In particular the refractory elements (such as the olivines and pyroxenes) have much more scattering than absorption power. This would explain the lack of significative absorption by Mg and Si in Cyg X-2 spectrum (Figure 5.1) compared to the significative features in the scattered spectrum.

Chapter 6

The Chandra view of interstellar dust

6.1 Motivations

The *Chandra* Observatory characteristics are in many ways complementary to those of XMM-Newton. As seen in Chapter 3, the PSF of *Chandra* -ACIS (FWHM $\sim 0.5''$) enable halo studies down to small angular distances from the source, where larger grains or matter closer to the source are believed to play a role. On the other hand the *Chandra* field of view (17′ ACIS-I), as well as the effective area (600 cm^2 at 1 keV) are smaller than those of XMM-Newton. Thus brighter halos, implying high column densities with bright X-ray emitters behind, can be best studied by *Chandra*. However, sometimes these observational parameters (high luminosity of the source and high column density) cancel the benefit of having a narrow PSF, because of the effects of pile-up that may distort the surface brightness profile as far as a radius of 60-100″. Studying highly absorbed sources has also the disadvantage of overshadowing the very soft X-ray spectrum of the source and therefore of the halo, where all the interesting scattering features are located.

For the study of *absorption* by ID, the high resolution spectroscopy of *Chandra* -HETG is ideal. HETG is at present the grating device with the best energy resolution in the energy range 0.3-1 keV, and is able to unveil signature of ID in the *absorbed* spectrum of an X-ray source. Indeed, as seen in Chapter 2, modulations in the usual absorption edge should be detected, if the X-ray radiation is absorbed by solid particles. These X-ray Absorption Fine Structure (XAFS, §2.3) are well studied in solid state physics, but were detected in astrophysaics only recently, with *Chandra* -HETG observations (Lee et al., 2002, this work).

In this chapter I describe first an imaging study of halos, carried out on a sample of archival sources observed by ACIS-S and ACIS-I. In the second part I present the analysis of HETG data and the discussion on the XAFS features.

Table 6.1: The Chandra ACIS Sample.

Name	Type[2]	l^{II}	b^{II}	RA	DEC	Instrument	Exposure[3]
GX 5-1	LMXB	5.1	-1.0	18 01 08	-25 04 31	ACIS-S	7
CEN X-3	HMXB	92.09	+0.34	11 21 15.2	-60 37 24	ACIS-I	3.9
						HETG[1]	50
						HETG[1]	40
1E 1740.7-2942.7-2942	LMXB	359.15	-0.12	17 44 02.7	-29 43 25	HETG[1]	70
						ACIS-S	10
TERZAN 5	GC	3.84	+1.69	17 48 05	-24 46.8	ACIS-I	42.1
V382 Vel	nova	284.17	+5.77	0 44 48.39	-52 25 30	ACIS-I	17.9
LMC X-1	HMXB	-79.8	-31.5	05 39 24	-69 45 15	HETG[1]	18.9
LMC X-3	LMXB	-86.4	-32.1	05 38 56	-64 05 47	HETG[1]	14.3

[1] zeroth order extraction.

[2] LMXB: Low Mass X-ray Binary; HMXB: High Mass X-ray Binary; GC: Globular Cluster.

[3] given in ksec.

6.2 The halo sources sample

The brightest halos occur for sources with high ($\sim 10^{22} \mathrm{cm}^{-2}$) column densities, therefore in order to have a halo contribution $> 10\%$, sources with galactic latitude $b < 3°$ were selected from the *Chandra* public archive (PS95). Table 6.1 lists the sources of the sample. Three of them (GX 5-1, LMC X-1, LMC X-3) were also included in the sample of 25 halo-sources observed by ROSAT (PS95).

The statistics of almost all sources in this sample was not sufficient for an energy-dependent analysis of the halo. I thus chose a *mean* energy, obtained by weighting the individual photon energies according to the energy dependence of the scattering cross section (E^{-2}, at least for E larger than ~ 1 keV). For the softer halos the energy was simply chosen at the maximum of the source emission, providing the maximum statistics. The halos were studied at one energy for all sources unless otherwise stated. In the following I present the general results on the halo sources, devoting additional discussion to the most interesting sources of the sample.

6.3 Results

Figure 6.2 displays the scattering halo profiles of this sample at one chosen energy. The profiles were modeled using a standard MRN grain size distribution and a uniform distribution of grains along the line of sight, although the upper and lower limits on the relative distance where the scattering takes place were free to vary in the fit. The goodness of fit was judged via the χ^2 minimization (Chapter 5). Once the pure halo

emission was modeled, the fractional contribution of the extended (I_{halo}) to the total intensity (I_{tot}) could be estimate. Recalling that:

$$I_{frac} = \frac{I_{halo}}{I_{tot}} = (1 - e^{-\tau_{sca}}),$$ (6.1)

and

$$\tau_{sca}(1\text{keV}) = \tau_{sca} \, E^2,$$ (6.2)

I could compare the scattering optical depths τ_{sca} of the halos, in the Rayleigh-Gans (R-G) approximation. The limits of the R-G approach will be extensively discussed in §6.3.4. The optical depths are listed in Table 6.2, along with the N_H measured from a broad-band spectral analysis, the fractional halo intensity measured at the chosen energy E_{mean} and the value of A_V, if known. In Figure 6.1 previous results by ROSAT (PS95) and the *Chandra* data points are plotted. For the three sources that were also present in the ROSAT sample (LMC X-1, LMC X-3, GX 5-1), there is agreement with the ROSAT findings. GX 5-1, and 1E 1740.7-2942 are known to be intrinsically absorbed and therefore they lie outside the correlation $\tau = 0.05 \times N_H(10^{21}\text{cm}^{-2}) - 0.083$ (PS95).

The globular cluster Terzan 5 also lies well outside the correlation. This may reflect intrinsic absorption of circumstellar material of the X-ray binary EXO 1745-248 which produces the halo (Heinke et al., 2003). On the other hand, the hypothesis of dust in the intracluster medium itself cannot be excluded. Recent results from the infrared camera on board the Infrared Space Observatory (Evans et al., 2003) revealed, for the first time, the presence of dust in the core of another globular cluster, NGC 7078.

Table 6.2: Results of the Halo Fit

source	N_H 10^{21}cm^{-2}	I_{frac} %	E_{mean} (keV)	A_V mag	$\tau_{1\text{keV}}$
GX 5-1	30.1 ± 0.4	25.5	1.75	. . .	0.8
CEN X-3	9.5 ± 0.5	22.8	1.75	4.4^2	0.76
1E 1740.7-2942.	82^{+35}_{-24}	5.2	1.75	$\sim100^5$	0.15
TERZAN 5	27 ± 2	14.0	1	6.75^1	0.15
V382 Vel	0.24 ± 0.02	3.2	0.75	$<0.31^4$	0.01
LMC X-1	7.3 ± 0.8	0.9	1	0.8^3	0.009
LMC X-3	2 ± 0.6	0.8	1	0.8^3	0.008

[1] Cohn et al. (2002), [2] Bradt & McClintock (1983), [4] Della Valle et al. (2002), [3] van Paradjis (1991) [5] $A_V = 25 - 175$, Skinner et al. (1991).
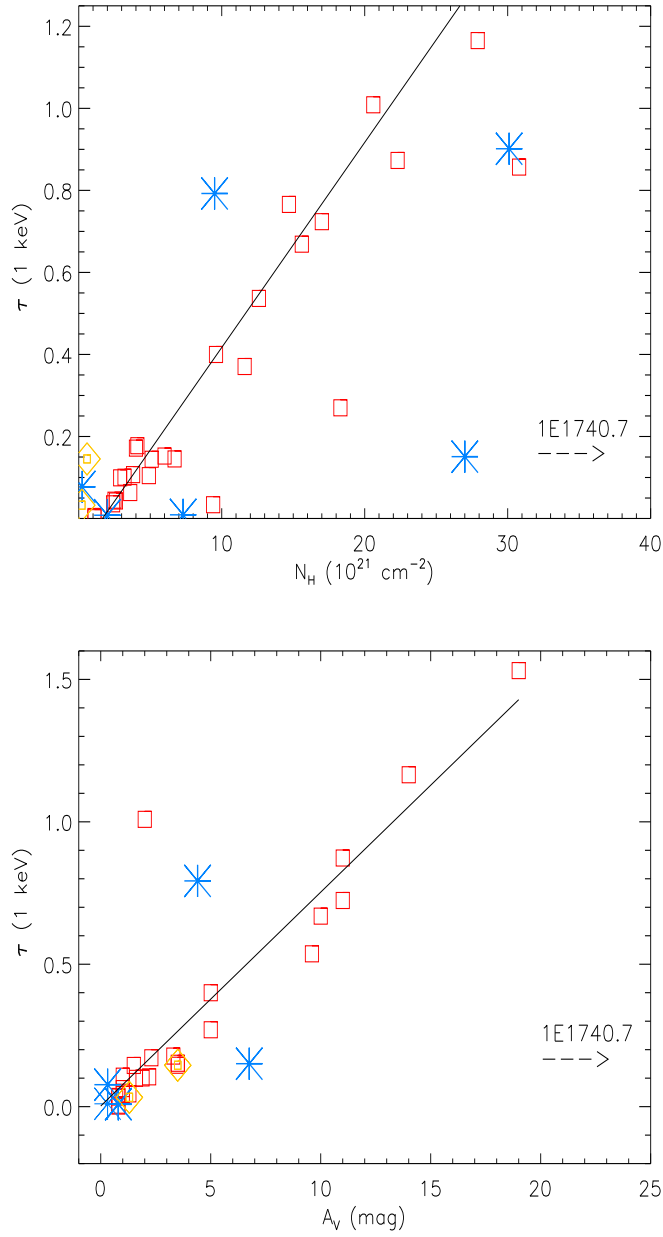
Figure 6.1: *Correlation between N_H vs τ (top) and A_V vs τ (bottom). The square data points represent the ROSAT data (PS95), while the asterisks are the Chandra data points from the present sample. The two yellow diamonds are XMM data for Cyg X-2 and GX 339-4. The source which lies well outside both the correlations is 1E 1740.7-2942.*
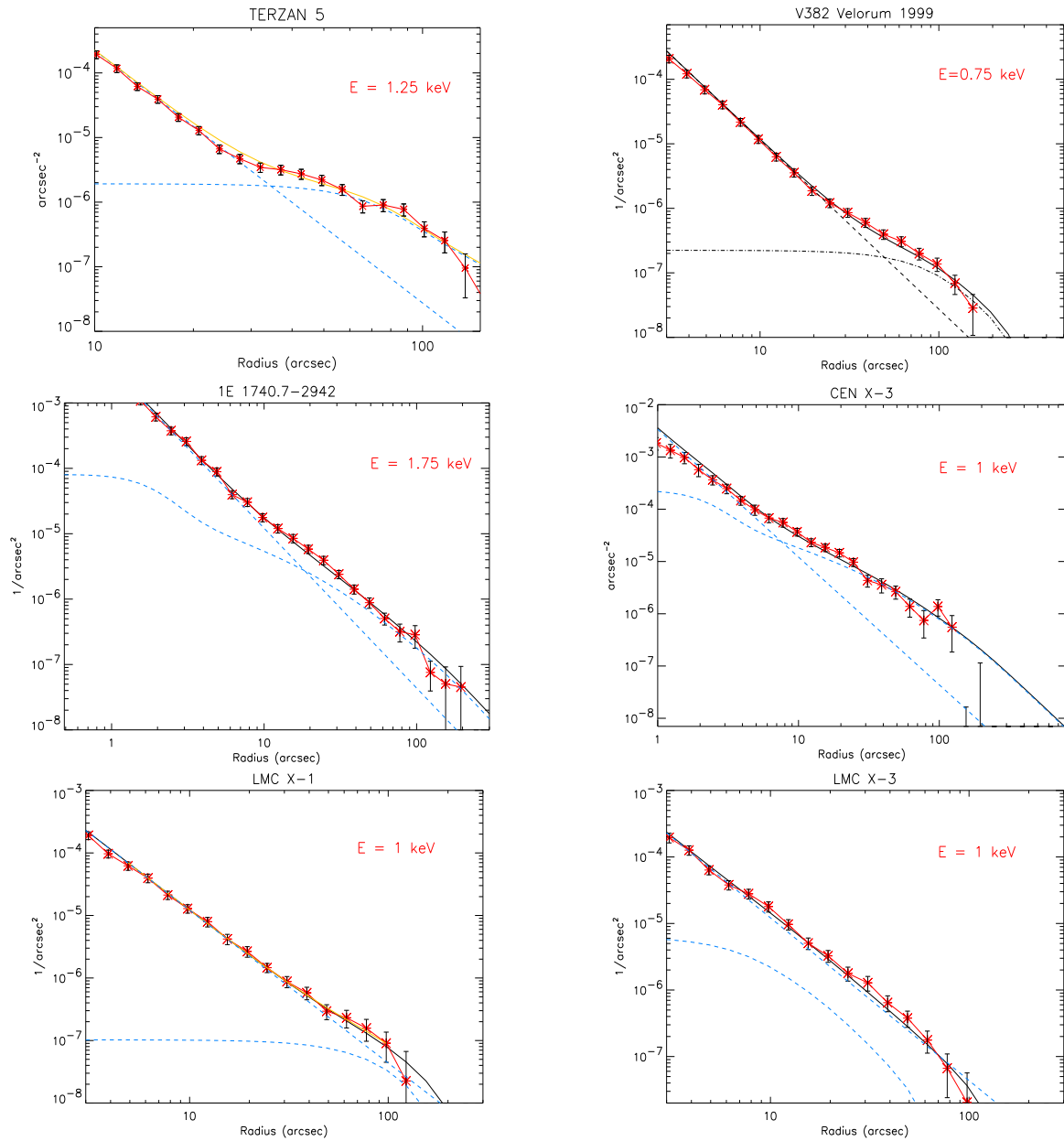
Figure 6.2: Halo fitting: data (star points) plus best-fit model+PSF (thick solid line) which is the sum of the halo model and the PSF (thin dashed lines).

6.3.1 GX 5-1

GX 5-1 was observed as a "guaranteed time" source. The object is located behind a dust layer with total column density $N_H \sim 2 \times 10^{22} \text{cm}^{-2}$. Its extreme brightness, permitted to perform an energy dependent study of the halo in the range 1-3.5 keV divided in 5 bins of 0.5 keV each. The *mean* energy is $\sim$1.7 keV (PS95). The halo could be studied only at radii larger than $100''$ from the source because of pile-up (see Figure 4.9).

This source provided also enough statistics to extract the spectrum of the scattered radiation in the ACIS energy range (0.5-8 keV), with the same procedure described in §4.3.2.

In Figure 6.4 (left panel), the SBP, the PSF and the best-fit model are shown. At all the selected energies the halo shape is quite uniform suggesting in this way a smooth distribution of the dust along the line of sight. For the dust size distribution, the two models described in Chapter 2 were applied. In this case, the energy range chosen for the analysis, given that lower energy photons are completely absorbed, allowed us to use the Rayleigh-Gans approximation. The validity of the models could not be fully constrained because the pile-up-free portion of the SBP was relatively small (*Radius* $>100''$). The fractional contribution of the halo is 25.5% at 1.75 keV. The large halo fraction in GX 5-1 can be appreciated also comparing the scattered spectrum (summed contribution of a dust halo and a mirror scattering halo) to the PSF one (Figure 6.3). The halo reaches its maximum around 1.7 keV, exceeding the PSF of a factor of ~ 20, at $100''$. The decline of the halo above 2 keV scales roughly as $E^{-2.4}$ (Figure 6.4, right panel).

In principle the spectral window between 1 and 2 keV would be eligible for detecting the scattering features (at least the on of Si at 1.84 keV), predicted by the theory and observed by XMM, as described in the previous chapter. Unfortunately, the correction for Charge Transfer Inefficiency (CTI) in the chip S3, where the source is located, is not calibrated at the time of writing. This leads to *(i)* a broadening and a shifting in energy of any spectral feature. This effect is emphasized going towards the read out node and *(ii)* impossibility to assign the CTI correction to the OOT events. Any attempt to search for sharp scattering features from the ratio of the halo and the source spectrum would be misleading.
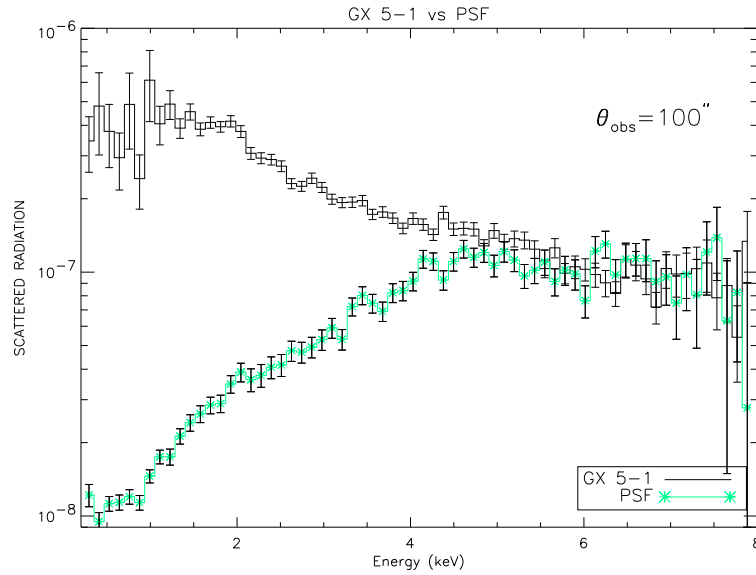
Figure 6.3: Comparison between GX 5-1 scattering halo spectrum and the PSF contribution at all energies at a distance of 100″ from the source
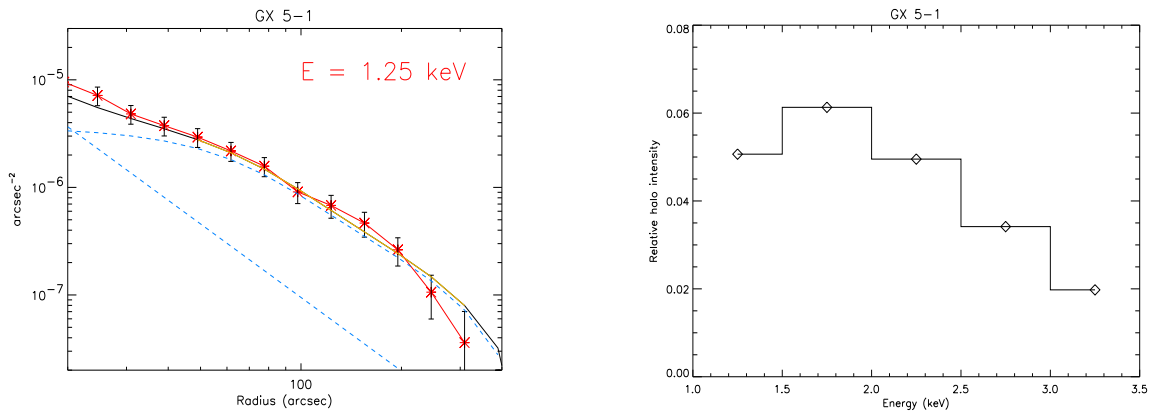

Figure 6.4: Left: GX 5-1 scattering halo at 1.75 keV along with the best-fit model+PSF (solid line), the PSF (dashed) and the halo model (dashed dotted). Right: the scattering halo intensity, PSF subtracted, as a function of energy. Of course the shape of Figure 6.3 is recovered, albeit at much lower resolution.

6.3.2 CEN X-3

This High Mass X-ray binary was observed on three occasions by *Chandra* in 2000, spanning 265 days between the first and the second and only 35 days between the second and the third. These observations measured different flux states, associated with a spectral variation (Figure 6.5), which could also be reflected in the halo properties.

As seen in Figure 6.5 (top left panel), the obs#1 monitored the eclipse of the neutron star behind the companion star, after a sharp increase in flux going from 5 to 20 cts/bin. In the right top panel the combined spectrum of all the intervals, taken from the 0th order is shown: the soft spectrum is obliterated up to 2 keV, while a strong iron complex around 6-7 keV is detected. The detailed modeling of the high resolution spectrum in function of time was presented by Wojdowski et al. (2003). The flux variation characterizes the hard part of the spectrum only, namely, the iron complex, while the soft spectrum stays constant and at a very low level trough all the phases. As predicted by the theory, even if the variation in flux is of a factor of four, we found the scattering halo not to be influenced since the scattering is dominant at lower energies. Indeed the extended emission does not change (the upper limit is $< 2\%$) its relative contribution to the total output in the energy range 0.5-2 keV.

Observations #2 and #3 were instead performed after roughly nine months. The appearance of the two spectra is similar, but shifted in flux of a factor ~ 30. Both light curves present smooth modulations of $\sim 20\%$ in amplitude. I extracted the scattering halo of Cen X-3 for obs#2 and obs#3 for the whole observation interval.

The analysis of the SBP revealed a bimodal structure for the halo profile. A first bump was detected at $\sim 13''$, while a more extended structure is visible at radius larger than $\sim 50''$. For obs#3, the halo could be detected just up to $25''$ because of the "small window" HETG observational mode (*i.e.*, a FOV of only $1.4'$).

A single component model, assuming a uniform distribution of dust along the line of sight plus a MRN model for the dust size distribution, did not provide a good fit. In particular, it was not able to explain the structure at small radii, even if the exponent of the MRN distribution (§2.9) was allowed to vary towards values lower than -3.5 thus letting the large grains to make a larger contribution (Figure 6.6). Allowing the upper limit on grain sizes to be larger than the classical value of $0.25\mu m$ did not improve the fit. Large grains are able to produce narrower halos, but, alternatively, also a "clumpy" distribution of dust produces halos with different extensions resulting in a "bumped" halo like that observed in Cen X-3. To test this model, I allowed a percentage of the dust to be clumped at variable distances on the line-of-sight to the object to determine a likely distribution. The best-fit is obtained when $\sim 20\%$ of the material is clumped at 80% of fractional distance.

Our line of sight indeed intercept regions of different dust density. In particular, Cen X-3 is located well inside ($b = 0.33°$) of Sagittarius-Carina arm at Galactic lon-

gitude $l = 292.09°$. The distance to Cen X-3 was estimated to be 6 kpc (Woo et al., 1994), 8 kpc (Krzeminski, 1974), and 10 kpc (van Oijen, 1989). In Figure 6.7 a map of the Milky Way, traced by HI emission, is shown (McClure-Griffiths et al., 2002; Heiles, 1984), as well as the possible locations of the object, in kpc. Depending on the choice for the distance, from the three estimates above, Figure 6.7 shows that the line of sight should meet a bulk of dust starting from a fractional distance of $\sim$60% if the object is closer to us, while if the location is around 10 kpc or more, the line of sight could even avoid the higher density regions until $\sim$80-90% of the path. The result presented here is therefore consistent with the higher distance estimates and implies a lower limit of $\approx$10 kpc.

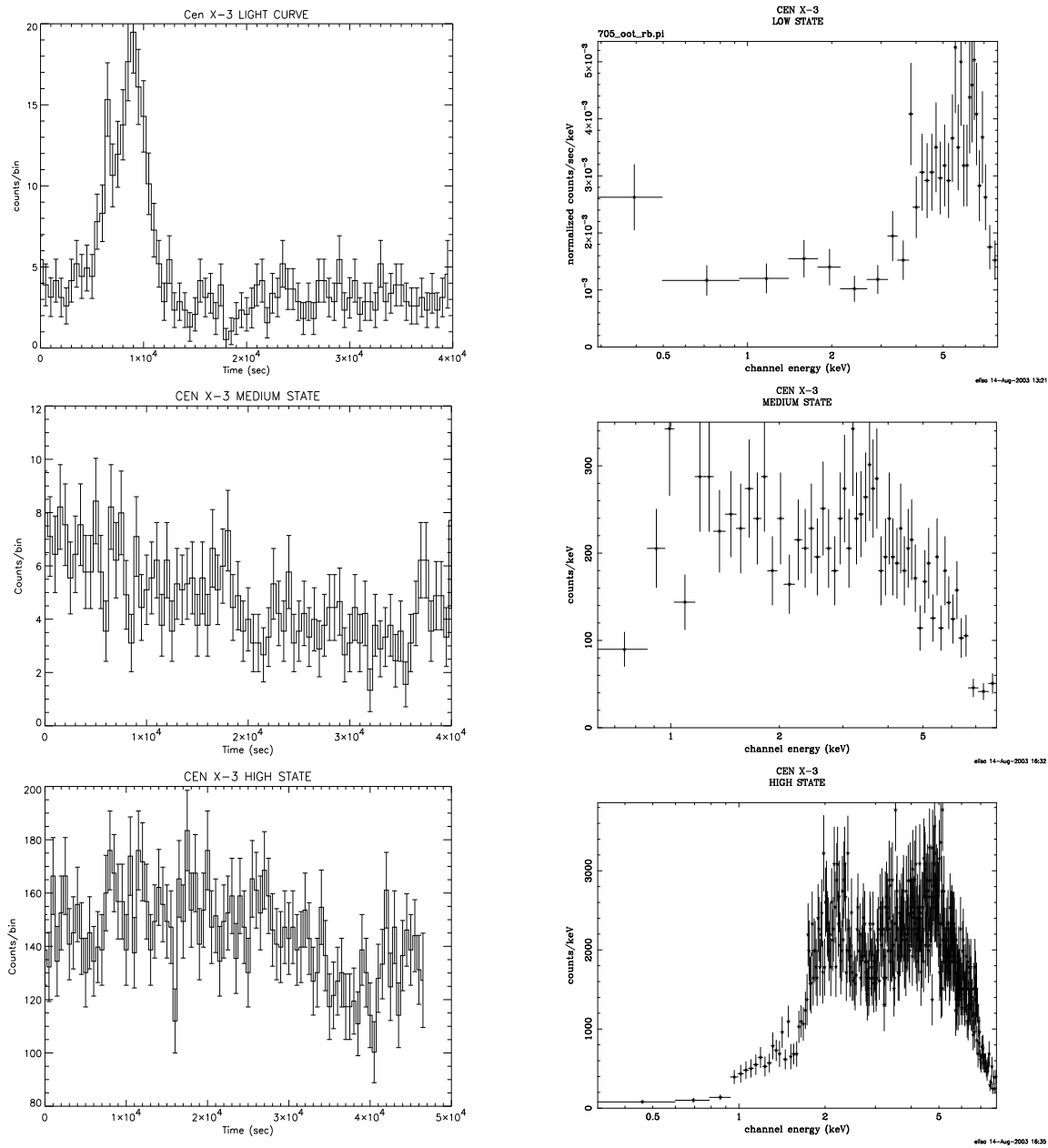*Figure 6.5: Light curves and spectra relative to three flux states of Cen X-3. The binning for the light curves is ∼500 seconds.*
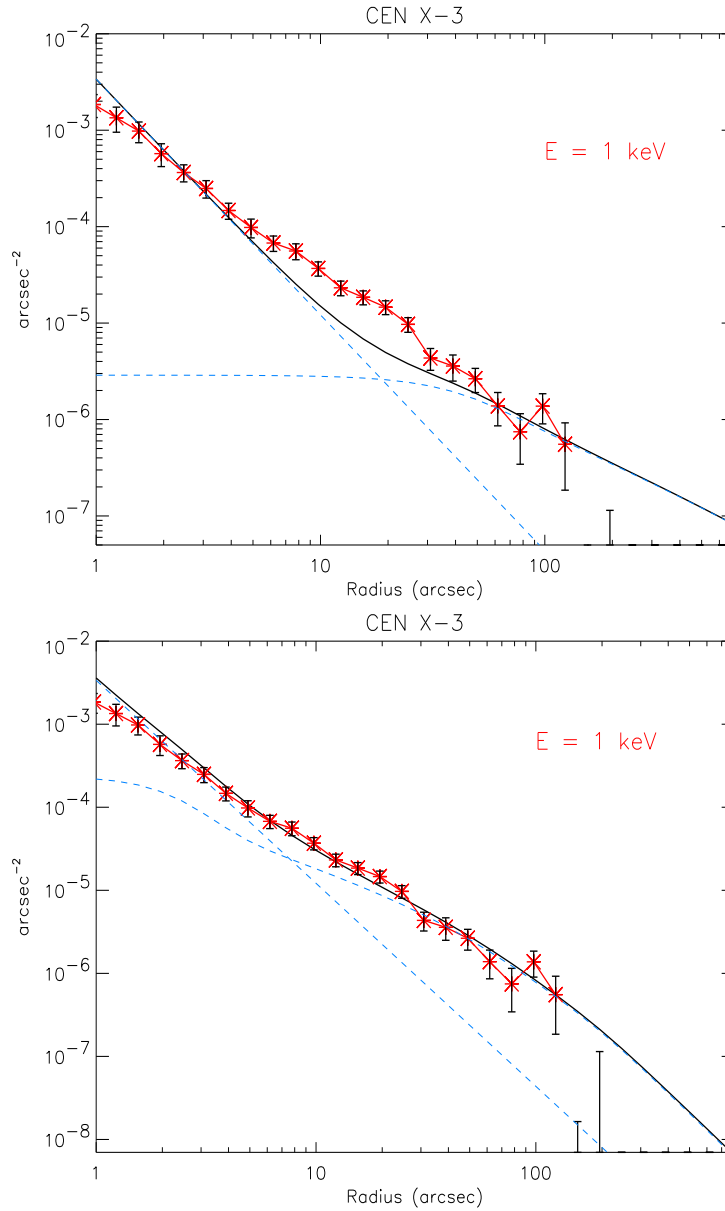
Figure 6.6: Halo fitting for Cen X-3: a single component model is not sufficient to explain the data (top). Concentrating the amount of dust to a fractional distance above 60%, in agreement with the known distribution of dust along the line of sight, greatly improves the fit (bottom). The star points are the data, the solid thick line is the model convolved with the PSF. The thin dashed lines are the separate component of PSF and model.
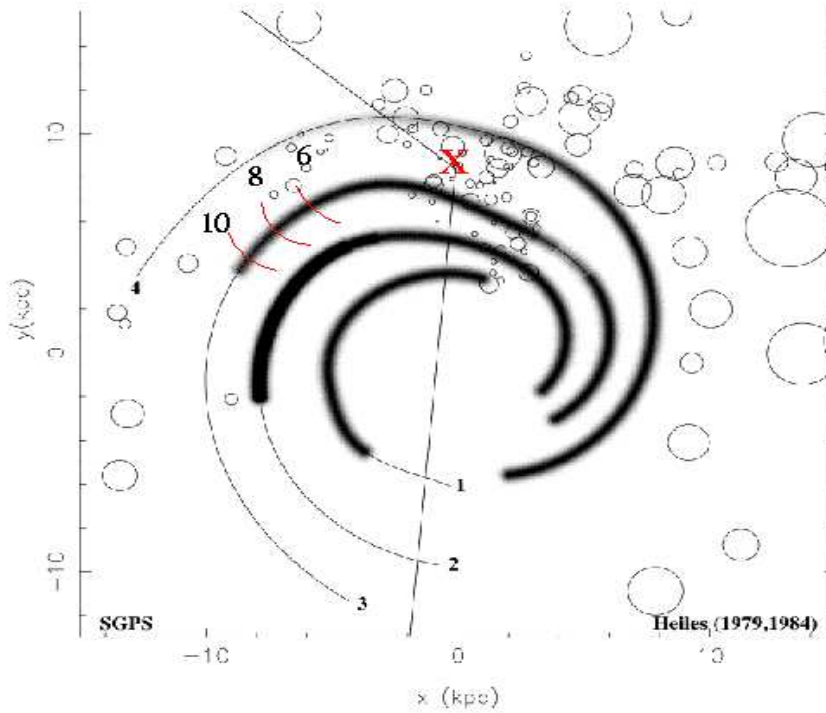
Figure 6.7: Distribution of the HI emission in the Milky Way (from McClure-Griffiths et al., 2002). The possible estimated distances of Cen X-3 are indicated: 6, 8, 10 kpc. (see text). The cross indicates the position of the Sun.

6.3.3 1E 1740.7-2942, the Great Annihilator

This black hole candidate is located only ~ 300 pc away from the Galactic center. The line of sight intercepts three spiral arms of the Galaxy's structure, and the column density of the diffuse medium, in a 1° region around the source, is 4.6-7.2×10^{22} cm^{-2} (Savage & Mathis, 1979). There is no conclusive agreement on the value of N_H towards the source itself, which would be crucial for understanding whether the source is located close, behind or embedded in the giant molecular cloud G−0.86−0.08 (Bally et al., 1987). Through radio observations of the HCO$^+$ (1-0) line, Phillips & Lazio (1995) and Yan & Dalgarno (1997) argued that the source must lie within the molecular cloud. The same conclusion was reached based upon the 6.4 keV iron line extinction ($< 2 \times 10^{22}$ cm^{-2}) detected by ASCA. This N_H value for the immediate surroundings of the source would be inconsistent with the total N_H ($\sim 1 \times 10^{23}$ cm^{-2}) measured by ASCA toward the source (Churazov et al., 1996). On the other hand, using the same ASCA dataset Sheth et al. (1996) measured a column density from photoelectric absorption ($\sim 8 \times 10^{22}$ cm^{-2}), inconsistent with the source being located in the cloud. Finally, the present *Chandra* ACIS-S measurement loosely constraints the value of the

76

column density ($N_H = 8.2^{+3.5}_{-2.4} \times 10^{22}$ cm^{-2}).

Studying the problem from the scattering point of view, I could estimate that, if the source was in the middle of this cloud, of size between 1.6 and 4.8 pc, (value derived from Haller & Melia, 1994, observation) and located at a distance of 8.5 kpc, I expect an additional halo component. This would be located at 99.9% of the path from the observer and its profile would be ~ 5 times narrower than a halo produced by smooth and evenly distributed dust along the line-of-sight. However, such component is difficult to quantify, since the fractional distance, z, is not a very sensitive parameter: if the cloud were located at 90% of the total path, the expected size of the halo would be also a factor of five narrower, but this would place the scatterer 1 kpc nearer to us.

The fit of the surface brightness profile of 1E 1740.7-2942 strongly requires, in addition to a diffuse emission, a second component placed at $z > 0.7$ containing $\approx 40\%$ of the total dust available (Figure 6.2). This component includes the dust in the spiral arms, intercepted by the line of sight.
The analysis of the scattering morphology cannot be conclusive on the relative locations of the star and the cloud. Nevertheless, the location of this source in the N_H-τ_{sca} and in the A_V-τ_{sca} diagrams (Figure 6.1), strongly indicates that the source is located in a dust-dense region.

6.3.4   The structure of the interstellar dust grains

There is not a clear view on the internal structure of an interstellar dust grain. In the past it has been found that the current models tended to over-predict the number of scattering event producing the X-ray halo emission. To solve this discrepancy it has been proposed (*e.g.*, Mathis et al., 1995, PS95) that the grains are not compact, but contain many holes and voids. This "fluffiness" structure would provide the same amount of extinction, but less scattering. Fluffy grains could also eliminate the so called "carbon crisis" in the ISM: in order to justify the measured extinction, more carbon was needed than was actually available in dust grains (Cardelli et al., 1996). However, the fluffy grain model has not been generally accepted. Dwek (1997), for example, pointed out that the increased absorbing power of the fluffy grains would produce an excess of infrared emission which would have been in disagreement with the IR observations. On the other hand, Smith & Dwek (1998) investigated the possibility that an erroneous use of the R-G approximation for the calculation of the scattering cross section would have been the cause of the discrepancy halo-model. The R-G approximation indeed deviates significantly from the Mie theory below 2 keV: the scattering cross section, calculated with the R-G approximation is $\sim 29\%$ larger at 1 keV and ~ 4.5 times larger at 0.3 keV (Figure 6.9).

I have investigated this problem starting from the correlations found by PS95

between A_V, τ_{scatt} and N_H (Figure 6.1). Given a scattering optical depth of 1, one can extrapolate a value for the absorption equivalent hydrogen column density N_H, and from it, using tabulated elemental abundances, the absorption column density N_X relative to the most important constituents of the ISM, for instance C, N, O, Fe, Mg, S, and Si (O and N in the form of ice coatings). The absorption column density N_X value can be compared with the *scattering* column density for the element X. The latter can be calculated analytically, in the R-G approximation (PS95, Mauche & Gorenstein, 1986):

$$\sigma_{scatt}^X = N_{grain}^X \tau_{scatt} = 1.1 \times 10^{-11} \left(\frac{2Z}{M}\right)^2 \left(\frac{\rho}{3}\right)^2 a(0.1\mu m)^4 E(\text{keV})^{-2} \left[\frac{F(E)}{Z}\right]^2 \text{ cm}^{-2}$$

$$(6.3)$$

where ρ is the density, M the molecular weight, Z the atomic charge and $F(E) = |f' + if''|$ is the atomic scattering factor (§2.4.1). In the PS95 calculation, single elements were considered, assuming that condensed matter may be modeled as a collection of non-interacting atoms. This assumption is in general a good one for energies sufficiently far from absorption thresholds (Henke et al., 1993). Assuming also complete depletion of the elements, PS95 found that the sum of their contribution to the scattering optical depth would have been much higher than 100%. This led to the conclusion that a filling factor (< 1) should be added to the grain density distribution. In the present calculation I followed a slightly different approach in calculating the interesting physical quantities.

Rayleigh-Gans approximation *vs* the exact Mie solution

This enters in the calculation of both the absorption and the scattering column density, N_X and N_{grain}^X respectively:

(i) The calculation of $\tau_{scatt}(1 \text{ keV})$ in Figure 6.1 relies on the E^{-2} dependence of the total scattering cross section σ_{scatt} (cf. equation 6.2). If calculated on the basis of the Mie total scattering cross section, rather than the R-G approximation, the value of $\tau_{scatt}(1 \text{ keV})$ is lower by up to 20%, depending on N_H (Figure 6.8). The correlation then becomes:

$$\tau_{scatt}(1\text{keV}) = 0.039 \times N_H(10^{21}\text{cm}^{-2}) - 0.046. \qquad (6.4)$$

Thus, at an optical depth $\tau_{scatt}(1\text{keV})$ of unity, N_H is 2.67×10^{22} cm^{-2} instead of 2.3×10^{22} cm^{-2}, as extrapolated from PS95.

It should also be noted that the measure of N_H via spectral fit might be misleading, for, if the amount of photons *scattered* away from our line of sight (that is, subtracted from the observed flux) is significant, N_H becomes a measure of the extinction (absorption + scattering). However, relying on the A_V vs N_H correlation (Figure 6.1),

implemented in the fitting program XSPEC, N_H changes by $\sim$14% for an optical extinction of 20 mag ($N_H \sim 5 - 6 \times 10^{22}$cm^{-2}). Thus, for the N_H determination, for the sources of the ROSAT sample, this effect is not a concern.

(ii) The scattering cross section is not computed analytically (using eq. 6.3), but rather using Mie theory as described in §4.3.5. As already mentioned, the difference between the curves is $\sim$30% at 1 keV (Figure 6.9).

The grain size distribution

The reference value for the dust grain size has always been 0.1 μm. I computed the scattering cross section assuming a MRN distribution in the range a=0.005-0.25 μm, finding that indeed a significant difference, using the MRN distribution rather than a single grain size, can be appreciated only for energies below 0.2 keV (Figure 6.9).

The elemental abundances

In order to calculate the absorption column density of the element X, N_X, I considered both solar abundances (from Grevesse & Sauval, 1998, GS98 in Table 6.3) and the ISM abundances, recently listed by Wilms et al. (2000, and references therein, WAM00 in Table 6.3). The ISM abundances consider both the gas and the dust phase. The depletion value is the ratio of gas to the total amount of matter and for a species X, and it is defined as 1-β_X. Of course 1-β_X=1 if the element is totally in gas phase. Traditionally 1-β_X has been taken zero for heavy elements (*e.g.* Morrison & McCammon, 1983, MM83 in Table 6.3). In this study I considered also revised depletion values (Shull, 1993).

The result of this study is summarized in Table 6.3. The value for N_X^{Abs} is calculated according to the abundances set listed above, choosing the depletion according to MM83 or WAM00, listed between squared brackets. The value for N_X^{scatt} is calculated using the Mie theory. In the last column, I compare the number of particles able to absorb with the number of the scatterers and I list their contribution (N_X^{Scatt}/N_X^{Abs}). It is evident that the fractional contribution varies considerably depending on the abundances considered. If we consider just the upper values, which correspond, in all cases but oxygen, to the GS98 solar abundances, we see that iron grains alone would be sufficient to account for all the scattering at optical depth one. In this case the fluffiness hypothesis would be justified, as it would effectively reduce the "scattering power" of each grain.

Considering instead the lower values of the last column, and adopting both the ISM abundances and the depletion factors of WAM00, the total contribution would be $\sim$135%. While the error on the solar abundances of GS98 is only 0.06dex[1], for the

---

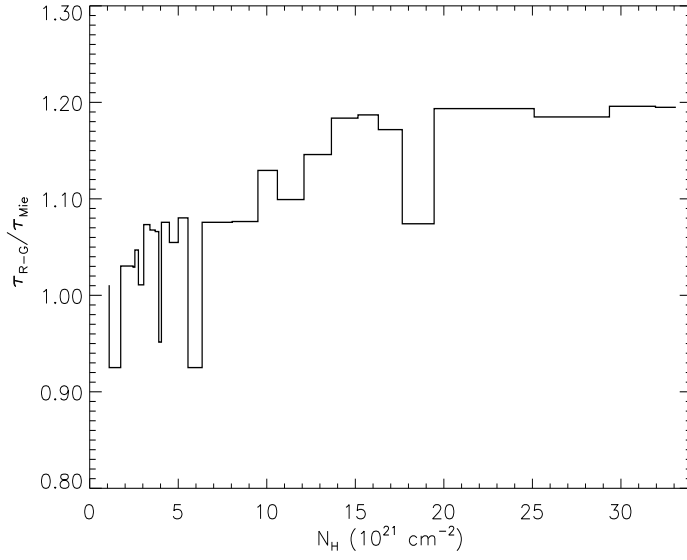[1]Quasi-unit of logarithm to base 10: 1dex=log10

Figure 6.8: Ratio between the derived τ_{scatt} at 1 keV in the case of the R-G approximation and Mie theory vs the equivalent hydrogen column density, N_H. The maximum discrepancy is of the order of 20%. The lower points are due to the intrinsically absorbed sources (see Figure 6.1).
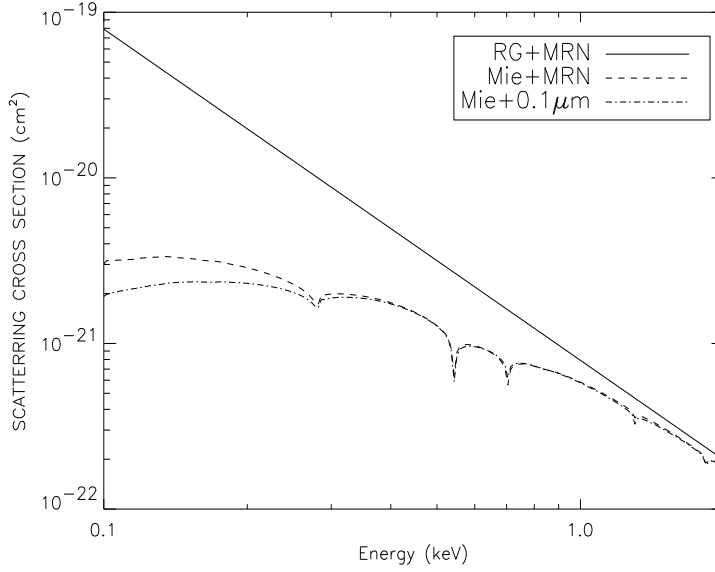

Figure 6.9: Comparison between the R-G approximation (solid line) and the Mie theory for the total scattering cross section vs energy. The cross section using the Mie theory was computed using the MRN grain size distribution (dashed line) and a single grain size of 0.1 μm (dashed dotted line).

ISM it is $\sim$0.1dex. This implies that the values of N_X^{Abs}(GS98) (and thus the higher fractional contributions) do not change dramatically if the error is included in the calculation, while the lower fractional contributions may change significantly. In the case of carbon, for instance, the minimum fractional value is 35%, but may go down to 18% if we take into account the error on the abundances. The summed contribution of the individual elements can be easily lowered to less (or around) 100%, making the fluffiness of the grains a less fundamental ingredient of the dust grain distribution.

Table 6.3: *Test of the fluffiness hypothesis. The N_H assumed to reach a τ_{scatt} of 1 is 2.67×10^{22} cm^{-2}. The last column lists the contribution, in terms of % of a column density, of a single element to a scattering depth $\tau_{scatt}=1$.*

Element	N_X^{Abs}(GS98)^2 [1-β_X=MM83]	N_X^{Abs}(WAM00)^2 [1-β_X=MM83]	N_X^{Abs}(WAM00)^2 [1-β_X=WAM00]	$N_X^{scatt2,3}$	min-max contr. %
C	8.8 [0.0]	6.4 [0.0]	3.2 [0.5]	9.0	35-97
N^1	2.2 [0.0]	2.0 [0.0]	... [1.0]	17.0	0-13
O	4.4 [0.75]	3.2 [0.75]	5.2 [0.6]	16.0	20-32
Mg	1.0 [0.0]	0.6 [0.0]	0.5 [0.2]	9.6	5-10
Si	0.9 [0.0]	0.5 [0.0]	0.4 [0.1]	5.0	8-18
S	0.6 [0.0]	0.3 [0.0]	0.1 [0.6]	4.03	2.5-15
Fe	0.8 [0.0]	0.7 [0.0]	0.5 [0.3]	0.76	65-105

[1] N is considered completely depleted by Morrison & McCammon (1983) and completely in gas phase by Wilms et al. (2000).

[2] in units of 10^{18} cm^{-2}.

[3] The assumed densities (in g/cm^3) to calculate N_X^{scatt} :
C=2.02, O,N=0.99, Mg=1.73, Si=2.33, S=2.02, Fe=7.87 (Henke et al., 1993).

6.4 Absorption by interstellar dust: the sample

In Table 6.4 I list the sample of sources chosen for the investigation of X-ray Absorption Fine Structures (XAFS, §2.3) due to dust using the HETG on board *Chandra*. Along with the celestial coordinates, the values of the N_H and the flux in the energy range 0.5-2 keV are also listed. They were selected from the public archive of *Chandra* primarily according to their brightness in the X-ray band. High statistical sampling is necessary to identify structures with depths of just few percent of the depth of the related absorption edge. In order to ensure that a conspicuous amount of dust is present along the line of sight, the Galactic latitude was also restricted to $b < 4°$. However, the disadvantage of a high flux in the soft X-ray band is the aspect of pile-up,
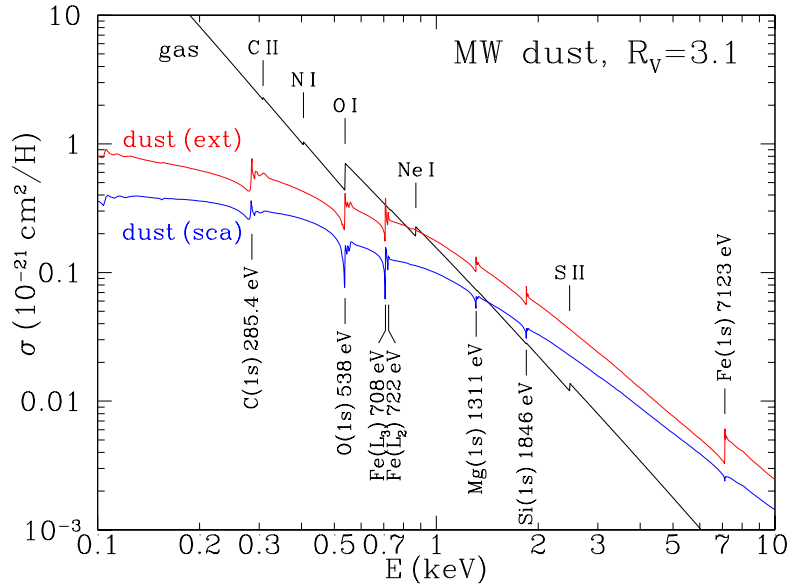
Figure 6.10: X-ray extinction and scattering cross section per H nucleon due to dust (Draine, 2003b)

that in some cases made the analysis impossible, especially at the energy of Si (for GX 9+1, for instance). Fainter source fluxes, that is more absorbed spectra, have the advantage to mitigate the pile-up effect, but at the price of lowering the statistics at softer energies. The most extreme case are GX 301-2 and 1E 1740.7-2942, where the soft energy part of the spectra was totally obliterated by ISM absorption.

Table 6.4: Main Parameters of Chandra HETG objects.

source	Type	l^{II}	b^{II}	RA	DEC	Exposure (ksec)	N_H (10^{22} cm^{-2})	Flux$_{[0.5-2\text{keV}]}$ (erg cm^{-2}s^{-1})
GX 5-1	LMXB	5.1	-1.0	18 01 08	-25 04 31	10	3.3	4.17×10^{-10}
GX 340+0	LMXB	339.59	-0.08	16 45 47.7	-45 36 40	23	5.9	2.2×10^{-11}
GX 301-2	HMXB	300.10	-0.04	12 26 37.6	-62 46 13	59	10.	...
GX 9+1	LMXB	9.08	+1.15	18 01 32.3	-20 31 44	7	1.7	5.9×10^{-10}
1E 1740.7-2942.	LMXB	359.15	-0.12	17 44 02.7	-29 43 25	70	140	4.7×10^{-15}
GRS 1758-258	LMXB	4.51	-1.36	18 01 12.3	-25 44 36	30	1.8	6.9×10^{-11}

6.4.1 Absorption features by dust grains

Interstellar dust grains play a role in the extinction of sources especially at those energies where the total cross section for dust becomes comparable with or higher than

that of the gas (Figure 6.10). Therefore, I focused on the Mg and Si edges, which should have sufficient statistics, given the high column densities towards these sources (Table 6.4).

The Mg and Si edges for GX 5-1 are shown in detail in Figure 6.11. A normal edge model, superimposed on the best-fit continuum, is not sufficient to explain the data which shows significant (4σ, Figure 6.12) residuals for the Si edge. From Figure 6.11 to Figure 6.14, the results for the Si edge are plotted, while the Mg edges are shown in Figure 6.16. For comparison, the region of Mg and Si for Cyg X-1 ($N_H = 6.7 \times 10^{21} \mathrm{cm}^{-2}$) are also shown (Schulz et al., 2002, Figure 6.15).

These detected features, called in general XAFS (X-ray Absorption Fine Structure), were identified as XANES, X-ray Absorption Near Edge Structure. These are in particular the signature of a multiple scattering of the photoelectron wave with the neighboring atoms inside the grain itself. On the contrary, the other typical solid particles absorption features, EXAFS, would require a even higher resolution to be detected, since they appear as relatively smooth modulations of the spectral continuum. However, the spectrum shows additional complexity at the higher energy side of the Si edge around 6.4 Å as predicted for EXAFS modulation (Figure 6.11). The same kind of spectral complexity was found in GRS 1915+105 (Lee et al., 2002), as is shown in Figure 6.13.

It is remarkable that for GX 5-1, GX 340+00, GRS 1915+105, and GRS1758-258 the most prominent absorption "teeth" lie, to the first approximation, at the same energy offset from the nominal edge energy. The first is at 6.7 Å (1.850 keV) for all sources, $\sim$11 eV away from the edge energy . The second, around 6.65 Å (1.864 keV), may be the blend of two features, as evident in Figures 6.11,6.14. A tentative way to identify the compound responsible for the absorption would be to compare our data with the laboratory measurements. Qualitatively, the depth of the XANES seems to be a function of the electron population in the compound and, the simpler the structure, the deepest the first tooth compared to the second (Farrell & Fleet, 2001). Moreover, the distance of the first tooth from the energy edge is found to correlate with the square of the electronegativity of the bonding ligands (Wong et al., 1995). Measurements of this kind were carried out with accuracy for very few Si compounds (e.g., Fröba et al., 1995; Wong et al., 1995), none of which were typical ID silicate. Nevertheless we can rule out absorption by some materials on the basis of the distance of the first peak (Wong et al., 1995, Si and SiC,). SiO_2 lies $\sim$9 eV away from the edge, which may not be ruled out. However the measurements show that the second tooth for SiO_2 is four times shallower, which is not consistent with these data.

The two absorption features in the data could be the superposition of two "light" compounds, where each of the tooth is a primary peak or, more probably, a compound

with a heavier element (*e.g.* Mg, Fe). Although it is expected that Mg and Si are strongly coupled in the ID, the connection between the XANES around the Si and Mg edges cannot be conclusively determined, due to the lack of laboratory measurements for comparison.

Examining a sample of the brightest sources lying in the Galactic plane, I found that, non surprisingly, the positive detection of XAFS correlates with the mean column density of dust along the line of sight, N_H. For instance, Cyg X-1, an excellent candidate for its brightness, does not show evidence of such structures. Its column density ($N_H = 6.7 \times 10^{21}$cm^{-2}) can be then considered as a lower limit for a positive detection. The upper limit is about ten times higher, indeed for sources with $N_H > 8 \times 10^{21}$ cm^{-2} the absorption is so strong that even the edges themselves disappear from the spectrum.

6.4.2   Abundances in the ISM

Taking advantage of the high spectral resolution of *Chandra* -HETG, I also estimated abundances, where the statistics allowed a direct measure of the optical depth, of the most prominent ISM absorption edges in our sample (see §5.3.2 for the formulae and approximations used). I inferred the equivalent hydrogen column density, starting from the elemental column density N_X and taking into account ISM abundances (Wilms et al., 2000). As seen in Table 6.5, the Si abundance is systematically higher than the solar value, except for Cyg X-1 which also has the lowest N_H (6.7×10^{21}cm^{-2}, Schulz et al., 2002) of our sample. At the same time, the abundances derived from the magnesium edge are consistent within the errors with the tabulated values.

Table 6.5: *Interstellar Abundances inferred from the Mg and Si edges optical depth, using solar abundances from Wilms et al. (2000).*

source	N_H $\times10^{22}$cm^{-2}	τ^{Si}	N_H^{Si} $\times10^{22}$cm^{-2}	τ^{Mg}	N_H^{Mg} $\times10^{22}$cm^{-2}
GX 5-1	3.1 ± 0.04	0.40 ± 0.01	7.2 ± 0.2	0.33 ± 0.03	3.6 ± 0.3
GRS 1915+105	5.3 ± 0.04	0.47 ± 0.01	8.4 ± 0.2	0.29 ± 0.03	3.1 ± 0.3
GX 9+1	1.7 ± 0.04^1	0.35 ± 0.03	5.7 ± 0.3	0.17 ± 0.04	1.84 ± 0.4
GRS 1758-258	1.8 ± 0.05	0.13 ± 0.02	2.3 ± 0.4	0.16 ± 0.02	1.7 ± 0.2
Cyg X-1	0.67 ± 0.003	0.03 ± 0.004	0.28 ± 0.03	0.08 ± 0.004	0.78 ± 0.05

[1] The Si edge is measured from a short frame time observation, pile-up-free.

The ISM is not homogeneous and the abundances values are means over many lines of sight. In this sample, the sources which show an overabundance of Si are located very near to the Galactic Center, where the environment may well be dustier and

denser than the average ISM. From the theory, we know that for energies above the Mg edge the extinction is made almost totally by dust grains, (Figure 6.10). Indeed the dust extinction cross section is strongly dominant over the gas phase cross section above $\sim$1 keV (Draine, 2003b). The main components of ID, together with carbon, are olivine (and pyroxenes): $Mg_{2x}Fe_{2-2x}SiO_4$ ($Mg_xFe_{1-x}SiO_3$) (Chapter 2). It has been calculated that if only these compounds are considered, their abundance is enough to account for the depletion of Si and Mg (Whittet 2003). If we rely on the values of Table 6.5, Si is approximately twice the solar abundance. It may be that Si is coupled more with Fe than with Mg, despite the prediction that the Mg to Fe ratio should be 5:2. However, this possibility cannot be tested with the present sample, lacking reliable estimates for iron abundances, since the Fe L edge (E$\sim$0.70 keV) is too heavily absorbed, and the Fe K edge at 7.1 keV from ISM could be marginally detected only in GX 340+00. In this work, only in the RGS data of Cyg X-2 and GX 339-4 (Chapter 5) could the iron contribution be measured. The abundance of iron was consistent, in first approximation, with the ISM value. However, the iron abundance measurement for Cyg X-2 could be misleading since this object lies in a different environment from the *Chandra* sources, with a lower N_H where the medium is believed to be smoother and diffuse. The environment of GX 339-4 is on the contrary more similar to the sources in the *Chandra* sample, being located at the same latitude as GX 340+0, but 4° above the Galactic plane. In this scenario, Fe and Mg would be in the expected forms in dust grains: the large majority of Mg is in silicates, while Fe locked in silicates but also in other compounds (Whittet 2003). The remaining Si would be then in other forms, simple quartz (SiO_2, SiO_4) or combined with rarer elements, like for instance aluminum (Al_2SiO_4). However, the XAFS analysis could rule out a major contribution of SiC and SiO_2 to the Si absorption edge.
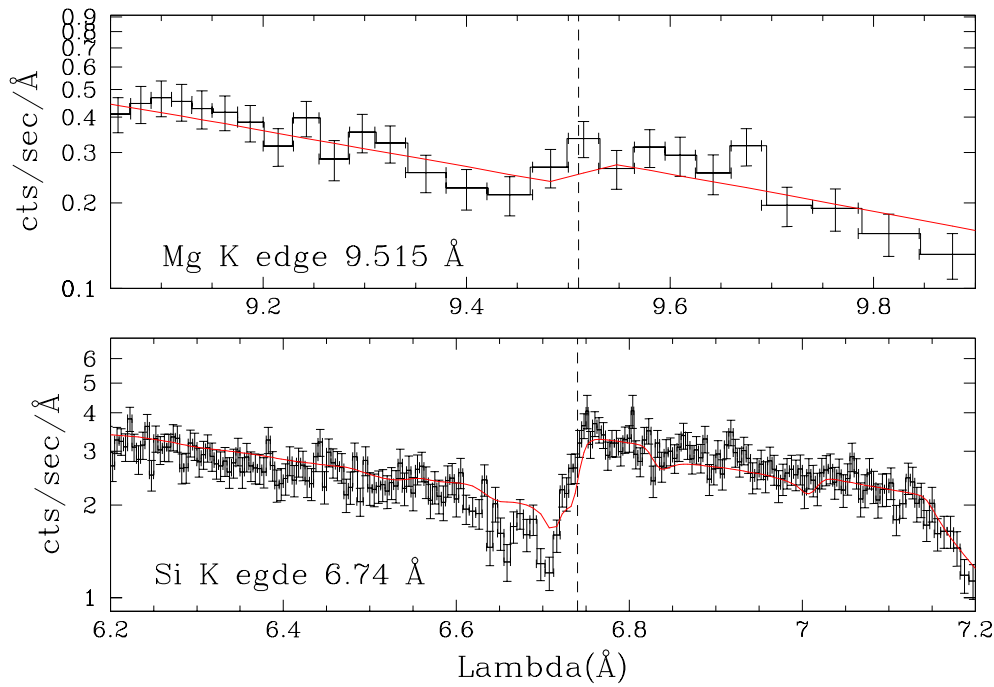
Figure 6.11: Data vs model for GX 5-1 around the Mg (top) and Si (bottom) edges. A simple single edge model (solid line) does not explain the substructures.
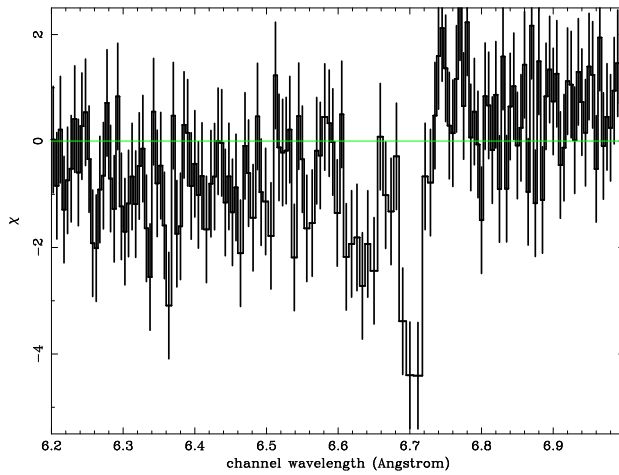

Figure 6.12: Residuals of a single edge model in terms of significance σ for the region around the Si edge. The error bars are of 1σ.
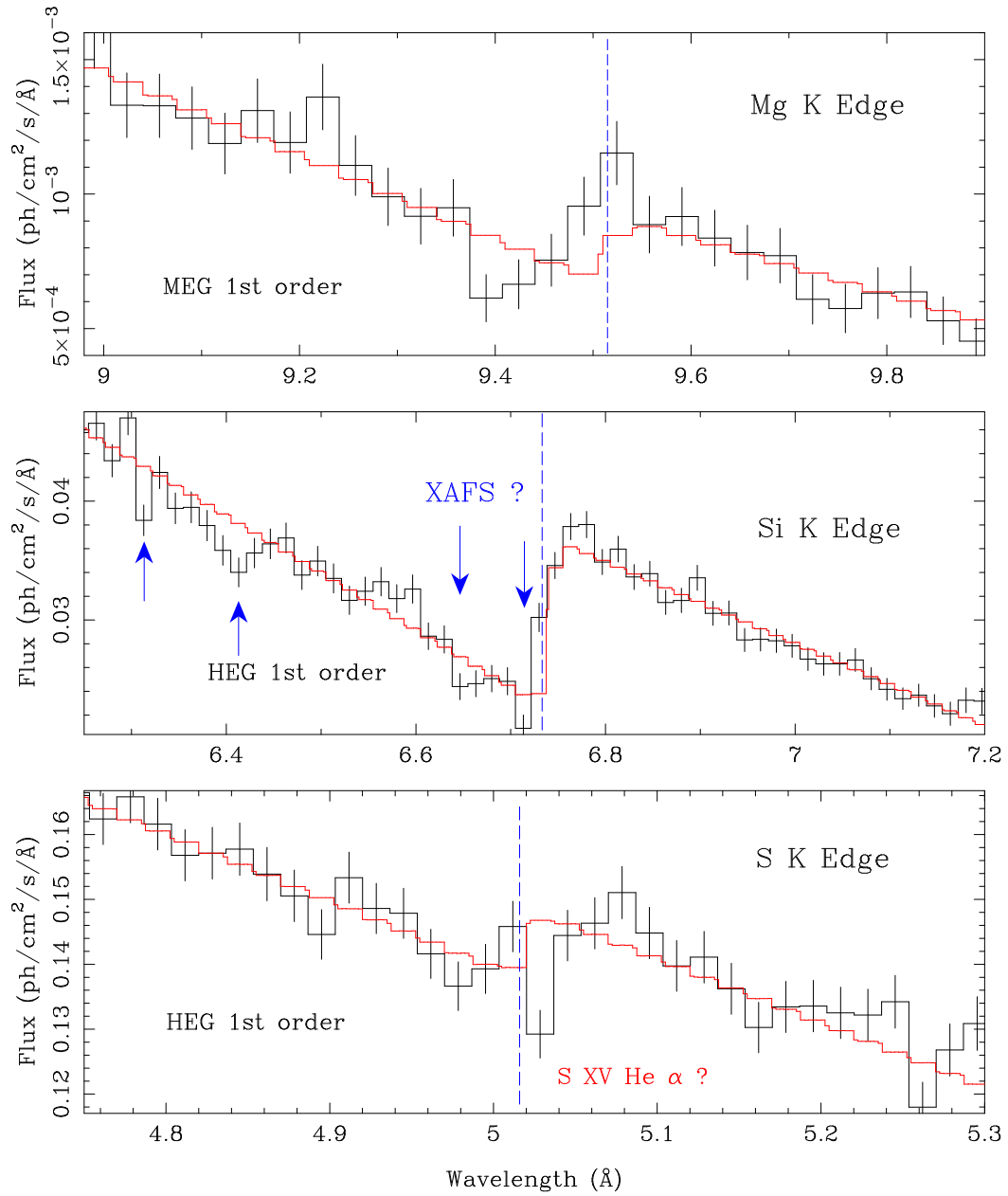
Figure 6.13: Data vs model for GRS 1915+105 around the Mg, Si and S edges (from top to bottom). The same structures as in GX 5-1 are detected (Lee et al., 2002).
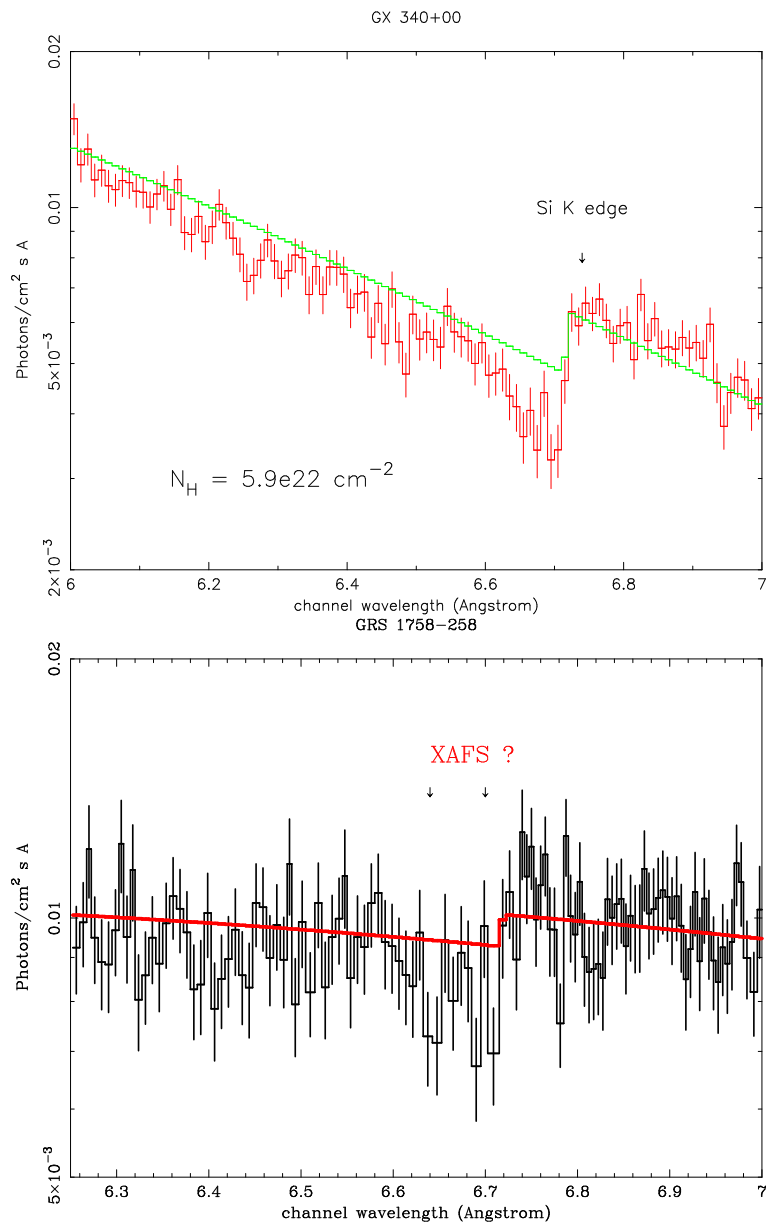
GX 340+00

Si K edge

$N_H = 5.9e22$ cm^{-2}

GRS 1758−258

XAFS ?

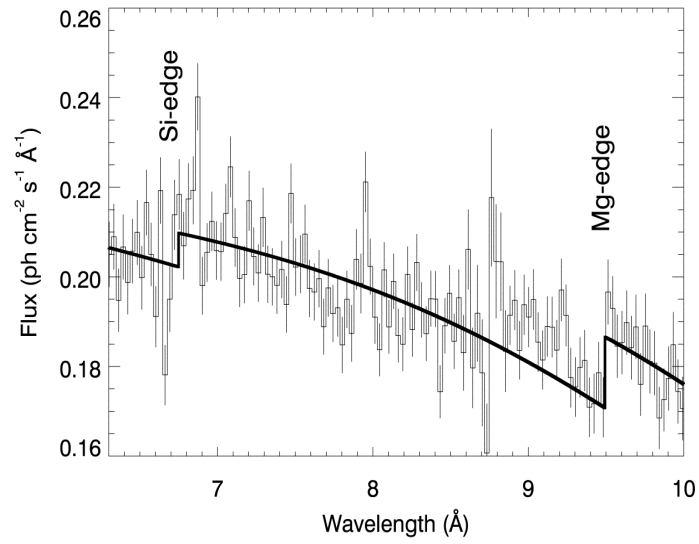Figure 6.14: *Detail of Si for two in the sources of the present sample. From top to bottom: GX 340+00, GRS 1758-258.*

Figure 6.15: Cyg X-1 (Schulz et al., 2002) Mg and Si edges are plotted for comparison with the present sample. There is no evidence of XAFS in Cyg X-1 data.

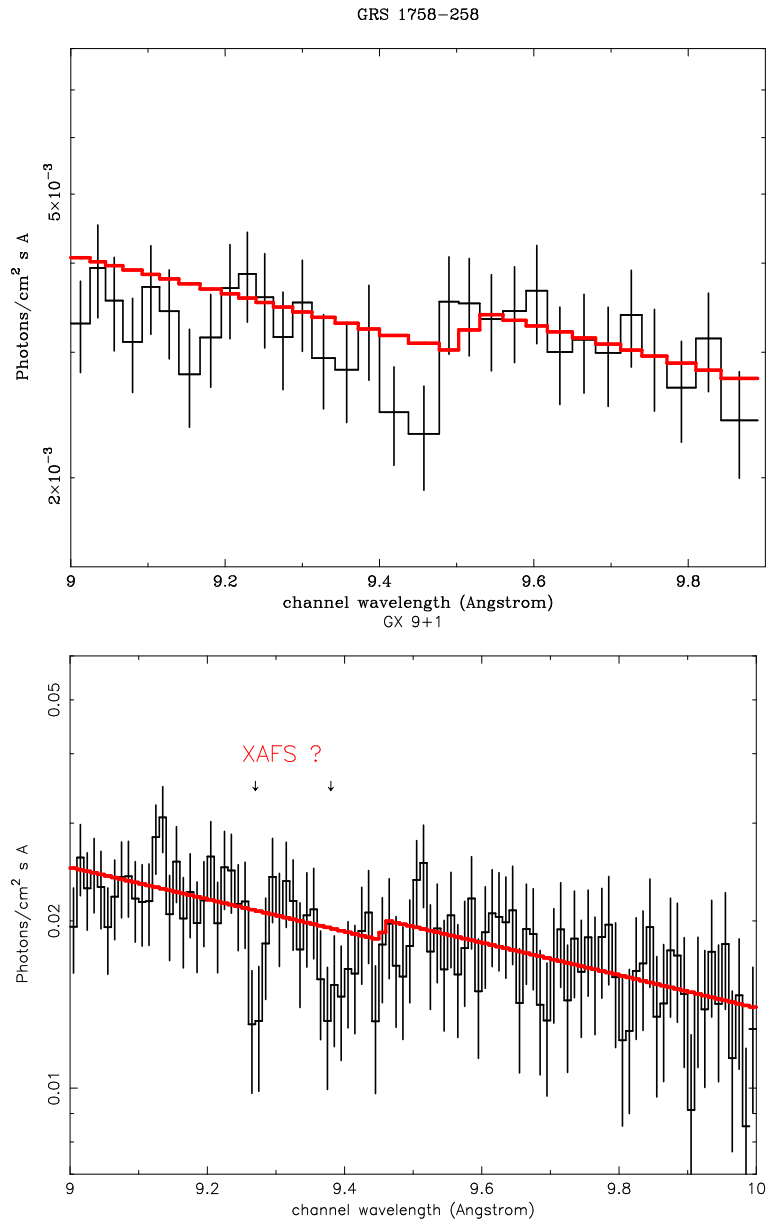Figure 6.16: Detail of Mg for two of the sources of the present sample. From top to bottom: GRS 1758-258, GX 9+1.

Chapter 7

Conclusions

The results from the X-ray observatories *Chandra* and XMM-Newton, led to advancements in our knowledge of interstellar dust as seen in the X-rays. In this work I considered two aspects of the interaction between the interstellar dust grains and the X-rays : absorption and scattering of the radiation from a luminous background source. The former was best studied through the high energy resolution of the spectrographs, XMM-RGS and *Chandra*-HETG. The scattered X-ray radiation, which produces a halo of faint and diffuse emission, was investigated using the large field of view of the CCDs: *Chandra*-ACIS and XMM-EPIC-pn.

7.0.3 Absorption by interstellar dust

The study of the absorbed radiation by interstellar dust led to important results, summarized here:

• First, the tentative detection of absorption features which are the unmistakable signature of absorption by solid grains, the so called X-ray Absorption Fine Structure (XAFS). They may appear as extra absorption "teeth" within a normal X-ray absorption edge and they are the result of the interaction between the photoelectrons inside the solid grains itself.

Among the brightest sources, the more absorbed ($N_H \sim few \times 10^{22}$ cm^{-2}) by the ISM, show evidence of XAFS near the absorption edges of Mg and Si. In particular, the spectra of GRS 1915+105 (Lee et al 2001), GX 5-1, GX 340+00, GRS 1758-258 observed by the *Chandra*-HETG, show at least two, very significant, substructures especially near the Si edge. Moreover, all sources show the same spectral pattern in that region.

Above atomic number of oxygen, the elements in the ISM are almost completely locked in solid grains and Mg and Si are believed to be among the fundamental com-

ponents of dust, in the form of olivine or pyroxene, for instance (*e.g.* Whittet 2003). In principle, the distance of such "teeth" from the edge energy is proportional to the distance of the electrons from the nucleus. Indeed, precise laboratory measurement can distinguish among different types of compounds of that specific element, from the distance parameter. Astrophysical data are far from having the required statistics for this identification. However, the published laboratory results were used for comparison with the present data: *(i)* the complexity of the pattern and the depth of the "teeth" suggest absorption by a heavy compound (not as light as SiO_2, but rather Mg or Fe compounds). *(ii)* The distance in energy of the first, and more prominent, "tooth" from the edge energy is not consistent with absorption by Si and SiC (Fröba et al., 1995).

- The sources lying behind a relatively thin layer of dust ($N_H \sim few \times 10^{21}$ cm^{-2}) are less absorbed and enable the study of lower energy features, such as the oxygen edge at ~ 0.54 keV. Oxygen is believed to be an important component both in the gaseous and solid phases of the ISM (depletion of $\sim 25\%$, Wilms Allen & McCray, 2000). I studied, in great detail, the oxygen structure of Cyg X-2 and GX 339-4, two bright ($L \sim 10^{39}$ erg sec^{-1}) X-ray binaries observed by XMM-RGS. Below the edge jump, a number of resonant absorption lines were detected. Thanks to recent laboratory experiments (*e.g.* Gorczyca & McLaughlin 2000, Kortright & Kim 2000), I could identify these as transitions of OI, OII and OIII. They are likely to be features of the ISM, mostly because they seem to be ubiquitous, although with different intensities, when the statistics allows the detection. These features were indeed also observed in a sample of binaries observed by *Chandra* (Juett et al 2003). The contribution of weakly ionized oxygen may well originate from the ISM in the vicinity of the source. Moreover it solves the problem of the apparent underabundance of oxygen in the ISM, if estimated from the neutral features alone. Unfortunately, due to a lack of comparative laboratory measurements, the possibility for OII and OIII features instead being interpreted as absorption by molecular oxygen cannot be either confirmed or denied

7.0.4   Scattering by interstellar dust

The radiation scattered by dust could be also studied with unprecedented precision:

- The high throughput offered by the XMM instruments enables to study the faintest halos, produced by the least amount of dust necessary to scatter the radiation. Brighter halos where investigated using *Chandra*.
Two complementary approaches were used to study the scattered radiation: imaging and spectroscopy. The analysis on the images enabled the Surface Brightness Profile

(SBP) of the source to be modeled at various energies. In addition, I investigated the spectral properties of the scattered emission, such analysis has never been performed previously.

This dual analysis aspect, gave me the opportunity to test different, and sometimes controversial, aspects of the scattering halos theory.

(i) The limits of the validity of the so called Rayleigh Gans approximation were investigated. This study proves this approximation to be completely misleading at energies below 1 keV and this confirms earlier suggestions from studies with ROSAT (Smith & Dwek 1998). Instead, the complete Mie theory for scattering of solid spherical particles was used, which takes into account the very strong energy dependence of the scattering cross section with energy. The necessity to use the complete Mie theory was evident in the halo *spectral* analysis, but for the *spatial* analysis, where the energy is always confined to a known, small, range, the largest departure from the detailed theory and the Rayleigh-Gans approximation is only in the normalization. This holds especially in the range 1-2 keV, far from the absorption energy of the ID elements.

(ii) The classical model for the dust grain size distribution in the ISM (Mathis Rumpl & Nordsieck 1977) was tested against the modern Weingartner & Draine (2001) model. The latter takes into account the newer results achieved through infrared observation of interstellar dust. On this respect, the results of this comparison are not conclusive. The differences between the two models result in nuances that cannot be fully appreciated by the X-ray data. Although I cannot conclusively differentiate between the two dust models, my analysis can constraint two aspects: dust grains with large size ($a > 0.25 \mu m$) were not required to explain the data; the single scattering approximation seems to be adequate in the fitting of the data.

(iii) The structure of an interstellar grain was often claimed to be porous (fluffy). Starting from the correlation N_H vs τ_{scatt} at 1 keV (PS95), I tested the "fluffiness" hypothesis by comparing, for each relevant element in the interstellar dust, the number of grains available for absorption with the number of grains available to scatter. PS95, used the Rayleigh-Gans approximation and solar abundances, considered the complete depletion of the heavy elements and found that fluffiness was required. Without "fluffiness" for the contribution of the elements to a scattering optical depth of 1 would have been much greater than 100%. In the present analysis, I used the Mie theory and a different set of abundances and depletions, which are believed to be more representative of the ISM (Wilms et al., 2000). In contrast, my analysis, considering also the uncertainties on the abundances values, shows that the sum of the contributions of the single elements to the optical depth is near or lower than 100%, therefore the fluffiness of the grains is not required to explain the data.

(iv) The general correlation found by Predehl & Schmitt (1995) between absorption and scattering in the ISM, parameterized by the equivalent hydrogen column density, the visual extinction and the scattering optical depth at 1 keV, is confirmed in this

study. Although, using the Mie theory instead of the Rayleigh-Gans approximation, the slope of the N_H-$\tau_{scatt}(1keV)$ correlation is ~29% flatter. The halo objects that do not obey the relation for the most part have absorption in excess, evidence of a dense dusty environment in the vicinity of the source.

• Complementary to XMM, the exceptionally narrow point spread function of *Chandra* telescope, gave me the opportunity to study the extended emission at scales as low as a few arcsec from the center of the source. Not surprisingly, the SBP shape does not indicate smooth and evenly distributed dust along specific lines of sight. The medium indeed is known to be clumpy and the line of sight passes through portions of the spiral arms of the Milky Way. In three cases with best statistics (GX 5-1, The Great Annihilator, Cen X-3) I found that at least two components are necessary: a diffuse component which contributes for 50-70% of the scattering plus a component concentrated closer to the source. The latter produces a narrower halo which accounts for the rest of the scattering. On the contrary, in the case of the brightest sources of the Magellanic Clouds in our sample (LMC X-1, LMC X-3), the expected similar narrow component, was not detected.

• The spectral analysis of the scattering halo was performed only in three cases (once again, for statistical reasons) out of which, the best example was provided by the low absorption source Cyg X-2. The halo spectrum could be studied down to ~ 0.5 keV. I report in this thesis the unprecedented detection of the scattering features located at energies consistent with O, Mg and Si, among the more abundant components in interstellar dust. These features were predicted by the scattering theory, however were never observed previously. I tentatively fitted the continuum of the scattered emission using the two grain size distribution models above mentioned, assuming two sets of values for elemental abundances (Grevesse & Sauval 1998, Wilms Allen & McCray 2000). Although some of the parameters were loosely constrained (for oxygen above all), all the fits prefer a dust composition made by carbon and silicates. The silicates in this case seem to be composed by Mg and Fe compounds, with Mg to Fe proportion ≈5:2, in agreement with previously determined ISM values (Whittet 2003).

Appendix A

Simulating the PSEUDO-MIPs in XMM Epic-Pn Camera

In §4.1.1 the Pseudo-MIPs problem was introduced. Here the simulation program and its testing is described, using as an example the source Cyg X-2 .

The inputs are:

i) the spectral shape (S), extracted from the out of time events (OOT): the energy distribution is conserved despite the misinterpretation of the flux value. Note that the source position, rather than the recored position on the CCD, has been used for the CTI (Charge Transfer Inefficiency) correction.

ii) The value, which is practically constant across the chip, of the discarded columns number from the rejection of the *real* MIPs, from the "Discarded Line File" (DLI) of the observation (Figure 4.1).

iii) A guess on the source count rate over the whole energy band. A reasonable starting point may be converting the count rate of other mission measurements. If the source is strongly variable in a long time scale, one may keep track of its variation checking the Rossi X-ray Timing Explorer (RXTE) flux monitoring.

iv) An encircled energy profile of the inner part of the Point Spread Function. As a first step, we used the on-ground calibrated profile for the on-axis position.

The count rate is then distributed according to the spectrum S and spatially constrained by the PSF model. The number of photons per frame time (Nframe) is then calculated. The time in which the out of time events are produced (6.3% of the frame time) is also included in the simulation. A column (plus the neighboring columns at the right and left hand sides) is rejected if in a single frame time the amplitude of the charge in a pixel exceed 3000adu (15 keV). In addition, if the number of columns rejected per frame time at a given RAWX position exceeds the maximum number allowed (2^{16}), then an overflow occurs, *i.e.* an uncertainty on the number of saturation levels of the order of n. Of course, the maximum value for n is the number of frames.

A.1 Position and Energy dependence

The number of discarded lines due to pseudo-MIPs may change dramatically in dependence of the position of the peak of the source across one pixel. In Figure A.1 the discarded lines number is plotted vs the RAWX coordinate, for a beam hitting different positions along the X direction of the pixel RAWX=35, RAWY=192 , assuming a broad band rate of 4000 cts/sec, an exposure of 1 ksec and the spectral shape of Cyg X-2. In the simulation program the level of *real* MIPs in the Cyg X-2 observation is included, which results in a constant level of $\sim$9000 discarded lines in the Figure.
In the vertical axis, the value of the disregarded lines N is plotted as (N mod 2^{16}), in order to make evident the overflows. We observe that at the edge (RAWX=35.0) and at the center of the pixel (RAWX=35.5) the shape is symmetric, being the assumed PSF spherically symmetric and the central three columns have reached the saturation level at least one time.

The probability of exceeding the value of $\sim$15 keV, producing a pseudo-MIP, is dependent on the spectral shape, i.e., the hardest the spectrum, the more probable will be to exceed this value. Of course, if the source flux is particularly high, even a soft spectrum can easily produce pseudo-MIPs. In Figure A.2 such effect is explained. The simulation is run assuming again the Cyg X-2 spectral shape, but imposing the integral under the curve to be the same for the energy intervals: 0.5-1.5, 1.5-3.5, 3.5-5.5, 5.5-10 keV respectively. For a rate of 4000 c/s, and pixel coordinates 35.25,192, the central columns saturates already at energies larger than 1.5keV. For E>3.5 keV the core of the PSF completely saturates and pseudo-MIPs occurs also in the wings of the Gaussian.

A.2 The Point Spread Function

Recent calibration results (Kirsch, 2003) shows a misalignment between the source position and the optical axis, implying an off-axis angle of the order of 1 arcmin for sources believed to be on-axis. In order to estimate the PSF shape in such conditions, I performed an in-flight calibration of the core (within a radius of $\sim$ 5 arcsec) of the PSF of on-axis sources. I considered the sum of six on-axis observations of the bright star, soft spectrum, ζ Puppis, for a total exposure time of 105 ksec, in Large Window mode. Given the very short transfer time (0.16% of the frame time), the LW mode implies a negligible contribution from the OOT events to the PSF profile. In Figure A.3 the summed image is shown in RAW coordinates (1 pixel=4.1$''$), choosing the energy range 0.2-2 keV. Only single events were selected, to in order to sharpen the shape of the profile, but however the contribution of double events photons, which have the effect of smearing out, is, at this energy of $\sim$20%. In Figure A.4 the flux contours of the
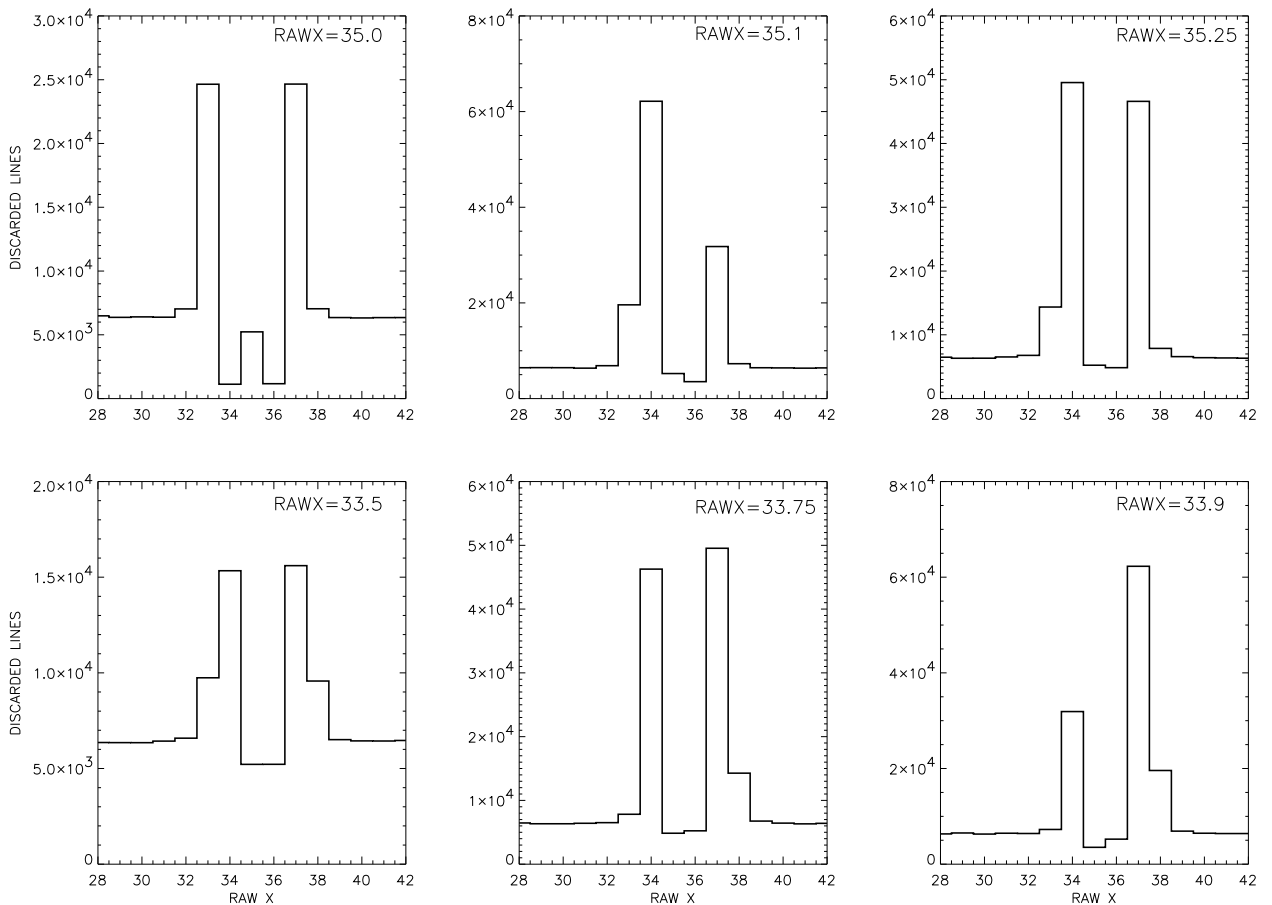
96

Figure A.1: The peak of the source is varied along the RAWX direction in the pixel 35,192.
The shape of the discarded lines is symmetric if the peak is located at the beginning or at
the center of the pixel (leftmost panels). The input rate is 4000 c/s over a 0.1-10 keV band.
The spectral distribution is from Cyg X-2 .

summed fluxes is shown. The core of the PSF shows an asymmetry in the RAWX axis,
as expected, being the optical axis shifted mostly in the RAWX direction, as indicated
in Figure A.3. However, at 1σ (where the value of the peak of the PSF drops of a
factor $1/e$) the maximum elongation does not lie in the direction of the optical axis,
but slightly south-west of it, being $\Delta\sigma$ between the two directions $\sim$0.2 pixels. The
values of the σ of a fitting Gaussian along the RAWX and RAWY axis are, starting
from the right hand side of RAWX, going counterclockwise: 1.14,0.85,1.35,1.14 pixels
respectively. At $\sim2\sigma$ the distortion of of the PSF is actually along the direction of
the optical axis. The inner part of the PSF distortion may be indeed determined
by the position of the peak across central pixel, while the outer part is due to the
misplacement of the source with respect to the optical axis.
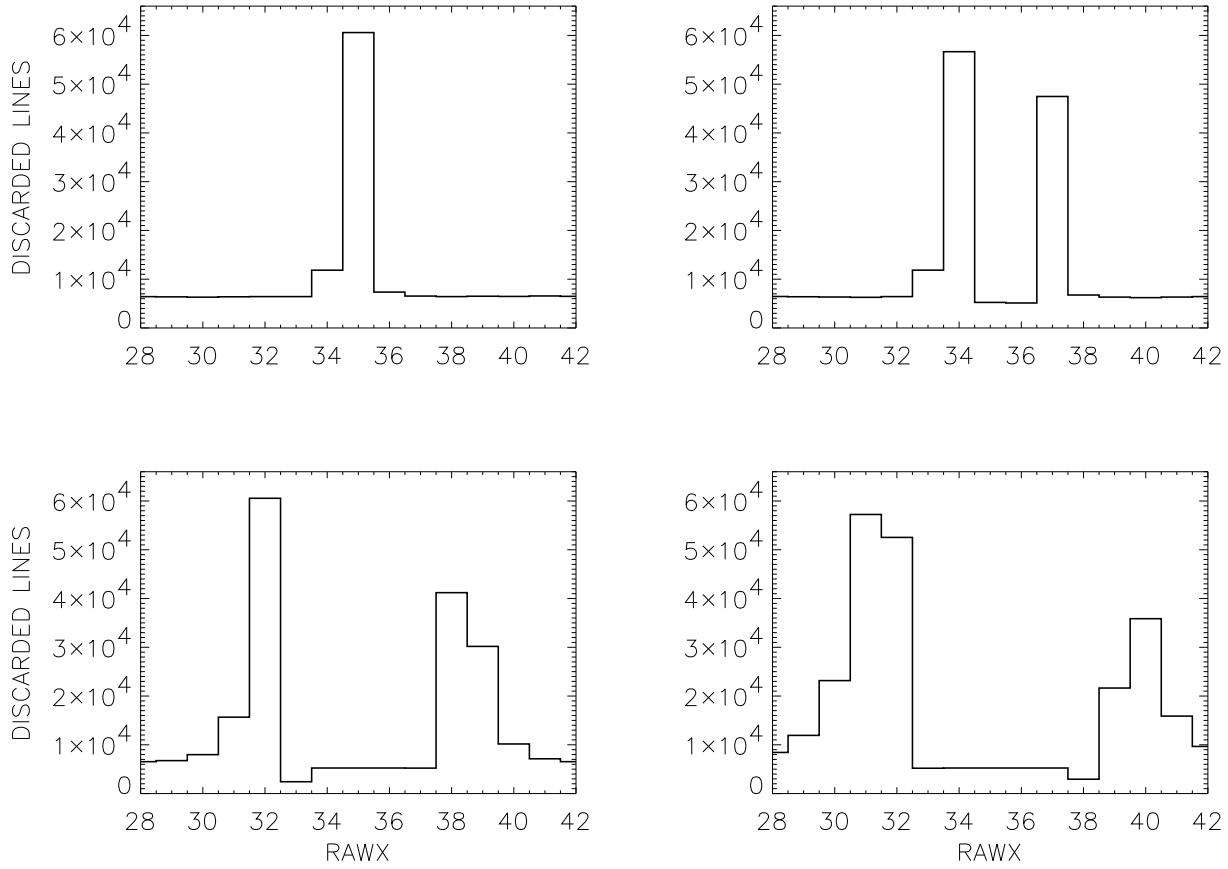
Figure A.2: The energy dependence of the discarded line profile. From top to bottom, left to right, the energy intervals: 0.5-1.5, 1.5-3.5, 3.5-5.5, 5.5-10 keV are plotted.
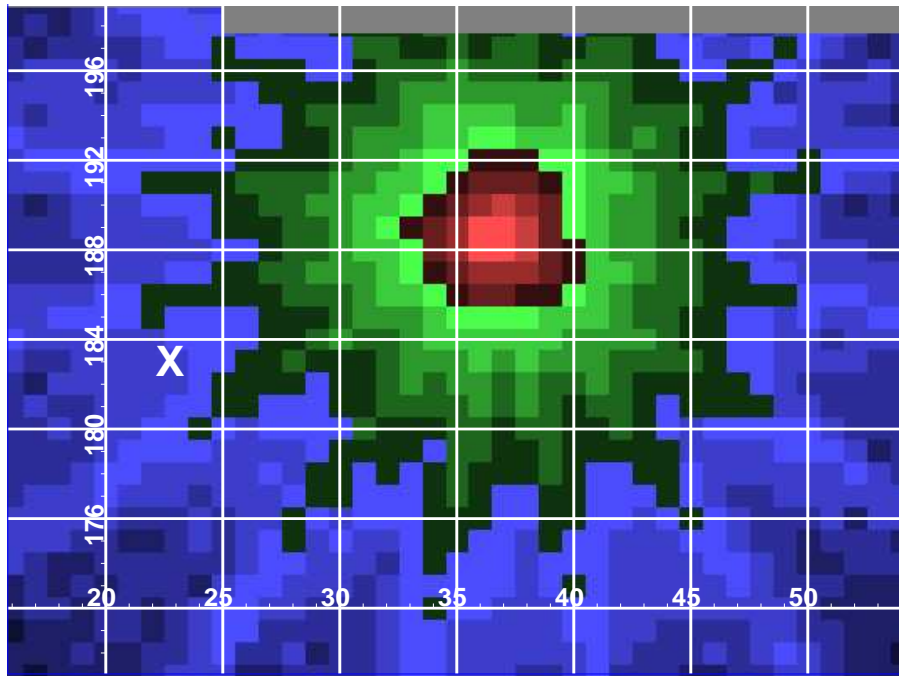
Figure A.3: The image of the sum of 6 observations of ζ Puppis in RAW coordinates. The true optical axis lies at 23,183 in RAW coordinates, indicated with an X.
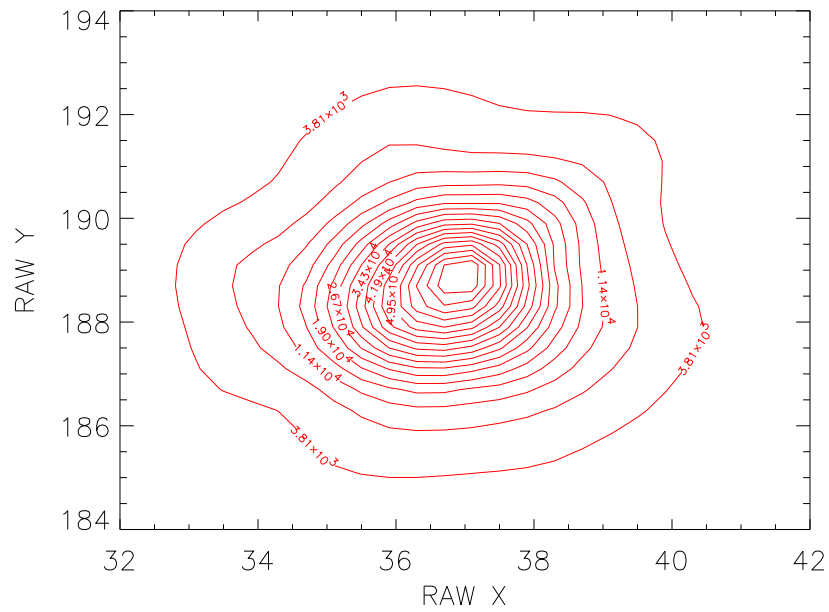

Figure A.4: The flux contours of the central 10 pixels of ζ Puppis. An asymmetry is evident on the X axis.

Bibliography

Allende Prieto, C., Lambert, D. L., & Asplund, M. 2001, ApJ, 556, L63

André, M. K., Oliveira, C. M., Howk, J. C., Ferlet, R., Désert, J.-M., Hébrard, G., Lacour, S., des Étangs, A. L., Vidal-Madjar, A., & Moos, H. W. 2003, ApJ, 591, 1000

Aschenbach, B., Citterio, O., Ellwood, J. M., Jensen, P., Dekorte, P., Peacock, A., & Willingale, R. 1987, The high throughput X-ray Spectroscopy Mission. Report of the Telescope Working Group, 53–+

Bally, J., Stark, A. A., Wilson, R. W., & Henkel, C. 1987, ApJS, 65, 13

Belloni, T., Méndez, M., van der Klis, M., Lewin, W. H. G., & Dieters, S. 1999, ApJ, 519, L159

Bevington, P. R. & Robinson, D. K. 2003, Data reduction and error analysis for the physical sciences (Data reduction and error analysis for the physical sciences, 3rd ed., by Philip R. Bevington, and Keith D. Robinson. Boston, MA: McGraw-Hill, ISBN 0071199268, 2003.)

Bohlin, R. C., Savage, B. D., & Drake, J. F. 1978, ApJ, 224, 132

Bouwman, J., Meeus, G., de Koter, A., Hony, S., Dominik, C., & Waters, L. B. F. M. 2001, A&A, 375, 950

Bradt, H. V. D. & McClintock, J. E. 1983, ARA&A, 21, 13

Brinkman, B. C., Gunsing, T., Kaastra, J. S., van der Meer, R., Mewe, R., Paerels, F. B., Raassen, T., van Rooijen, J., Braeuninger, H. W., Burwitz, V., Hartner, G. D., Kettenring, G., Predehl, P., Drake, J. J., Johnson, C. O., Kenter, A. T., Kraft, R. P., Murray, S. S., Ratzlaff, P. W., & Wargelin, B. J. 2000, in Proc. SPIE Vol. 4012, p. 81-90, X-Ray Optics, Instruments, and Missions III, Joachim E. Truemper; Bernd Aschenbach; Eds., 81–90

Cardelli, J. A., Meyer, D. M., Jura, M., & Savage, B. D. 1996, ApJ, 467, 334

Churazov, E., Gilfanov, M., & Sunyaev, R. 1996, ApJ, 464, L71+

Cohn, H. N., Lugger, P. M., Grindlay, J. E., & Edmonds, P. D. 2002, ApJ, 571, 818

Davis, J. E. 2001, ApJ, 562, 575

de Bergevin, F. 1999, in X-Ray and Neutron Reflectivity: Principles and Applications, 331

de Vries, C. P., den Herder, J. W., Kaastra, J. S., Paerels, F. B., den Boggende, A. J., & Rasmussen, A. P. 2003, A&A, 404, 959

Della Valle, M., Pasquini, L., Daou, D., & Williams, R. E. 2002, A&A, 390, 155

den Herder, J. W. e. a. 2001, A&A, 365, L7

Di Salvo, T., Farinelli, R., Burderi, L., Frontera, F., Kuulkers, E., Masetti, N., Robba, N. R., Stella, L., & van der Klis, M. 2002, A&A, 386, 535

Dickey, J. M. & Lockman, F. J. 1990, ARA&A, 28, 215

Draine, B. 1989, in IAU Symp. 135: Interstellar Dust, 313–27

Draine, B. T. 2003a, ArXiv Astrophysics e-prints

—. 2003b, astro-ph/0304489

Draine, B. T. & Lazarian, A. 1999, ApJ, 512, 740

Draine, B. T. & Tan, J. C. 2003, ApJ, 594, 347

Dwek, E. 1997, ApJ, 484, 779

Evans, A., Stickel, M., van Loon, J. T., Eyres, S. P. S., Hopwood, M. E. L., & Penny, A. J. 2003, A&A, 408, L9

Farrell, S. P. & Fleet, M. E. 2001, Physics and Chemistry of Minerals, 28, 17

Fitzpatrick, E. L. 1986, AJ, 92, 1068

Fitzpatrick, E. L. & Massa, D. 1986, ApJ, 307, 286

Fröba, M., Wong, J., Behrens, P., Sieger, P., Rowen, M., Tanaka, T., Rek, Z., & Felsche, J. 1995, Physica B Condensed Matter, 208, 65

Freyberg, M. 2003, The XMM-Newton Epic-PN camera: Spectral and Temporal Properties of the Internal Background, XMM-Newton Calibration Report, (June 2003)

Gaetz, T. 2002, Wings of the Chandra PSF, Proceedings of the 2002 Chandra Calibration Workshop

Garmire, G. P., Bautz, M. W., Ford, P. G., Nousek, J. A., & Ricker, G. R. 2003, in X-Ray and Gamma-Ray Telescopes and Instruments for Astronomy. Edited by Joachim E. Truemper, Harvey D. Tananbaum. Proceedings of the SPIE, Volume 4851, pp. 28-44 (2003)., 28–44

Ghizzardi, S. 2002, In Flight Calibration of the PSF for the PN Camera, XMM-Newton Calibration Report, EPIC-MCT-TN-012, (June 2002)

Giacconi, R. e. a. 1979, ApJ, 230, 540

Gorczyca, T. W. & McLaughlin, B. M. 2000, Journal of Physics B Atomic Molecular Physics, 33, L859

Grevesse, N. & Sauval, A. J. 1998, Space Science Reviews, 85, 161

Haller, J. W. & Melia, F. 1994, ApJ, 423, L109+

Heiles, C. 1984, ApJS, 55, 585

Heinke, C. O., Edmonds, P. D., Grindlay, J. E., Lloyd, D. A., Cohn, H. N., & Lugger, P. M. 2003, ApJ, 590, 809

Henke, B. L., Gullikson, E. M., & Davis, J. C. 1993, Atomic Data and Nuclear Data Tables, 54, 181

Holweger, H. 2001, in AIP Conf. Proc. 598: Joint SOHO/ACE workshop "Solar and Galactic Composition", 23–+

Howk, J. C., Savage, B. D., & Fabian, D. 1999, ApJ, 525, 253

Juett, A. M., Schulz, N. S., & Chakrabarty, D. 2003, ArXiv Astrophysics e-prints

Kim, S., Martin, P. G., & Hendry, P. D. 1994, ApJ, 422, 164

Kirsch, M. 2003, Improved Vignetting Correction by refining the XMM optical axis, XMM-Newton Calibration Report, (December 2003)

Königsberger, D. C., P. R. 1988, X-Ray Absorption (New York, Willey & Sons)

Kortright, J. B. & Kim, S. 2000, Phys.Rev.B, 62, 12216

Krzeminski, W. 1974, ApJ, 192, L135

Kurt, C. M. & Dufour, R. J. 1998, in Revista Mexicana de Astronomia y Astrofisica Conference Series, 202–+

Lee, J. C., Reynolds, C. S., Remillard, R., Schulz, N. S., Blackman, E. G., & Fabian, A. C. 2002, ApJ, 567, 1102

Li, A. & Draine, B. T. 2002, ApJ, 564, 803

Lillie, C. F. & Witt, A. N. 1976, ApJ, 208, 64

Liu, J., Bregman, J. N., & Seitzer, P. 2001, American Astronomical Society Meeting, 199, 0

Maejima, Y., Makishima, K., Matsuoka, M., Ogawara, Y., Oda, M., Tawara, Y., & Doi, K. 1984, ApJ, 285, 712

Marshall, H. L., Dewey, D., & Ishibashi, K. 2003, ArXiv Astrophysics e-prints

Mason, K. O. e. a. 2001, A&A, 365, L36

Mathis, J. S. 1996, ApJ, 472, 643

Mathis, J. S., Cohen, D., Finley, J. P., & Krautter, J. 1995, ApJ, 449, 320

Mathis, J. S. & Lee, C.-W. 1991, ApJ, 376, 490

Mathis, J. S., Rumpl, W., & Nordsieck, K. H. 1977, ApJ, 217, 425

Mauche, C. W. & Gorenstein, P. 1986, ApJ, 302, 371

McClure-Griffiths, N. M., Dickey, J. M., Gaensler, B. M., & Green, A. J. 2002, ApJ, 578, 176

McLaughlin, B. M. & Kirby, K. P. 1998, Journal of Physics B Atomic Molecular Physics, 31, 4991

Mendez, M. & van der Klis, M. 1997, ApJ, 479, 926

Miller, J. M., Raymond, J., Fabian, A. C., Homan, J., Nowak, M. A., Wijnands, R., van der Klis, M., Belloni, T., Tomsick, J. A., Smith, D. M., Charles, P. A., & Lewin, W. H. G. 2003, ArXiv Astrophysics e-prints

Misselt, K. A., Clayton, G. C., & Gordon, K. D. 1999, ApJ, 515, 128

Mitsuda, K., Inoue, H., Koyama, K., Makishima, K., Matsuoka, M., Ogawara, Y., Suzuki, K., Tanaka, Y., Shibazaki, N., & Hirano, T. 1984, PASJ, 36, 741

Miyamoto, S., Kimura, K., Kitamoto, S., Dotani, T., & Ebisawa, K. 1991, ApJ, 383, 784

Molster, F. J., Waters, L. B. F. M., Tielens, A. G. G. M., Koike, C., & Chihara, H. 2002, A&A, 382, 241

Morrison, R. & McCammon, D. 1983, ApJ, 270, 119

Murray, S. S., Chappell, J. H., Kenter, A. T., Kraft, R. P., Meehan, G. R., & Zombeck, M. V. 1998, in Proc. SPIE Vol. 3356, p. 974-984, Space Telescopes and Instruments V, Pierre Y. Bely; James B. Breckinridge; Eds., 974–984

Overbeck, J. W. 1965, ApJ, 141, 864

Paerels, F., Brinkman, A. C., van der Meer, R. L. J., Kaastra, J. S., Kuulkers, E., Boggende, A. J. F. d., Predehl, P., Drake, J. J., Kahn, S. M., Savin, D. W., & McLaughlin, B. M. 2001, ApJ, 546, 338

Phillips, J. A. & Lazio, T. J. W. 1995, ApJ, 442, L37

Piraino, S., Santangelo, A., & Kaaret, P. 2002, ApJ, 567, 1091

Pollock, A. 2003, Status of the RGS Calibration, XMM-Newton Calibration Report, XMM-SOC-CAL-TN-0030 Issue 2 (April 2003)

Predehl, P., Burwitz, V., Costantini, E., & Trümper, J. 2001, in ASP Conf. Ser. 251: New Century of X-ray Astronomy, 46–+

Predehl, P. & Klose, S. 1996, A&A, 306, 283

Predehl, P. & Schmitt, J. H. M. M. 1995, A&A, 293, 889

Press, W. H., Teukolsky, S. A., Vetterling, W. T., & Flannery, B. P. 1992, Numerical recipes in FORTRAN. The art of scientific computing (Cambridge: University Press, —c1992, 2nd ed.)

Rolf, D. P. 1983, Nature, 302, 46

Savage, B. D. & Mathis, J. S. 1979, ARA&A, 17, 73

Schattenburg, M. L. & Canizares, C. R. 1986, ApJ, 301, 759

Schattenburg, M. L., Canizares, C. R., Berg, C. J., Clark, G. W., Markert, T. H., & Winkler, P. F. 1980, ApJ, 241, L151

Schulz, N. S., Cui, W., Canizares, C. R., Marshall, H. L., Lee, J. C., Miller, J. M., & Lewin, W. H. G. 2002, ApJ, 565, 1141

Schulz, N. S., Juett, A., Chakrabarty, D., & Canizares, C. R. 2003, Astronomische Nachrichten, 324, 166

Sheth, S., Liang, E., Luo, C., & Murakami, T. 1996, ApJ, 468, 755

Shull, J. M. 1993, Physica Scripta Volume T, 47, 165

Skinner, G. K., Pan, H. C., Maisack, M., Staubert, R., Borozdin, K. N., Brinkman, A. C., Englhauser, J., Gilfanov, M. R., Kaniovsky, A. C., Pietsch, W., Sunyaev, R. A., & in 't Zand, J. J. M. 1991, A&A, 252, 172

Smith, R. K. & Dwek, E. 1998, ApJ, 503, 831

Smith, T. L. & Witt, A. N. 2002, ApJ, 565, 304

Sofia, U. J. & Meyer, D. M. 2001, ApJ, 554, L221

Stecher, T. P. & Donn, B. 1965, ApJ, 142, 1681

Strüder, L. e. a. 2001, A&A, 365, L18

Takei, Y., Fujimoto, R., Mitsuda, K., & Onaka, T. 2002, ApJ, 581, 307

Teo, B. K. 1986, EXAFS: Basic Principles and Data Analysis (Berlin, Springer)

Titarchuk, L. 1994, ApJ, 434, 570

Trümper, J. & Schönfelder, V. 1973, A&A, 25, 445

Trümper, J. 1982, Advances in Space Research, 2, 241

Turner, M. J. L. e. a. 2001, A&A, 365, L27

van Oijen, J. G. J. 1989, A&A, 217, 115

van Paradjis, J. 1991, Neutron Stars: Theory and Observation (Kluwer, Dordrecht)

Weingartner, J. C. & Draine, B. T. 2001, ApJ, 548, 296

Whittet, D. C. B. 1981, QJRAS, 22, 3

—. 2003, Dust in the galactic environment (Dust in the galactic environment, 2nd ed. by D.C.B. Whittet. Bristol: Institute of Physics (IOP) Publishing, 2003 Series in Astronomy and Astrophysics, ISBN 0750306246.)

Whittet, D. C. B., Gerakines, P. A., Tielens, A. G. G. M., Adamson, A. J., Boogert, A. C. A., Chiar, J. E., de Graauw, T., Ehrenfreund, P., Prusti, T., Schutte, W. A., Vandenbussche, B., & van Dishoek, E. F. 1998, ApJ, 498, L159+

Wickramasinghe, N. C. & Guillaume, C. 1965, Nature, 207, 366

Wilms, J., Allen, A., & McCray, R. 2000, ApJ, 542, 914

Wilms, J., Nowak, M. A., Dove, J. B., Fender, R. P., & di Matteo, T. 1999, ApJ, 522, 460

Witt, A. 1989, in IAU Symp. 135: Interstellar Dust, 87–+

Witt, A. N. & Schild, R. E. 1988, ApJ, 325, 837

Wojdowski, P. S., Liedahl, D. A., Sako, M., Kahn, S. M., & Paerels, F. 2003, ApJ, 582, 959

Wong, J., Rek, Z. U., Rowen, M., Tanaka, T., Schäfers, F., Müller, B., George, G. N., Pickering, I. J., Via, G., Devries, B., Brown, G. E., & Fröba, M. 1995, Physica B Condensed Matter, 208, 220

Woo, J. W., Clark, G. W., Day, C. S. R., Nagase, F., & Takeshima, T. 1994, ApJ, 436, L5

Yan, M. & Dalgarno, A. 1997, ApJ, 481, 296

Acknowledgments

Curriculum vitæ et studiorum

Personal Data:

Name:	Elisa Costantini
Date of Birth:	30th March, 1974
Place of Birth:	Rimini (Italy)
Nationality:	Italian

Education:

1988-1993: Scientific high school "A. Einstein", Rimini (Italy)
school leaving examination (maturità):
Grade vote: 60/60

1993-1998: Study of Physics and Astronomy, University of Bologna (Italy):
Diploma Thesis (laurea): *"X ray properties of quasars observed by BeppoSAX"*
Advisors: Prof. G.G.C. Palumbo, Dr. A. Comastri
Grade vote: 110/110 *with honour*

Current Position:

2000-2004: Research Assistant at the Max-Planck-Institut
für extraterrestrische Physik in Garching (Germany).

Previous Position :

May 1999-May 2000: Research Assistant at the
Harvard-Smithsonian Astrophysical Observatory, Cambridge, MA

List of publications

- E. Costantini, P. Predehl & M. Freyberg
  The XMM-Newton view on Interstellar Dust
  2004, to appear in Memorie della Societa' Astronomica Italiana, the Proceedings
  of the EPIC Consortium (held on Oct 14-16, 2003 in Palermo).

- Th. Boller, R. Keil, G. Hasinger, E. Costantini, R. Fujimoto, N. Anabuki,
  I. Lehman & L. Gallo
  XMM-Newton Observations of the Ultraluminous IRAS Galaxy NGC 6240
  2003, A&A,.411, 63

- P. Predehl, E. Costantini, G. Hasinger, Y. Tanaka
  **XMM-Newton observation of the Galactic Center, evidence against
  the X-ray reflection nebulae model**
  in *X-Ray Surveys, in the Light of the New Observatories*, Astronomische Nachrichten,
  Feb 2003 issue.

- P. Predehl, V. Burwitz, E. Costantini & J. Trümper.
  **Geometrical Distance Measurement of Cyg X-3 Using its X-ray Scat-
  tering Halo**
  in *New Century of X-ray Astronomy* , H. Inoue and H. Kunieda (eds), 251, 46
  (2001).

- E. Costantini & P. Predehl
  **Chandra observation of GX 5-1 halo: a deeper understanding of in-
  terstellar dust properties**
  in *Two Years of Chandra Symposium*, 34C (2001)

- S. Mathur, E. Costantini, F. Nicastro, A. Fruscione, B. Wilkes
  Complex X-Ray Absorption in NGC 3516: New Results
  in *Probing the Physics of Active Galactic Nuclei*, B.M. Peterson, R.W. Pogge
  and R.S. Polidan (eds) ASP, 224, 275 (2001)

- E. Costantini, C. Salvini, B. Wilkes, F. Nicastro, S. Mathur, A. Fruscione, A. Co-
  mastri.
  **The complex and variable absorption of NGC 3516 observed by Bep-
  poSAX**
  in *X-ray astronomy: stellar endpoints, AGN, and the diffuse X-ray background*
  N.E. White, G. Malaguti, and G.G.C. Palumbo (eds), AIP, 599,590, (2001)

- E. Costantini, F. Nicastro, A. Fruscione, S. Mathur, A. Comastri, M. Elvis,
  F. Fiore, C. Salvini, G.M. Stirpe, C. Vignali, B. Wilkes, P.T. O'Brien & M.R. Goad.

The complex X-ray absorbers of NGC 3516 observed by BeppoSAX
2000, ApJ, 544,283

- T. Mineo, F. Fiore, A. Laor, E. Costantini, A. Comastri et al.
  BeppoSAX broad band observation of low redshift quasars:spectral curvature and Iron Kα line
  2000, A&A, 359, 471

- E. Costantini, A. Comastri, C. Vignali, F. Fiore, E. Giallongo.
  BeppoSAX observations of high-redshift quasars
  1999, MmSAI, 70, 265.